ABSTRACT

Title of Document: CHARACTERIZATION AND MODELING OF TWO-PHASE HEAT TRANSFER IN CHIP-SCALE NON-UNIFORMLY HEATED MICROGAP CHANNELS

Ihab A. Ali, Doctor of Philosophy, 2010

Directed By: Professor Avram Bar-Cohen
Department of Mechanical Engineering

A chip-scale, non-uniformly heated microgap channel, 100 micron to 500 micron in height with dielectric fluid HFE-7100 providing direct single- and two-phase liquid cooling for a thermal test chip with localized heat flux reaching 100 W/cm^2, is experimentally characterized and numerically modeled. Single-phase heat transfer and hydraulic characterization is performed to establish the single-phase baseline performance of the microgap channel and to validate the mesh-intensive CFD numerical model developed for the test channel. Convective heat transfer coefficients for HFE-7100 flowing in a 100-micron microgap channel reached 9 kW/m^2K at 6.5 m/s fluid velocity. Despite the highly non-uniform boundary conditions imposed on the microgap channel, CFD model simulation gave excellent agreement with the experimental data (to within 5%), while the discrepancy with the predictions of the classical, “ideal” channel correlations in the literature reached 20%.

A detailed investigation of two-phase heat transfer in non-ideal micro gap channels, with developing flow and significant non-uniformities in heat generation, was performed.

Significant temperature non-uniformities were observed with non-uniform heating, where the wall temperature gradient exceeded 30°C with a heat flux gradient of 3-30 W/cm^2, for the quadrant-die heating pattern compared to a 20°C gradient and 7-14 W/cm^2 heat flux gradient for the uniform heating pattern, at 25W heat and 1500 kg/m^2s mass flux.

Using an inverse computation technique for determining the heat flow into the wetted microgap channel, average wall heat transfer coefficients were found to vary in a complex fashion with channel height, flow rate, heat flux, and heating pattern and to typically display an inverse parabolic segment of a previously observed M-shaped variation with quality, for two-phase thermal transport. Examination of heat transfer coefficients sorted by flow regimes yielded an overall agreement of 31% between predictions of the Chen correlation and the 24 data points classified as being in Annular flow, using a recently proposed Intermittent/Annular transition criterion. A semi-numerical first-order technique, using the Chen correlation, was found to yield acceptable prediction accuracy **(**17%**)** for the wall temperature distribution and hot spots in non-uniformly heated “real world” microgap channels cooled by two-phase flow.

Heat transfer coefficients in the 100-micron channel were found to reach an Annular flow peak of ~8 kW/m^2K at $G=1500$ kg/m^2s and vapor quality of $x=10\%$. In a 500-micron channel, the Annular heat transfer coefficient was found to reach 9 kW/m^2K at 270 kg/m^2s mass flux and 14% vapor quality level. The peak two-phase HFE-7100 heat transfer coefficient values were nearly 2.5-4 times higher (at similar mass fluxes) than the single-phase HFE-7100 values and sometimes exceeded the cooling capability associated with water under forced convection. An alternative classification of heat transfer coefficients, based on the variable slope of the observed heat transfer coefficient curve), was found to yield good agreement with the Chen correlation predictions in the pseudo-annular flow regime (22%) but to fall to 38% when compared to the Shah correlation for data in the pseudo-intermittent flow regime.

CHARACTERIZATION AND MODELING OF TWO-PHASE HEAT TRANSFER IN CHIP-SCALE NON-UNIFORMLY HEATED MICROGAP CHANNELS

by

Ihab A. Ali

Dissertation submitted to the Faculty of the Graduate School of the
University of Maryland, College Park, in partial fulfillment
Of the requirements for the degree of
Doctor of Philosophy
2010

Advisory Committee:
Professor Avram Bar-Cohen, Chair
Professor Marino DiMarzo
Professor Patrick McCluskey
Professor Peter Sandborn
Professor Bao Yang
Professor Gary Pertmer

© Copyright by

Ihab A. Ali

2010

Dedication

To my sister Rola

Your Soul will inspire us and be in our hearts forever.

Acknowledgements

Thank you my advisor Professor Avram Bar-Cohen for your advice, wisdom and support throughout the years of this work. I would like to thank my committee members, Professor Marino DiMarzo, Professor Patrick McCluskey, Professor Peter Sandborn, Professor Bao Yang and Professor Gary Pertmer, for their great comments, support and advice.

Many thanks to my friends Emil Rahim, Vinh Nguyen, Henry Lam, William Maltz, Ceferino Sanchez, Dr. Attila Aranyosi, Juan Cruz, Dr. Himanshu Pokharna, Dr. Rajiv Mongia, Dr. Jay Nigen and Bernie Rihn.

I have great gratitude to the Advanced Cooling Technologies' (ACT) Dr. Jon Zuo, Mr. Richard Bonner, Mr. John Hartenstine and especially my dear friend Mr. Scott Garner for their great efforts and support with the design of the apparatus used in this research.

Special thanks to Mr. Phil Tuma of 3M for his technical support and donation of the HFE-7100 fluid used in this work.

Thanks to my late sister Rola, your soul inspired and enriched me to stay in course until the end. Thanks to my mother Sabiha, my father Abdulkarim, my sisters Heba and Reem, my brother Hossam and my nephews Hasan and Hany. I love you.

Thank you my wife Alia and my son Sammy for your support and love. I am sorry for not been able to spend enough time with you the past few years. You are my life.

Table of Contents

Dedication……………………………………………………………………...……v

Acknowledgements ……………………………………………………….....vi

Table of Contents……………………………………...………………….........vii

List of Tables……………………………………………………….................xi

List of Figures………………………………………………………..............xiv

1. Trends and Cooling Requirements in the Electronic Industry………………...…….1

2. Liquid Cooling of Electronic Modules – Literature Review………………………10

2.1 Introduction………………...……………………………………..........10

2.2 Microchannel Coolers………………………….………….....…….11

2.3 Pool Boiling...14

2.4 Liquid Immersion Cooling……………………………………….....16

2.5 Liquid Immersion Modules...18

2.6 Flow Boiling...20

3. Theoretical Background...23

3.1 Single Phase Thermofluid Characteristics in Miniature Channels.............23

3.1.1 Pressure drop correlations………………………………...….23

3.2.2 Heat transfer correlations…………………………………….25

3.3.3 Effect of heating non-uniformity………………………………27

3.2 Two-Phase Thermofluid Characteristics in Miniature Channels…..……..28

3.2.1 Introduction……………………………………………...…...28

3.2.2 Two-phase flow regime modeling……………………………31

3.2.3 Characteristics of two-phase heat transfer in micro channels…..34

3.2.4 Heat transfer correlations……………………….………...…35

3.2.5 Unresolved issues in two-phase behavior in microgaps………...41

4. Experimental Apparatus ……………………………………………………43

4.1 Overall Description……………………………………………………43

4.2 Calibration of Flow Meter ……………………………………………45

4.3 Chip Thermal Test Vehicle………………………...…………………..46

4.4 The Microgap Test Channel… …………………………………………..52

4.5 Chip TTV - Sensor Calibration Procedure………………………………..53

4.6 Fluid Selection and HFE-7100 Novec Properties…………………………54

5. CFD Model and Simulation……………………………...……………………59

5.1 Introduction………………………………………………………………59

5.2 Equations Solved and Methodology………………………………………59

5.3 Model Description and Conjugate Heat Transfer……….………………...61

6. Single-Phase Data and Discussion…………………..…………………………..67

6.1 Basic Relations……………………..………………………………..67

6.2 Error Analysis……………………………………………………………..68

6.3 Single Phase Results………………………………………………………70

6.3.1 Comparison of experimental, CFD and theoretical correlation....70

6.3.2 Raw temperature data and comparison to CFD………………....76

6.3.3 Conjugate effects and conduction spreading in advanced

microprocessors……………………………………………………….82

6.3.4 Temperature distribution – Uniform heating…..………………...89

6.3.5 Temperature Distribution - Half-die and quadrant-die heating…93

6.3.6 Inversely determined heat transfer coefficients………………....95

6.4 Overall Single-Phase Hydraulic and Thermal Performance…….………...98

6.5 Conclusions…………………………………………………………...102

7. Two-Phase Heat Transfer Experimental Data and Discussion……………………106

7.1 Introduction and Basic Relations……………..……………………..…106

7.2 Taitel-Dukler Flow Regime Map……………………………………..111

7.3 Heat Transfer Characteristics…………………………….……………...125

7.4 Heat transfer Characteristics with Non-Uniform Heating……………….131

8. Heat Transfer Correlations…………………………………………………..…136

8.1 Introduction…………………………………………………………...136

8.2 Heat Transfer Correlation Based on Two-Phase Reynolds Number……137

8.3 Flow Regime Sorting Based on TD Transition Line……………………138

8.4 Flow Regime Sorting Based on Characteristic Curve…………………...142

8.5 Inverse Calculations of Spatial Heat Transfer Coefficient………………147

8.6 Inverse Calculations of Spatial Chen-Based Heat Transfer Coefficient...152

8.7 Prediction of Wall Temperature Distribution and Hot spots of Non-uniform

Heating……………………………………………………………..……..155

8.8 Conclusions……………………………………………………………..…158

9. Conclusion and Future Work………………..……………………………….164

9.1 Conclusion……………………………………………………………….164

9.2 Future Work…..……………………………….………………………171

10. Bibliography……………………………..……………………………......174

List of Tables

Table 1: HFE-7100 Environmental Properties [52]. 55

Table 2: HFE-7100 Toxicity Properties [52]. 56

Table 3: Characteristics of 3M's Fluorinert and Novec Fluids [52]. 57

Table 4: HFE-7100 Thermo-Physical Properties Compared to Other Coolants...........58

Table 5: Sensor Temperatures for the Uniformly Heated 100-micron Microgap Channel with the Flow of HFE-7100, Tin=23°C, q″=7W/cm2. 77

Table 6: Sensor Temperatures for the Half-Die Heated 100-micron Microgap Channel with the Flow of HFE-7100, Tin=23°C, q″=7W/cm2. 78

Table 7: Sensor Temperatures for the Quadrant-Die Heated 100-micron Microgap Channel with the Flow of HFE-7100, Tin=23°C, q″=7W/cm2. 78

Table 8: Sensor Temperatures vs. Flow Rates and Junction vs. Surface (Wall) Temperatures for 100-micron Channel and Uniform Heating with the flow of HFE-7100, Tin=23°C, q″=7W/cm2...81

Table 9: Sensor Temperatures vs. Flow Rates and Junction vs. Surface (Wall) Temperatures for 100-micron Channel and Half-Die Heating with the flow of HFE-7100, Tin=23°C, q″=7W/cm2...81

Table 10: Sensor Temperatures vs. Flow Rates and Junction vs. Surface (Wall) Temperatures for 100-micron Channel and Quadrant-Die Heating with the flow of HFE-7100, Tin=23°C, q″=7W/cm2. 82

Table 11: Average error (ε_{AVE}) of Heat transfer Coefficient Predictions Sorted by Annular and Intermittent Flow Regimes per Classical T&D Line and $\frac{We^{1/2}}{Bo^{1/4}} = 6.2$ Based Line-Uniformly-Heated Channel. 139

Table 12: Parameters of Two-Phase Heat Transfer Chen Correlation on 100-micron Channel, Showing Error Reduction by Setting Convective Enhancement Term F=1. 141

Table 13: Average Error (ε_{AVE}) of Heat Transfer Coefficient Predictions Using Chen and Shah Correlations for Uniformly Heated Channels. 143

Table 14: Average Error (ε_{AVE}) of Heat Transfer Coefficient Predictions Sorted by Pseudo Annular and Pseudo Intermittent Flow regimes Graphically per (h vs. x) Characteristic Curve, for Uniformly Heated Channels.................................... 144

Table 15: Average Error (ε_{AVE}) of Heat Transfer Coefficient Predictions Using Chen and Shah Correlations for Half-Die Heated Channels..................................... 144

Table 16: Average Error (ε_{AVE}) of Heat Transfer Coefficient Predictions Sorted by Pseudo Annular and Pseudo Intermittent Flow regimes Graphically per (h vs. x) Characteristic Curve, for Half-Die Heated Channels. 145

Table 17: Average Error (ε_{AVE}) of Heat Transfer Coefficient Predictions Using Chen and Shah Correlations for Quadrant Heated Channels. 145

Table 18: Average Error (ε_{AVE}) of Heat Transfer Coefficient Predictions Sorted by Pseudo Annular and Pseudo Intermittent Flow regimes Graphically per (h vs. x) Characteristic Curve, for Quadrant Heated Channels....................................... 146

Table 19: Experimental (Two-Phase Test) and Iteratively Adjusted CFD Wall Temperatures for Three Heating Patterns. 100 micron Channel, 25W, G= 1500 kg/m2s. 149

Table 20: Temperature Errors of Conduction-Only Model with Prescribed Chen-Based Average h on Wall, 100-micron Channel Flowing HFE-7100, P=25W, G= 1500 kg/m2s. 158

List of Figures

Figure 1: iNEMI's Server Chip power and Heat Flux Trends [1]. 1

Figure 2: ITRS Power Trend for High Performance and Cost Performance Electronic Chips [2]...2

Figure 3: Trends in Chip Package Thermal Resistance [3]. 3

Figure 4: Power Non-Uniformity of Intel's Itanium Processor [4]...............................4

Figure 5: Power Map (Non-Uniformity) Impact on Thermal and Cooling Performance [4]...5

Figure 6: Thermal Packaging Roadmap 2001-2016 [5] 6

Figure 7: Hot spot cooling by microchannel liquid cooled plate mounted on chip substrate via TIM layer [6]..10

Figure 8: High Power IGBT Module [7]. 11

Figure 9: Integrated Liquid (R134a) Cooled Plate for IGBT Module [7]. 12

Figure 10: Server Rack-Level Cooling for Stacked IGBT Modules [7] 12

Figure 11: Two-phase Flow regimes in horizontal channel [20]. 30

Figure 12: Taitel-Dukler Flow Regime Map Showing, Stratified, Bubble, Intermittent and Annular Flow Regimes- 100-micron Channel Dh=200 micron, HFE-7100 Fluid. 31

Figure 13: Heat transfer coefficient data from Yang and Fujita [37] and Cortina-Diaz and Schmidt [38] showing the characteristic M-shape behavior [20]. 33

Figure 14: Two-Phase Microgap Channel Test Apparatus...43

Figure 15: Design Schematics of the Two-Phase Microgap Channel Apparatus.........44

Figure 16: External Water-Cooled Condenser for the two-Phase Microgap Channel Apparatus. 45

Figure 17: Pressure Relief Reservoir for the two-Phase Microgap Channel Apparatus. 46

Figure 18: Kobold Flow Meter Calibration Curves for Water and HFE-7100............47

Figure 19: Intel's Merom Processor Thermal Test Vehicle (TTV) [51]. 48

Figure 20: Intel's TTV Schematic Three Different Power (Heating) Zones with Locations of Temperature Sensors. 48

Figure 21: Intel's TTV Serpentine-Type Heating Zones and Locations of Temperature Sensors [51]. 49

Figure 22: Assembled Intel TTV Showing Locations of the Three Heater Zones. 50

Figure 23: Intel's TTV Board. 51

Figure 24: TTV Cooper Channel 52

Figure 25: Hermetically Sealed Microgap Channel. 52

Figure 26: TTV Characteristic Temperature Sensor Calibration. 53

Figure 27: HFE-7100 Thermal and Fluid Properties [52]. 58

Figure 28: The CFD Computational Grid. 61

Figure 29: Fluid Channel Grid. 62

Figure 30: Full Conjugate Domain Grid. 63

Figure 31: CFD Solution Convergence for Key Temperature Sensors. 63

Figure 32: 3-D View of the Microgap Fluid Channel CFD Model.............................64

Figure 33: XY and YZ Views of the Microgap Fluid Channel CFD Model. 65

Figure 34: Model of the Junction Plane Showing the Emulated Serpentine-Type Heating Zones..66

Figure 35: Effect of Fluid Velocity on Single-Phase Pressure Drop in a 100-micron Microgap Channel Flowing HFE-7100 (Dh = 200 micron). 72

Figure 36: Effect of Fluid Velocity on Single-Phase Heat Transfer Coefficient in a 100-micron Microgap Channel Flowing HFE-7100 (Dh = 200 micron). P=10W, Tin=23C. 73

Figure 37: Single-Phase Pressure Drop vs. Velocity for HFE-7100 in a 100-micron Microgap Channel (Dh=200 micron). 75

Figure 38: Single-Phase Heat Transfer Coefficient vs. Velocity for HFE-7100 in a 100-micron Microgap Channel (Dh=200 micron). P=10W, Tin=23C. 76

Figure 39: Die Average Sensor Excess Temperature Test Data and CFD Simulation vs. Velocity, HFE-7100 flowing in a 100-micron Microgap Channel and Uniform Heating q″=7W/cm2. 79

Figure 40: Conduction Spreading Conjugate Effect on Wall Spatial Heat Flux and Heat Transfer Coefficient for Uniformly Heated 100-micron Channel with the Flow of HFE-7100, Tin=23°C, q″=7W/cm2..84

Figure 41: Conduction Spreading Conjugate Effect on Wall Spatial Heat Flux and Heat Transfer Coefficient for Half-Die Heated 100-micron Channel with the Flow of HFE-7100, Tin=23°C, q″=7W/cm2. 85

Figure 42: Conduction Spreading Conjugate Effect on Wall Spatial Heat Flux and Heat Transfer Coefficient for Quadrant-Die Heated 100-micron Channel with the Flow of HFE-7100, Tin=23°C, q″=7W/cm2..86

Figure 43: Single-Phase Conjugate Heat Transfer Conversion Rate vs. Fluid Inlet Velocity for the 100-micron Microgap Channel. P=10W, Tin=23C....................89

Figure 44: Chip Surface (Wall) Temperature Distribution of Uniformly Heated 100-micron Microgap Channel - (a) 0.7m/s (left), (b) 6.5m/s (right), Tin =23C.........92

Figure 45: Mid-Height Fluid Velocity Vectors Distribution for a 100-micron Uniformly Heated Microgap Channel - (a) 0.7m/s (left), (b) 6.5m/s (right). 92

Figure 46: Mid-Height Pressure Distribution for a 100-micron Uniformly Heated Microgap Channel - (a) 0.7m/s (left), (b) 6.5m/s (right). 93

Figure 47: Chip Surface (Wall) Temperature Distribution of Half-Die Heated 100-micron Microgap Channel - (a) 0.7m/s (left), (b) 6.5m/s (right), Tin=23C..........94

Figure 48: Chip Surface (Wall) Temperature Distribution of Quadrant-Die Heated 100-micron Microgap Channel - (a) 0.7m/s (left), (b) 6.5m/s (right), Tin=23C...95

Figure 49: Spatial Variation of Heat Transfer Coefficient for Uniformly Heated 100-micron Microgap Channel - (a) 0.7m/s (left), (b) 6.5m/s (right), Tin=23C..........96

Figure 50: Spatial Variation of Heat Transfer Coefficient for Half-Die Heated 100-micron Microgap Channel - (a) 0.7m/s (left), (b) 6.5m/s (right), Tin=23C..........97

Figure 51: Spatial Variation of Heat Transfer Coefficient for Quadrant-Die Heated 100-micron Microgap Channel - (a) 0.7m/s (left), (b) 6.5m/s (right), Tin=23C...97

Figure 52: Pressure Drop vs. Re for a Microgap Channel with Various Channel Heights, flowing HFE-7100, Tin=23°C, q″=7W/cm2. 100
Figure 53: Heat Transfer Coefficient vs. Re for a Microgap Channel with Various Channel Heights, flowing HFE-7100, Tin=23°C, q″=7W/cm2. 101
Figure 54: Pressure Drop vs. Re for a Microgap Channel with Various Channel Heights, flowing Water, Tin=23°C, q″=7W/cm2. 102
Figure 55: Heat Transfer Coefficient vs. Re for a Microgap Channel with Various Channel Heights, flowing Water, Tin=23°C, q″=7W/cm2. 102
Figure 56: Two-phase h vs. q″ and x for Uniform Heated 100-micron Channel Flowing HFE-7100. 110
Figure 57: Two-phase h vs. q″ and x for Uniform Heated 200-micron Channel Flowing HFE-7100. 111
Figure 58: Two-phase h vs. q″ and x for Uniform Heated 500-micron Channel Flowing HFE-7100. 111
Figure 59: Taitel-Dukler Map with Flow Regimes and h's for Uniform Heating and 100-micron Channel. G=350, 500, 650, 800, 1000 and 1500 kg/m2s...............113
Figure 60: Taitel-Dukler Map with Flow Regimes and h's for Uniform heating and 200-micron Channel. G=150, 350, 500, 650, 800, 1000 and 1500 kg/m2s. 114
Figure 61: Taitel-Dukler Map with Flow Regimes and h's for Uniform Heating and 500-micron Channel. G=80, 150, 270 and 350 kg/m2s. 115
Figure 62: Tabatabai & Faghri's Modification to the Taitel-Dukler Map Showing the Proposed Transition Line to Annular Flow [20]. 117

Figure 63: Taitel-Dukler Map with Flow Regimes and h's for Half-Die Heating and 100-micron Channel. G=350, 500, 650, 800, 1000 and 1500 kg/m2s................120

Figure 64: Taitel-Dukler Map with Flow Regimes and h's for Half-Die Heating and 200-micron Channel. G=150, 350, 500, 650, 800 and 1500 kg/m2s..................121

Figure 65: Taitel-Dukler Map with Flow Regimes and h's for Half-Die Heating and 500-micron Channel. G=80, 150, 270 and 350 kg/m2s....................................122

Figure 66: Taitel-Dukler Map with Flow Regimes and h's for Quadrant-Die Heating and 100-micron Channel. G=350, 500, 650, 800, 1000 and 1500 kg/m2s. 123

Figure 67: Taitel-Dukler Map with Flow Regimes and h's for Quadrant-Die Heating and 200-micron Channel. G=150, 350, 500, 650, 800, 1000 and 1500 kg/m2s. 124

Figure 68: Taitel-Dukler Map with Flow Regimes and h's for Quadrant-Die Heating and 500-micron Channel. G=80, 150, 270 and 350 kg/m2s. 125

Figure 69: Two-Phase h vs. Exit Quality x of the Yang&Fujita [37] and Diaz et al [38] Data [20]. 127

Figure 70: Two-Phase h vs. Exit Quality x of the Uniformly Heated 100-micron Microgap Channel. 128

Figure 71: Two-Phase h vs. Exit Quality x of the Uniformly Heated 200-micron Microgap Channel. 129

Figure 72: Two-Phase h vs. Exit Quality x of the Uniformly Heated 500-micron Microgap Channel. 130

Figure 73: Two-Phase h vs. q and x for Half-Die Heating and 100-micron Channel.131

Figure 74: Two-Phase h vs. q and x for Half-Die Heating and 200-micron Channel.132

Figure 75: Two-Phase h vs. q and x for Half-Die Heating and 500-micron Channel.132
Figure 76: Two-Phase h vs. q and x for Quadrant-Die Heating and 100-micron Channel. 133
Figure 77: Two-Phase h vs. q and x for Quadrant-Die Heating and 200-micron Channel. 133
Figure 78: Two-Phase h vs. q and x for Quadrant-Die Heating and 500-micron Channel. 134
Figure 79: Two-Phase Heat Transfer Coefficient versus Retp for the Uniformly Heated 100-micron Microgap Channel..138
Figure 80: Characteristic Heat Transfer Coefficient Curve with Illustrated Ranges of Pseudo Annular and Pseudo Intermittent Flow Regimes, Uniformly-Heated 100-micron Channel, G =1500 kg/m2s..143
Figure 81: Inversely Calculated Spatial Heat Transfer Coefficient for 100-micron Channel and Uniform Heating. 25W, G= 1500 kg/m2s. 150
Figure 82: Inversely Calculated Spatial Heat Transfer Coefficient for 100-micron Channel and Half-Die Non-Uniform Heating. 25W, G= 1500 kg/m2s.............151
Figure 83: Inversely Calculated Spatial Heat Transfer Coefficient for 100-micron Channel and Quadrant-Die Non-Uniform Heating. 25W, G= 1500 kg/m2s. 152
Figure 84: Inversely Calculated Chen-based Spatial Heat Transfer Coefficient for 100-micron Channel and Uniform Heating. 25W, G= 1500 kg/m2s. 154
Figure 85: Inversely Calculated Chen-based Spatial Heat Transfer Coefficient for 100-micron Channel and Half-Die Non-Uniform Heating. 25W, G= 1500 kg/m2s..155

Figure 86: CFD Temperature Distribution vs. Conduction-Only Based Modeling with Wall-Prescribed Average Chen-Based h. 25W, G= 1500 kg/m2s. 157

Chapter 1:

Trends and Cooling Requirements in the Electronic Industry

In recent decades the industry-wide trend in electronics has been toward greater compactness, functionality and feature count and thus power dissipation for nearly all the categories of electronic equipment. The International Electronics Manufacturing Initiative (iNEMI) projects the chip power and chip heat flux trends for various electronic enclosure form factors, from servers to notebook platforms. Figure 1 shows the iNEMI's view of chip power chip flux trends for server platforms [1]. It is quite clear from the figure that the market shall, if it has not already, experience unprecedented growth in chip power and heat flux that by 2012 could reach 300W and 150 W/cm^2 in heat dissipation and heat flux, respectively.

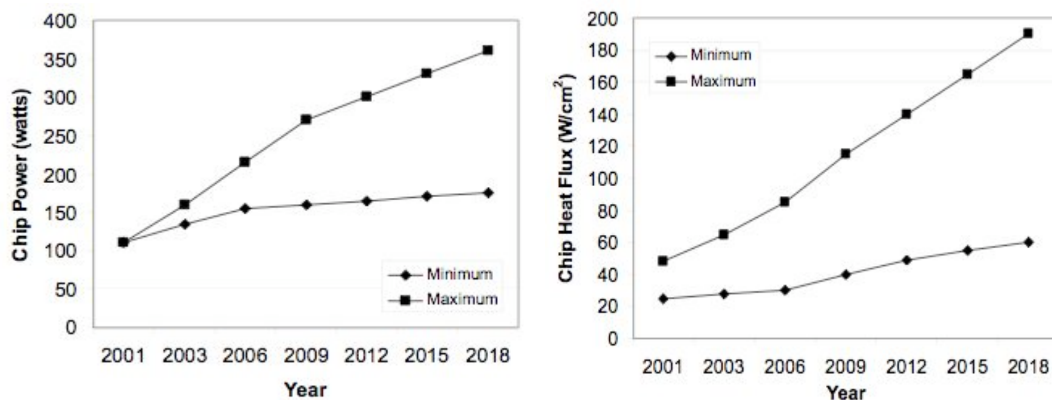

Figure 1: iNEMI's Server Chip power and Heat Flux Trends [1].

Although the increased awareness of power consumption and efforts to develop more energy efficient devices will cause this rate to slow, as per the International Technology Roadmap for Semiconductor (ITRS) shown in Figure 2, for the cost-performance system category, this slow down might not become apparent until the year 2015 [2]. On the other hand, changes in chip layout and packaging technologies, throughout recent years, have led to the wide adoption of flip chip technology and the appearance of highly non-uniform chip power dissipation. Both of these trends have had a strong impact on thermal management needs and thermal design constraints on advanced chip packages.

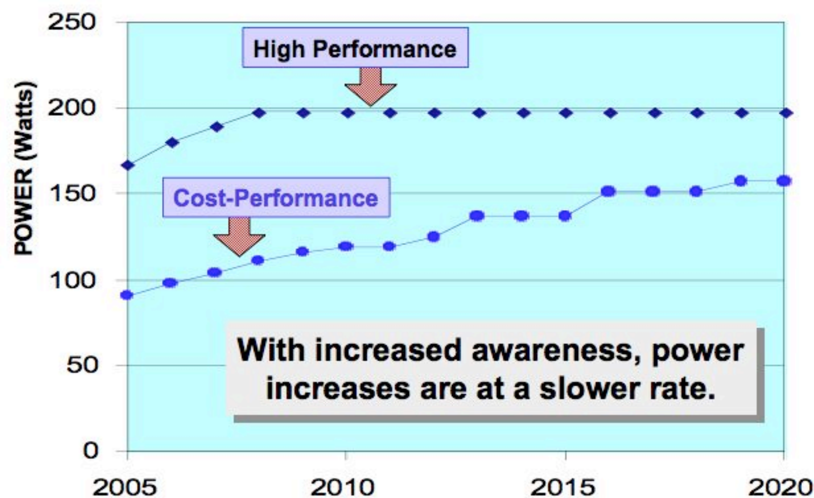

Figure 2: ITRS Power Trend for High Performance and Cost Performance Electronic Chips [2].

As shown in Figure 3, in the past decade thermal management of flip chip dies with non-uniform power dissipation has focused on the need to significantly lower the maximum chip-to-heat sink thermal resistance. Continuously improving heat sink performance has

made the chip-to-heat sink resistance dominant and the "controlling" or critical element of the total system thermal resistance [3]. Efforts must thus be directed at minimizing the chip-to-sink thermal resistance. Note that the arrow and circle in Figure 3 refer the thermal resistance curve to the year 2005, when the reference was published.

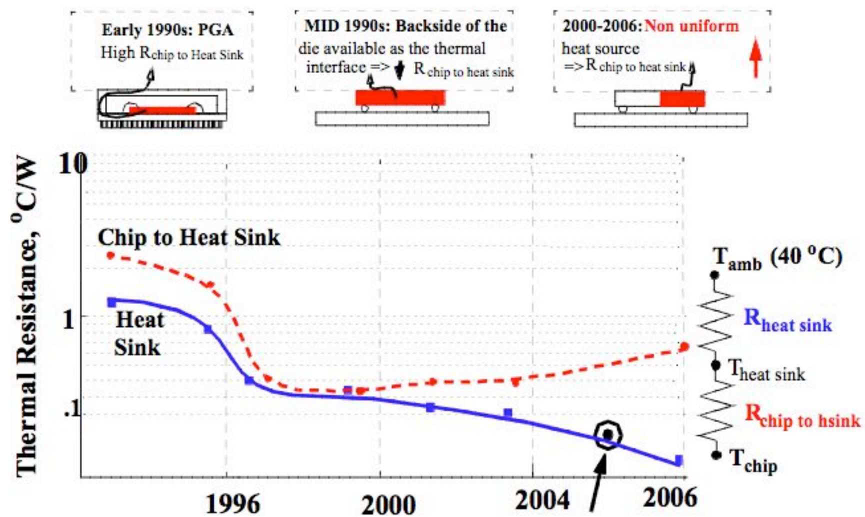

Figure 3: Trends in Chip Package Thermal Resistance [3].

The issue of chip power non-uniformity or non-uniform die heat flux is a frequent subject of the recent electronics cooling literature [4]. Figure 4 displays the heat flux

distribution on a Pentium III and Itanium chip, respectively, and shows how silicon architecture, design styles and complexity affect the power gradient across the die. While "hot spots" on the Intel Itanium processor can reach heat fluxes of 300 W/cm^2 [4], the Pentium III peak flux is close to just 50W/cm^2.

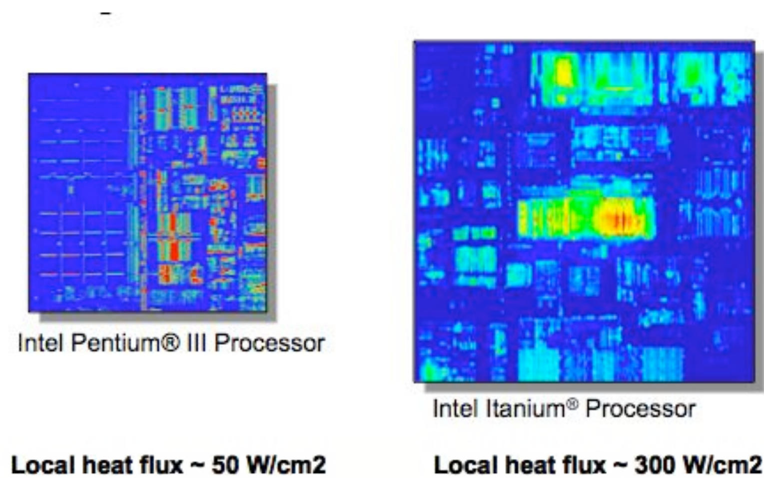

Figure 4: Power Non-Uniformity of Intel's Itanium Processor [4]

The impact of such on-chip hotspots, or high heat flux concentrations at the die junction plane, can be severe. This is clearly illustrated in Figures 5 where the thermal impact of power non-uniformity, or the presence of a hot spot, on the peak temperature rise is assessed. It is seen that the non-uniform distribution could, for the conditions examined, be equal to having an additional dissipation of about 30W, uniformly distributed, from the perspective of the overall thermal resistance and chip thermal management potential. [2,5]. Researchers and designers, faced by these challenges, have been focusing on more efficient thermal management techniques and alternative

approaches to smooth the temperature distribution resulting from the highly non-uniform die heat flux.

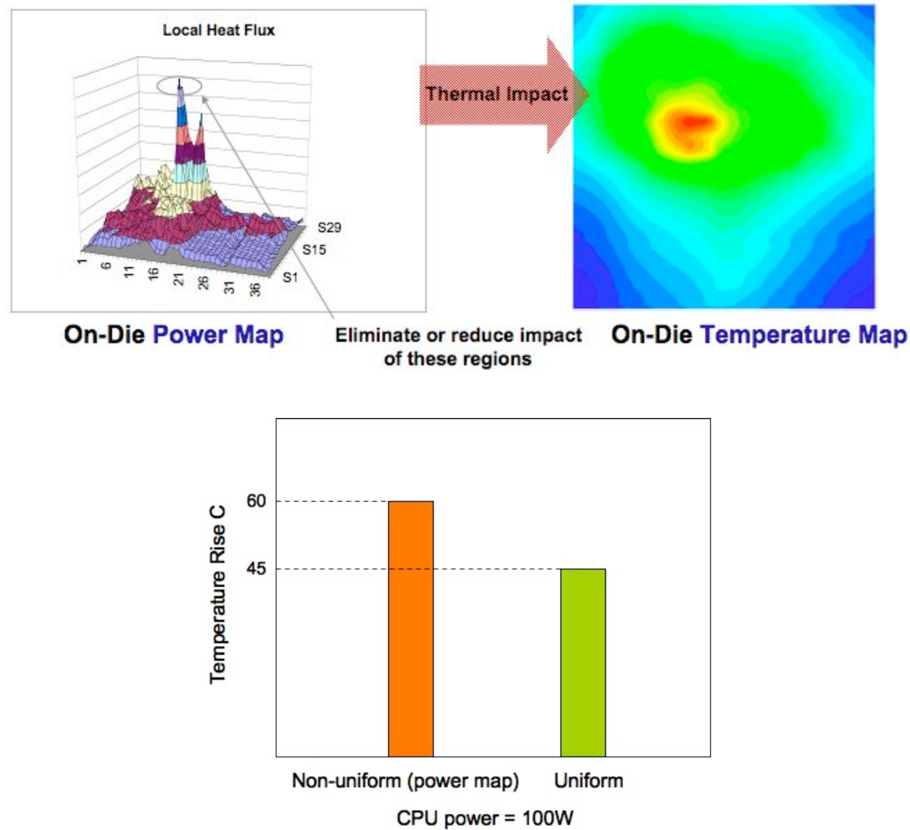

Figure 5: Power Map (Non-Uniformity) Impact on Thermal and Cooling Performance [4].

As a consequence, the thermal packaging community started searching for and investigating new cooling technologies for high heat flux chips, as depicted in Figure 6. While the initial efforts in the 2000-2005 time frame, associated with the transition to 130nm and later to 90nm features, involved improvements in the Thermal Interface Materials (TIMs), wafer thinning is a promising approach to reducing the thermal

resistance for chips with 65nm features. However, as the chip features continue to shrink towards 45nm and the chip power and heat flux increase towards 225W and 450W/cm^2, respectively, there is an urgent need for advanced thermal management techniques. This thermal management roadmap does suggest that for the 2013 and beyond, when chip heat flux might exceed 500W/cm^2, two-phase cooling by direct contact of an evaporating/boiling dielectric liquid with the chip might be the only viable thermal management solution. [5].

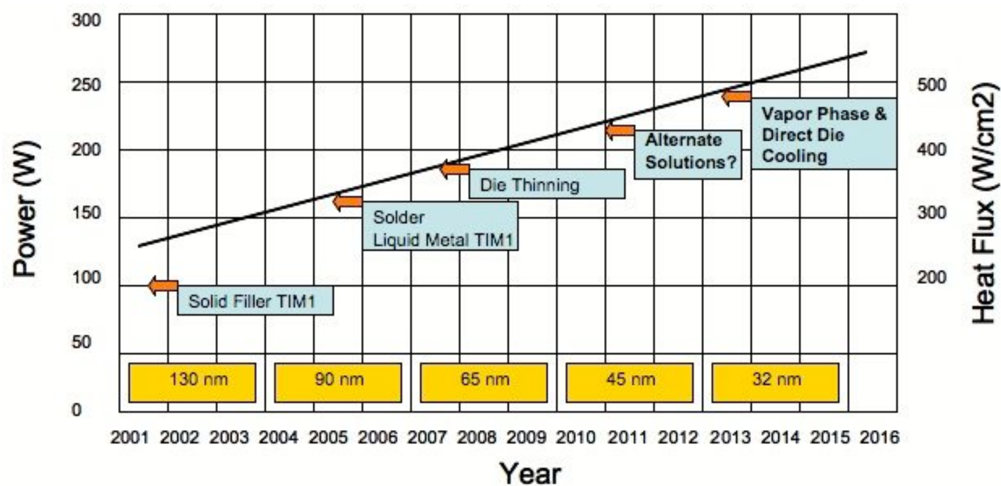

Figure 6: Thermal Packaging Roadmap 2001-2016 [5]

Dissertation Roadmap

The present study focuses on the two-phase thermal performance limits of non-uniformly heated microgap channels in a packaged chip-scale form factor. The research goal is to study the thermal performance of such microgap channel coolers in a non-ideal form factor with non-uniform heating conditions and to use the results to

provide the technical foundation for the engineering, design of such microgap channel coolers applied to single chips and also to 3D modules containing multiple chip stacks. While Chapter 1 provided an introduction to recent and future trends of cooling requirements in the electronics industry, Chapter 2 covers a literature review of liquid cooling of electronic modules. Chapter 3 provides the theoretical background for single-phase and two-phase thermofluid characteristics in miniature channels. Chapter 4 provides a detailed description of the experimental apparatus used to conduct the two-phase as well as single-phase experimental tests on the 100-, 200- and 500-micron channels used in the present work. Chapter 5 covers the details of the CFD based numerical model and simulations used to validate and enhance the experimental test data. Chapter 6 discusses the single-phase test data comparisons with available correlations and with CFD model results. The chapter also provides an overall assessment of the single-phase thermal performance of the various microchannels used in the study with HFE-7100 and water as the working fluid. Chapter 7 covers the two-phase data and discussion, including heat transfer characteristics and flow regime modeling. Chapter 8 discusses the experimental data comparison with heat transfer correlations in the literature for the Annular and Intermittent flow regimes. This chapter also covers the utilization of CFD for the inverse calculations of spatial heat transfer coefficient and introduces a simple semi-numerical approach for the prediction of wall temperature distribution and hot spots of non-uniform heating.

Chapter 2:

Liquid Cooling of Electronic Modules – Literature Review

2.1 Introduction

Thermal management needs of the electronics industry continue to be driven by the demand for increased functionality, high heat dissipation and density, component miniaturization, and the reliability benefits of junction temperature reduction and control.

Advanced liquid cooling thermal management techniques for electronics can be classified as direct or indirect methods; depending on whether, the cooling fluid is in direct contact with the electronic module chip package. Single-phase and two-phase liquid cooled microchannels are examples of indirect liquid cooling while pool boiling and liquid immersion provide good examples of direct liquid cooling. While one of the main benefits of direct liquid cooling is the elimination of the contact thermal resistance between the cooling module and the surface of the electronic chip, these techniques involve intensive reliability packaging and assembly and maintenance requirements. Nevertheless, this direct method, from a packaging perspective, is efficient for cooling 3D or multi-chip stacked modules. Active (pumped) liquid cooled microchannels while they are indirect methods, can provide extensive wetted surface area for the liquid to interact with in both single- or two-phase regimes. They

also constitute very good methods for cooling single chips such as advanced microprocessors and graphics chips.

2.2 Microchannel Coolers

Active liquid cooling has started to emerge as a feasible solution for even cost performance electronics systems. The recent increase in CPU heat fluxes coupled with the need to thermally design for the highest possible heat flux for speed reasons, caused thermal system to become more complex and has paved the way for active cooling. High power density cores on the die necessitate the use of active micromechanical means for heat removal [3**].**

Figure 7 shows that the use of single-phase microchannel liquid cooling can be an effective means to overcome the die hot spot problem and achieve acceptable junction temperatures [6]. However, this method did not eliminate the large TIM thermal resistance between the die and the first layer of microchannel assembly.

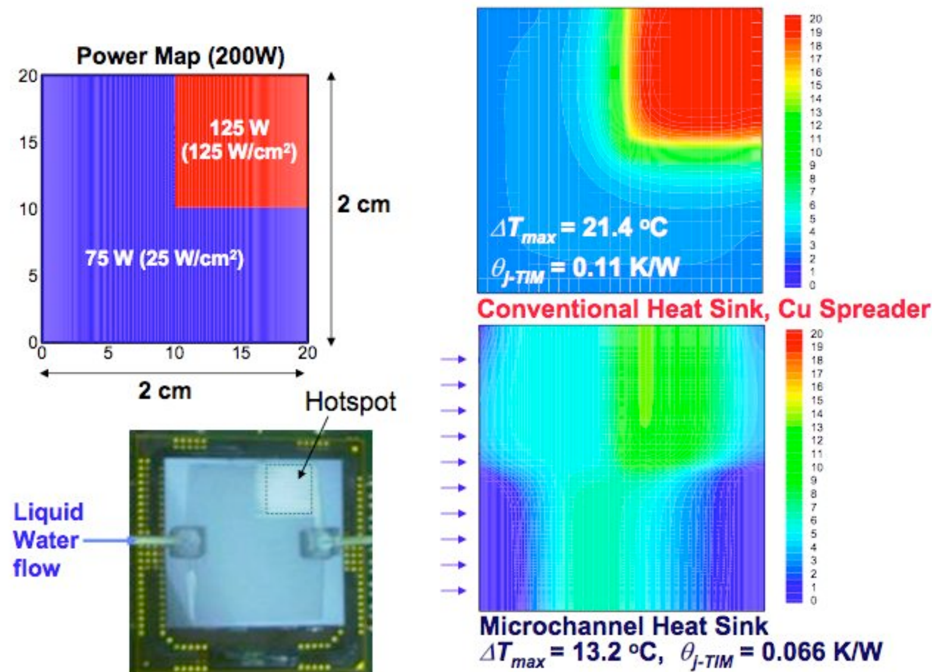

Figure 7: Hot spot cooling by microchannel liquid cooled plate mounted on chip substrate via TIM layer [6]

Figures 8 and 9 display successful implementations of two-phase liquid cold plates for industrial power electronics systems [7] such as Integrated Gate Bipolar Systems (IGBT's). The pumped two phase cooling achieved around 50% increase in power dissipation compared to single phase and 120% increase in power dissipation compared to air cooling. The physical volume reduction achieved with the two-phase-cooled system is significant and even provides a modest cost reduction versus the air-cooled system. The use of a vaporizable dielectric fluid, R134a indirectly contacting the chips, operating at its saturation temperature, allows the use of a smaller quantity of liquid, a smaller pump for low-flow operation, and smaller tubing diameters, when

compared to a comparable single-phase water cooling system designed for use within the same type of cabinet (shown in Figure 10) and to dissipate the same module heat loads. The use of a vaporizable dielectric fluid in a copper cold plate with convoluted fin internal structure is demonstrated to yield around 100% additional capacity to dissipate heat generated at the IGBT module base, as compared to the water-cooled cold plate tested; the improvement over the production air-cooled finned aluminum extruded thermal solution is demonstrated to be greater than 125% [7].

Figure 8: High Power IGBT Module [7].

Figure 9: Integrated Liquid (R134a) Cooled Plate for IGBT Module [7].

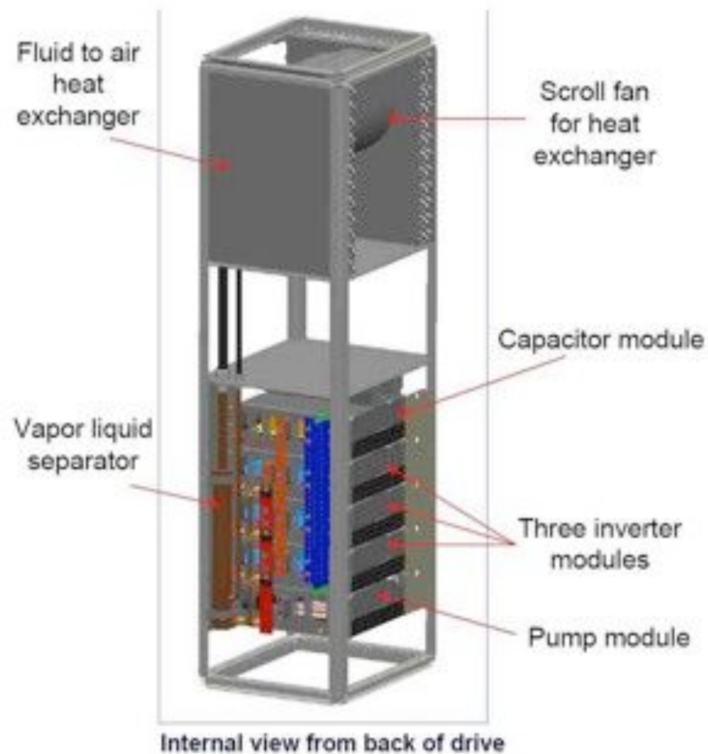

Figure 10: Server Rack-Level Cooling for Stacked IGBT Modules [7]

2.3 Pool boiling

Pool boiling as a method for cooling electronic modules can provide much higher performance than conventional forced air [8], Furthermore, understanding pool boiling is important for the successful implementation of immersion cooling.

You et al, [9] discussed a method for enhancing boiling heat transfer. The method of particle layering is introduced as an effective and convenient technique for enhancing boiling heat transfer on a surface. Such an enhanced surface, showed a decreased level

of wall superheat under boiling and an increased critical heat flux relative to superheat and critical heat flux values for an untreated surface, due perhaps to an increased number of nucleation sites or to a change in cooling modalities to two-phase flow in a porous layer. Application of this technique results in a decrease of heated surface temperature and a more uniform temperature of the heated surface; both effects are important in immersion cooling of electronic equipment.

Arik and Bar-Cohen [8], showed that boiling heat transfer with the candidate liquids provides heat transfer coefficients that are as much as two orders of magnitude higher than achievable with forced convection of air. Unfortunately, the highly effective nucleate boiling domain terminates at the Critical Heat Flux, approximately in the range of 20 W/cm^2 at atmospheric conditions and saturation temperature. Consequently, if immersion cooling is to be used, ways must be found to increase the pool boiling CHF of these dielectric liquids. Use of a pool boiling CHF correlation points to the possibility of reaching a CHF of nearly 60 W/cm^2, using elevated pressure and subcooling, along with a dilute mixture of a high boiling point fluorocarbon, and applying a microporous coating to the surface of the chip.

Bergles and Kim [10], demonstrates that the generation of vapor below a heated surface is an effective means of reducing the large superheat required for inception of boiling with liquids suitable for direct immersion cooling of microelectronic devices. In the experiments with R-113 and a plain copper heat sink surface, the incipient boiling superheat was reduced from 33 K to as low as 8 K. With a sintered boiling surfaces, the incipient boiling superheat was reduced from 22 K to as low as 7 K. A

reasonable explanation for the effectiveness of this sparging technique is that the impacting bubbles activate temporarily dormant cavities that, in turn, activate large neighboring cavities. The technique appears to be easily adaptable to liquid encapsulated modules containing arrays of microelectronic devices.

Normington et al [11], demonstrated experimental results related to the use of mixtures of dielectric liquids to control temperature and overshoot while handling high heat fluxes. A variety of pure dielectric liquids from Ausimont (boiling points from 81 to 110°C) were evaluated. These liquids are similar to Fluorinert liquids from 3M. Data have been taken on single pure liquids showing the usual expected substantial overshoot (26'C average) during the incipience of nucleate boiling. The addition of a second liquid to modulate the temperature and control the overshoot has been presented. Various mixtures (20-95% of low boiling point; 580% of high boiling point) were then tested with some mixtures showing virtually no overshoot (0-6 °C) while still allowing high total heat fluxes greater than 30 W/cm^2. On average, the overshoot was reduced from 26 to 4°C for a variety of liquid mixtures. Some mixtures allowed for zero overshoot. The 4°C overshoot was less than the temperature variation across the chip. The effect of liquid mixtures in reducing overshoot is pronounced only in the high subcooling case (50°C subcooling); for 10°C subcooling, the effect is insignificant. The mechanisms of these results are not clear. It is, however, clear that relatively small amounts of a second liquid can strongly modify the boiling heat transfer characteristics of the dielectric liquids.

2.4 Liquid Immersion Cooling

Liquid immersion cooling represents a potential method for meeting the requirements for removal of increasingly high heat fluxes from individual chips and from three-dimensional microelectronic packages. Kraus and Bar-Cohen [12] and Bar-Cohen et al [13], provide a detailed analysis on Liquid immersion cooling of microelectronic systems, many researchers investigated various aspects of liquid immersion cooling focusing on 3D modules. The electronic module's external surface temperature (condenser temperature) is a crucial aspect in the success of a liquid immersion technique as it limits the ability of the module's surface to expel thermal energy outside the system.

Yokouchi et al [14], presents a cooling techniques using direct immersion cooling for high-density packaging and provides a discussion focusing on a) the treatment of bubbles produced by nucleate boiling and b) the control of coolant composition to prevent "temperature overshoot" occurring at the boiling point as thermal hysteresis. Maintaining subcooled boiling (the initial stage of nucleate boiling) up to the maximum power of the application is a useful technique in high-density packaging of computers because this technique produces fewer problems than saturated boiling. Using a coolant that mixes two fluorocarbons having different boiling points at a ratio of 80%-20% was found to prevent temperature overshoot on the chip surface.

The adoption of direct immersion cooling of microelectronic chips and other devices

has been hampered by lack of understanding of, and inability to control, the temperature overshoot or high wall superheat associated with the inception of nucleate boiling.

2.5 Liquid Immersion Modules

Ciccio and Thun [15], showed that ebullient cooling with FC-78 refrigerant provided excellent cooling for an ultra-high density VLSI module mounted in a sealed container for condenser temperatures between 70F and 90F. They were able to double the module power density sustainable with conventional (forced air) cooling techniques. At a time when most chips were dissipating less than 1W, it was possible to maintain a 2W/chip and 15 W/in2 (2.35 W/cm^2) while keeping junction temperatures blow 150F. (65.6 ^{0}C)

Lee et al, [16] demonstrated experimentally the capability of liquid-encapsulated system to cool a multi-chip module (MCM) package. Tests were performed on both dry (no liquid-filled) and liquid-filled packages. In the liquid-filled situation, either a pure dielectric liquid or a dielectric liquid mixture was employed. The MCM package was externally cooled by either free-air or forced-air (1.0 to 2.54 m/s of air flow). Heat transfer history from single-phase, through nucleate boiling, to film boiling was documented.

The overall improvement for the liquid-filled package was 2–4 times compared to the dry package, due to the superior thermal properties of dielectric liquids compared to air. The maximum power dissipation in the liquid-filled package at 2.54 m/s external

airflow was 18 W (based on junction temperature maximum of 125C). In the liquid-filled package, both the single-phase and boiling heat transfer were enhanced by varying the external boundary conditions from free-air to forced-air.

The total power dissipation limit in the liquid-filled package is strongly influenced by the ability to condense the vapor in the package. By changing the boundary conditions from free-air to forced-air (2.54 m/s), the condenser (top lid) efficiency is raised, thus raising the maximum power dissipation by 2.5 times. Results also indicated that for any given external boundary condition, the allowable power dissipation did not vary much under different liquid conditions: non-degassed liquid, degassed liquid at slightly above ambient pressure, and degassed liquid at ambient pressure. When the system was sealed, increasing power in the package created large liquid pressure and raised its boiling point. The chips remained in the single-phase regime and no boiling occurred. The paper also studies the effect of coolant mixture of two fluids, D80/HT110 (50/50% by volume). The mixture boiling curve behaved differently than the single-liquid curve: it had a long path of partial boiling and did not reach film boiling as junction temperature reached 125C. This particular mixture showed less-efficient boiling heat transfer than the single liquid. However, a proper composition of the mixture may raise the allowable power in the module compared to the single liquid, while maintaining the average junction temperature below 125 C. With a small-scale package (such as in the present study), when the system was sealed (with pure liquid), increasing power in the package created large liquid pressure and raised its boiling point. Due to the high boiling point, the dies remained in the single-phase regime.

Nelson et al, [17] describes a multi-chip module (MCM) package that uses integral immersion cooling to transfer heat from the chips to a final heat transfer medium outside the package. The package is a miniature immersion cooled system with a pin-fin condenser that can be operated in either the submerged or vapor-space condensing mode. Tests have been performed with the module fully powered and with subsets of the chips powered. The results indicate that the heat transfer coefficient is similar in all partially powered modes. The paper shows that immersion cooling with Fluorinert FC72 is a viable method of thermally linking the chips in an MCM to an overhead heat exchanger, competitive in thermal resistance with both through-substrate cooling and direct above-substrate cooling.

Geisler el al [18], in their paper, explored the viability of passive liquid cooling to meet the needs of future VME-size electronics modules. Chip heat fluxes in excess of $20W/cm^2$ were achieved while maintaining chip temperatures below 110°C. Further, an overall module heat dissipation of 124W was transferred with 80°C module edge temperatures (FC-72, 3atm, finned module cover). The thermal performance of the module was limited by the presence of a bubble-fed vapor/air gap that reduced the ability of the module cover to extract heat from the liquid and threatened to burn out nearby components as it grew.

2.6 Flow Boiling

Microgap coolers provide direct contact between chemically inert, dielectric fluids and the back surface of an active electronic component, thus eliminating the significant

interface thermal resistance associated with thermal interface materials and/or solid-solid contact between the component and a microchannel cold plate. On the other hand, the very good thermal performance, represented by the flow boiling, especially with annular-flow regime, high heat transfer coefficient, makes the concept of microgap cooler an appealing one for scholars in the thermal packaging community.

Kim et al [19], provided an exploratory study of the thermofluid characteristics of two-phase microgap coolers flowing FC-72 in asymmetrically and uniformly heated channels. Taitel and Dukler flow regime mapping methodology suggested that intermittent and annular flow regimes dominated the behavior of their 110 micron and 500 micron channels. Their data revealed that area-average heat transfer coefficients between 7.5 kW/m^2K and 15.5 kW/m^2K, can be attained for microgap channels of 110 micron and 500 micron respectively. Heat transfer coefficient data was well bounded by the predictions of the Chen and Shah correlations for the Annular and Intermittent flow regimes, respectively.

Rahim et al [20], provided detailed analysis of microchannel/microgap heat transfer data for two-phase flow of refrigerants and dielectric liquids, gathered from the open literature and sorted by the Taitel and Dukler flow regime mapping methodology. Annular flow regime was found to be the dominant regime for this thermal transport configuration and its prevalence is seen to grow with decreasing channel diameter and to become dominant for refrigerant flow in channels below 0.1 mm diameter. A characteristic M-shaped heat transfer coefficient variation with quality (or superficial velocity) for the flow of refrigerants and dielectric liquids in miniature channels has

been identified. Comparison of the microgap refrigerant data to existing classical correlations reveals that the Chen correlation provides overall agreement to within a standard deviation of 38% for the entire data set. However, classification of the data by flow regime does allow for improved predictive accuracy.

Microgap channel coolers flowing two-phase dielectric fluid have a good potential for cooling advanced high power electronics for they provide good thermal performance and eliminate the inherited TIM thermal resistance prevailing with indirect liquid cooling techniques. They also can be considered as cost effective and reliable technique compared to the expensive microchannel coolers. In order, however, to address the particular applications in the industry for such microgap channel coolers, a focus should be on detailed study of the two-phase performance characteristics under non-ideal conditions including short channel length, non-uniformly heated channels, conjugate heat transfer effect and packaging in a chip-scale form factor. The present work focuses on studying and modeling the two-phase characteristics of microgap channels under these practical non-ideal industry parameters.

Chapter 3:

Theoretical Background

3.1 Single-phase Thermofluid Characteristics in miniature channels

The concept of a microgap is a promising cooling technique for advanced microelectronics. Microgap channels require no thermal interface attachments and thus allow for the direct and efficient of transfer heat directly form the chip surface. An appropriate design of a microgap requires knowing the pressure drop and overall thermal performance, as these two engineering parameters are important to size up the microgap and the pumping power associated with it.

3.1.1. Pressure drop correlations

Thome [21], in his Wolverine's Engineering Data Book lists numerous literature correlations of single-phase pressure drop. Garimella and Singhal [22], showed that conventional correlations for laminar and turbulent flow adequately predict the behavior in microchannels of hydraulic diameters as small as 250 μm.

Classical single-phase flow correlations for the pressure drop in parallel plate channel by Kays and London [23] can be expressed as:

$$\Delta P = \frac{\rho V^2}{2}\left[\left\{\left(1-\sigma_c^2\right)+K_c\right\}+4\cdot f\frac{L}{D_h}-\left\{\left(1-\sigma_e^2\right)+K_e\right\}\right] \tag{3.1}$$

Where $\frac{\rho V^2}{2}$ is the dynamic pressure associated with flow in the channel, $\sigma_c = A_c / A_{in}$ and $\sigma_e = A_c / A_{out}$ are the area ratios of contraction and expansion of the flow at the channel entrance and exit, respectively. K_c and K_e are the loss coefficients of flow irreversibilities and f is the friction factor representing the channel friction losses.

Shah and London [24] correlated the friction factor f in a parallel plate for laminar developing flow in the form of:

$$f = \left[\frac{3.44}{\left(x^+\right)^{1/2}} + \frac{24 + \frac{0.674}{4\cdot x^+} - \frac{3.44}{\left(x^+\right)^{1/2}}}{1 + 0.000029\cdot\left(x^+\right)^{-2}}\right] / \mathrm{Re} \tag{3.2}$$

where $x+$ is the dimensionless hydrodynamic axial distance, which can be expressed by:

$$x^+ = \frac{x / D_h}{\mathrm{Re}} \tag{3.3}$$

In the fully developed laminar flow, i.e. for $x^+ > 0.05$, the friction factor reaches an asymptotic value or $f = 96/\mathrm{Re}$.

3.1.2. Heat transfer correlations

The thermal performance of a microgap channel is evaluated using the dimensionless Nusslet number as given by:

$$Nu = \frac{h.D_h}{k} \tag{3.4}$$

Where h is the heat transfer coefficient, D_h is the channel hydraulic diameter and k is the fluid thermal conductivity and h is the heat transfer coefficient. The heat transfer coefficient is defined as:

$$h = \frac{q}{A\Delta T} \tag{3.5}$$

Where ΔT is the temperature difference between the channel heated surface (wall) and the cooling fluid, A is the wall surface area and q is the wall heat transfer rate that can be determined from implementing the channel energy balance equation via:

(3.6)

$$q = \dot{m} C_p (T_{outlet} - T_{inlet})$$

Where $\dot{m}$ the channel fluid mass flow rate, C_p is the fluid specific heat and T_{inlet} and T_{outlet} are the channel fluid inlet and outlet temperatures, respectively.

Wolverine's Engineering Data Book [21], lists numerous literature correlations of single-phase Nusslet number for a variety of flow types including laminar and fully developed turbulent flow.

Garimella and Singhal [22], showed that conventional correlations for fluid flow and heat transfer adequately predict the behavior in microchannels of hydraulic diameters as small as 250 μm.

Kays and Crawford [25], reviewed many Nusslet number equations available in the literature for circular tubes, circular tube annuli and rectangular tubes for laminar flow and thermally fully developed or developing flow with uniform surface temperature and uniform surface heat flux boundary conditions. Among them, and more directly related to the channel conditions in the present study, is the Nusslet number for laminar developing flow in parallel plate channels with isoflux boundary conditions as

$$Nu = 8.24 + \frac{0.065(D_h/L)\mathrm{Re}\,\mathrm{Pr}}{1 + 0.04[(D_h/L)\mathrm{Re}\,\mathrm{Pr}]^{\frac{2}{3}}} \tag{3.7}$$

where the value of 8.24 represents Nusslet number for the fully developed laminar flow.

In the fully developed turbulent flow, Dittus and Boelter equation [25] can be used for Re>10,000 and is given by

$$Nu = 0.023\mathrm{Re}^{0.8}\,\mathrm{Pr}^{0.4} \tag{3.8}$$

More specifically related to the characteristics of the channel type considered in the present work, Kakac and Shah [26] predicted the local and mean heat transfer coefficients in uniform heat flux, asymmetrically-heated, parallel plate channels as follows:

$$Nu_x = \left[\frac{1}{6} - \sum_{n=1}^{\infty} \frac{\exp\left(-4n^2\pi^2x^*\right)}{n^2\pi^2}\right]^{-1} \tag{3.9}$$

$$Nu_m = \left[\frac{1}{6} - \sum_{n=1}^{\infty} \frac{1-\exp\left(-4n^2\pi^2x^*\right)}{n^2\pi^2}\right]^{-1} \tag{3.10}$$

Where the dimensionless axial distance is given by:

$$x^* = \frac{L / D_h}{\mathrm{Re}\,\mathrm{Pr}} \tag{3.11}$$

3.1.3 Effect of heating non-uniformity

It is important to note the lack of available literature and correlations for non-uniform heat flux in refrigerant-cooled in micro channels. Remley, et al [27], experimentally investigated turbulent wall friction and forced convection heat transfer in a water-cooled trapezoidal channel with high Reynolds numbers and 1.14 cm hydraulic diameter. The paper reported that the Colebrook correlation [25] predicted the unheated channel friction factors well. It, however, systematically over predicted the measured friction factors obtained with the test section non-uniformly heated test section. Perimeter-average convective heat transfer coefficients for laterally non-uniform imposed heat fluxes were compared with the predictions of three widely-used correlations for turbulent flow in circular channels. All the correlations under predicted the data, typically by 11–28%. Although the form factor in Remley, et al's study is larger than in the present study, the paper nonetheless discussed an important factor that is the effect of heating non uniformity on the accuracy of correlations in predicting pressure drop and thermal performance of studied channels.

3.2 Two-phase Thermofluid Characteristics in miniature channels

3.2.1 Introduction

The research community had classified micro channels under different categories with different definitions. Mehendale et al [28], proposed a purely geometric definition, ignoring any impact of fluid properties, and considered passages in the diameter range from 1 micron to 100 micron as micro-channels, 100 microns to 1 mm as meso-channels, 1 mm to 6 mm as compact passages, and greater than 6 mm as conventional passages. Kandlikar and Grande [29], classified micro channels based on fabrication technology. They proposed that channels with hydraulic diameters of 3 mm or larger be considered as conventional, channels with a hydraulic diameter range of 200 micron to 3 mm to be classified as mini-channels, and, as new technologies were needed to create passages with diameters below 200 micron, such channels would be defined as micro-channels. Considering that severe rarefaction effects for many gases are encountered between 10 micron and 0.1 micron, and that such effects might become pronounced in two-phase flow, Kandlikar and Grande referred to this as the transitional region and used 10 microns as the lower limit on micro-channel behavior.

Kew & Cornwell [30] used the so-called confinement number, defined as the ratio of the theoretical departing bubble diameter to the channel diameter, i.e.,

$$C_o = \frac{\sqrt{[\sigma/(g(\rho_l - \rho_v))]}}{d} \tag{3.12}$$

to define the transition to micro-channels flow. Based on a statistical analysis of two phase heat transfer coefficient data and comparison to correlations provided by Liu and

Winterton [31], Cooper [32,33], Lazarek and Black [34], and Tran et al [35], Kew and Cornwell determined that, for confinement numbers greater than 0.5, the measured heat transfer coefficients departed significantly from the values predicted by the relevant conventional channel correlations. They thus chose Co= 0.5 as the transition criteria for micro-channel behavior. It is interesting to note that, in the present study, the confinement number Co takes the values of 4.6, 2.3 and 0.93 (all higher than 0.5) for HFE-7100 with 100-, 200- and 500-micron channels, respectively.

Forced flow of dielectric liquids with phase change in heated microgap channels had been recently the subject of many researches especially in the chemical, nuclear and mechanical engineering fields. Although the present study focuses the thermal characteristics of a chip-scale non-ideal and very short uniformly heated microgap channel with dielectric fluid HFE-7100, it is nonetheless, worth summarizing some of the available research data on similar refrigerants, flow or geometry parameters. Lee and Lee [36], investigated two-phase heat transfer in a 300mm long and 20mm wide horizontal rectangular gap with hydraulic diameters of 0.8mm-3.6mm using R113 refrigerant. They reported the dominance of the annular flow regime and gathered 491 heat transfer coefficient data points in the range of 5 kW/m^2K for a mass flux range of 52-208 $Kg/m^2.s$ with total pressure drop of 40 kPa. Yang and Fujita [37] used R113 in a similar but somewhat shorter, 100mm long and 20mm wide horizontal rectangular gap with hydraulic diameter of 0.4 mm-3.6 mm. Their 292 data points reported heat transfer coefficients of up to 6 kW/m^2K for mass fluxes in the range of 100 Kg/m^2s

subject to a heat flux of 2 W/cm^2 heat flux. Cortina-Diaz and Schmidt [38] investigated flow boiling heat transfer using n-Hexane and n-Octane in a 12.7mm by 0.3 mm channel with 0.6 mm hydraulic diameter. They reported heat transfer coefficient of 6 kW/m^2K in the range of a 100 Kg/m^2s mass flux and 2-4 W/cm^2 heat flux.

Madrid et al. [39] explored the behavior of HFE-7100 in a 40 parallel channel vertical rectangular channel mini cooler. The channels were 220mm long with a 0.84mm hydraulic diameter. Their 258 data points indicated a highest heat transfer coefficient value of 5.7 kW/m^2K at 71-191 Kg/m^2s mass flux range and 0.17-0.46 W/cm^2 heat flux range. A common conclusion from these studies is the heat transfer coefficient limit of around 6 kW/m^2K at the range of 50-200 Kg/m^2s mass flux and subject to low heat flux of 1-2 W/cm^2. The present study focuses on a larger range of mass fluxes of up to 1500 kg/m^2s and heat fluxes up to 50 W/cm^2.

3.2.2. Two-phase flow regime modeling

The flow of two-phase (vapor and liquid) mixture in pipes or channels has special characteristics and can take different forms, i.e., flow regimes, depending on the distinct vapor/liquid distributions. Four primary two-phase flow regimes, namely, Bubble, Intermittent, Stratified and Annular, as well as numerous sub-regimes, have been identified in the literature [20]. Bubble flow is associated with uniform distribution of small spherical bubbles within the liquid phase. Intermittent flow is characterized by the flow of liquid plugs separated by elongated slug-shape gas bubbles. Stratified flow is

characterized by the liquid flowing along the channel's lower surface and vapor flows above. Annular flow occurs when the liquid flows in a thin layer along the channel walls while the vapor flows in the channel center creating a vapor core. These flow regimes are graphically shown in Figure (11) as they progress axially along a horizontal channel length.

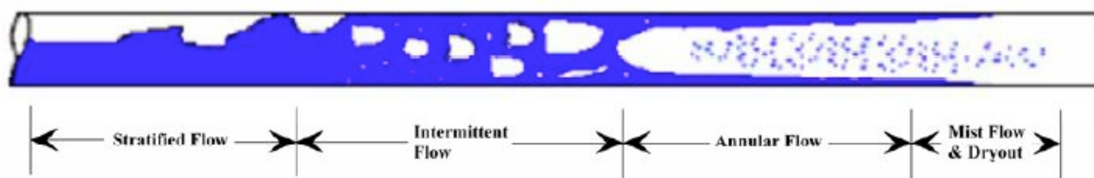

Figure 11: Two-phase Flow regimes in horizontal channel [20].

While the literature contains many approaches to mapping these vapor/liquid flow regimes and makes use of various two-phase thermo-fluid parameters, Taitel and Dukler [40] pioneered physics-based flow regime mapping using first-principle, analytical equations. Their approach most often represented on coordinates of liquid and vapor superficial velocity, respectively, has continued to evolve [41] and is today widely used for predicting and analyzing two-phase flow in tubes and channels.

The Taitel and Dukler (TD) map of two-phase flow in pipes identifies the boundaries among the four dominant flow regimes, i.e., stratified, intermittent, bubble and annular. The TD flow regime map schematically shows, in Figure (12), for the 100-micron channel with hydraulic diameter D_h of 200 micron, flowing HFE-7100 fluid, used in the present study, the four flow regimes along with transition lines between one regime and another as

relative functions of the liquid and vapor superficial velocities. The stratified flow regime occupied the lower corner of the map at low superficial vapor velocity and low superficial liquid velocity. Moderate superficial liquid velocity leads to intermittent flow while further increase in superficial liquid velocity, at similar low superficial vapor velocity leads to bubble flow. Annular flow occupies the right triangle-shape part of the map as both superficial gas and liquid velocities increase from their values at bubble and intermittent flow regimes.

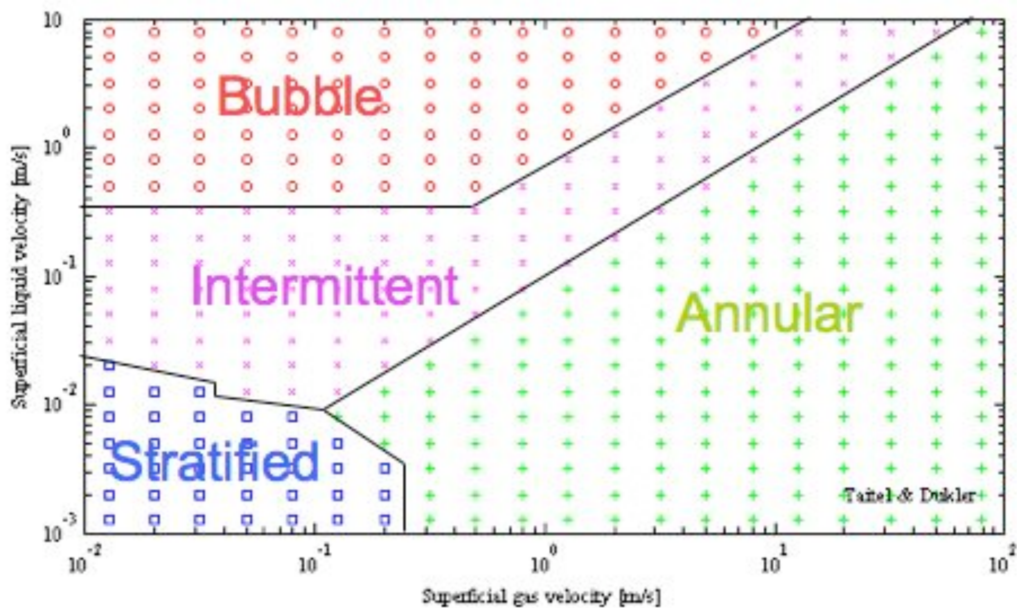

Figure 12: Taitel-Dukler Flow Regime Map Showing, Stratified, Bubble, Intermittent and Annular Flow Regimes- 100-micron Channel D_h=200 micron, HFE-7100 Fluid.

These transition lines reflect the distinction between surface tension driven regimes, such as bubble and intermittent flows, and shear force driven regimes, such as stratified and

annular. Furthermore, the TD flow regime map relies on adiabatic models that ignore the thermal interactions between phases, the pipe and the environment all of which are present in the diabatic systems. This dependence of adiabatic models makes the transition lines of the TD model less accurate when high heat fluxes are applied at the channel/pipe wall [42].

In addition to the TD flow regime map, other analytical approaches of flow regime transitions are available in the literature. Amongst them are the Weismann et al method [43], and Tabatabai and Faghri method [44] that proposed a modification to the TD map based on a criterion for the transition from surface tension dominated behavior to shear dominated behavior. These approaches compliment the traditional empirical flow regime maps obtained for water-steam, and other industrial fluids and cannot be easily extrapolated to microchannels and refrigerants.

Rahim and Bar-Cohen [20] conducted a detailed analysis of microchannel and microgap heat transfer data for two-phase flow of refrigerants and dielectric liquids, gathered from the open literature and sorted by the Taitel and Dukler flow regime mapping methodology, reveals the existence of the three primary flow regimes, i.e. Bubble, Intermittent, and Annular, along with Stratified flow for horizontal configurations, in miniature channels. However, the annular flow regime is found to be the dominant regime for this thermal transport configuration and its prevalence is seen to grow with decreasing channel diameter and to become dominant for refrigerant flow in channels below 0.1mm diameter.

3.2.3. Characteristics of two-phase heat transfer in micro channels

The literature data of two-phase heat transfer coefficients suggest a characteristic M-shaped heat transfer coefficient variation with quality (or superficial velocity) for the flow of refrigerants and dielectric liquids in miniature channels. The inflection points in this M-shaped curve are seen to equate approximately with flow regime transitions, including a first maximum at the transition from Bubble to Intermittent flow and a second maximum at moderate qualities in Annular flow, just before local dryout begins. This characteristic behavior is shown in Figure 13, taken from the comprehensive work done by Rahim et al [20], on the data from Yang and Fujita [37] and Cortina-Diaz and Schmidt [38].

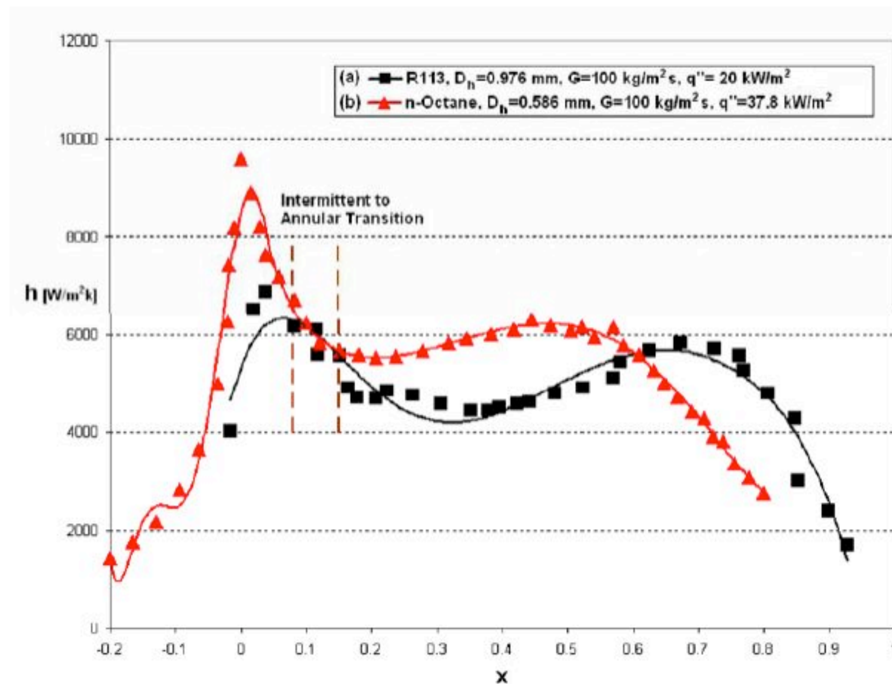

Figure 13: Heat transfer coefficient data from Yang and Fujita [37] and Cortina-Diaz and Schmidt [38] showing the characteristic M-shape behavior [20].

3.2.4. Heat Transfer Correlations

Thome and Collier, in their book [45], discussed the classical two-phase heat transfer correlations available in the literature and identified the prominent role played by the two-phase Reynolds number, based on the liquid fraction of the mass flux in the channel, in attempts to correlate the two-phase heat transfer coefficient. Kim, et al [19], analyzed two-phase microgap heat transfer in simple geometries and correlated to Chen and Shah correlations. Rahim and Bar-Cohen [20] conducted detailed analysis of microchannel/microgap heat transfer data for two-phase flow of refrigerants and dielectric liquids, gathered from the open literature. They analyzed the predictive accuracy of five classical two-phase heat transfer correlations [45] for miniature channel flow was examined. These classical correlations include Chen [46], Kandlikar [47], Gungor-Winterton [48], Gungor-Winterton Revised [49] and Shah correlations [50]. Selecting the best fitting of the classical correlations for each of the flow regime categories is seen to yield predictive agreement with regime-sorted heat transfer coefficients that does not depart significantly from the agreement found in large pipes and channels.

Comparison of a sample of microgap refrigerant data to existing classical correlations reveals that the Chen correlation provides overall agreement to within a standard deviation of 38% for the entire data set [20]. However, classification of the data by flow regime does allow for improved predictive accuracy. The authors have shown that the dominant, low quality Annular data could be correlated by the Chen

correlation to within an average discrepancy of just 24%, while the Shah correlation provides agreement to within an average discrepancy of 32% (vs. 72% for Chen) for data in the Intermittent regime, and the modified Gungor-Winterton correlation to approximately 37% (vs. 39% for Chen) for the moderate-quality annular flow data.

In the present work, the two correlations for two-phase flow heat transfer prediction, namely, the Chen and Shah correlations, were used as reference points to compare against the various experimental data obtained.

Chen Correlation

The starting point for the Chen correlation is:

$$h = h_{mic} + h_{mac} \tag{3.13}$$

The macroscopic contribution was calculated using the Dengler Addoms correlation with a Prandtl number correction factor to generalize the correlation beyond water as the working fluid.

$$h_{mac} = h_l F\left(X_{tt}\right) \tag{3.14}$$

Here F is an acceleration factor and the single phase liquid-only convective coefficient (h_l) is calculated via the Dittus-Boelter equation:

$$h_l = 0.023\left(\frac{k_l}{D}\right)\mathrm{Re}_l^{0.8}\,\mathrm{Pr}_l^{0.4} \qquad (3.15)$$

where

$$\mathrm{Re}_l = \frac{G(1-x)D}{\mu_l} \qquad (3.16)$$

The microscopic contribution was calculated using the Forster-Zuber correlation for pool boiling with an additional correction factor in the form of a suppression factor, S:

$$h_{mic} = 0.00122\left[\frac{k_l^{0.79} c_{pl}^{0.45} \rho_l^{0.49}}{\sigma^{0.5} \mu_l^{0.29} h_{lv}^{0.24} \rho_v^{0.24}}\right]\left[T_w - T_{sat}(P_l)\right]^{0.24}\left[P_{sat}(T_w) - P_l\right]^{0.75} S \qquad (3.17)$$

The suppression factor, S is required to account for the fact that nucleation is more strongly suppressed when the macroscopic convective effect increases in strength and the wall superheat diminishes. To calculate this suppression factor, Chen used a regression analysis of the data to fit S as a function of a two phase Reynolds number defined as:

$$\mathrm{Re}_{tp} = \mathrm{Re}_l\left[F(X_{tt})\right]^{1.25} \qquad (3.18)$$

Chen originally presented the suppression data in graphical format. However, Collier [45] found the following empirical fit for the suppression factor (which is used in this study):

$$S(\mathrm{Re}_{tp}) = \left(1.25 + 2.56x10^{-6}\,\mathrm{Re}_{tp}^{1.17}\right)^{-1} \tag{3.19}$$

Collier, also, provided empirical fits for the $F(X_{tt})$ data in the form:

$$\begin{aligned} F(X_{tt}) &= 1 && \text{for } X_{tt}^{-1} \leq 0.1 \\ F(Xtt) &= 2.35\left(0.213 + \frac{1}{X_{tt}}\right)^{0.736} && \text{for } X_{tt}^{-1} > 0.1 \end{aligned} \tag{3.20}$$

The Martinelli parameter X_{tt} is calculated as:

$$X_{tt} = \left(\frac{1-x}{x}\right)^{0.9}\left(\frac{\rho_g}{\rho_l}\right)^{0.5}\left(\frac{\mu_l}{\mu_g}\right)^{0.1} \tag{3.21}$$

Shah Correlation

In the Shah Correlation the heat transfer coefficient takes the form:

$$\psi_s = \frac{h}{h_l} = f(Co, Bo, Fr_{le}) \tag{3.22}$$

With the relevant dimensionless parameters provided as:

$$Co = \left(\frac{1-x}{x}\right)^{0.8}\left(\frac{\rho_v}{\rho_l}\right)^{0.5} \tag{3.23}$$

$$Bo = \frac{q''}{Gh_{lv}} \tag{3.24}$$

$$Fr_{le} = \frac{G^2}{\rho_l^2 gD} \tag{3.25}$$

The original Shah correlation was presented in graphical form. In 1982 Shah provided a computational representation of his correlation. This computational representation was outlined as follows:

$$N_s = Co \qquad \text{for } Fr_{le} \geq 0.04 \tag{3.26}$$

$$N_s = 0.038 Fr_{le}^{-0.3} Co \qquad \text{for } Fr_{le} < 0.04 \tag{3.27}$$

$$F_s = 14.7 \qquad \text{for Bo} \geq 11\text{E-4} \tag{3.28}$$

$$F_s = 15.4 \qquad \text{for Bo} < 11\text{E-4} \tag{3.29}$$

$$\psi_{cb} = 1.8 N_s^{-0.8} \tag{3.30}$$

For Ns > 1

$$\psi_{nb} = 230 Bo^{0.5} \qquad \text{for Bo} > 0.3\text{E} - 4 \tag{3.31}$$

$$\psi_{nb} = 1 + 46 Bo^{0.5} \quad \text{for Bo} \leq 0.3\text{E} - 4 \tag{3.32}$$

$$\psi_s = \max(\psi_{cb}, \psi_{nb}) \tag{3.33}$$

For Ns =< 1

$$\psi_{bs} = F_s \text{Bo}^{0.5} \exp\left(2.74 \text{N}_\text{s}^{-0.1}\right) \quad \text{for } 0.1 < \text{N}_\text{s} \leq 1 \tag{3.34}$$

$$\psi_{bs} = F_s \text{Bo}^{0.5} \exp\left(2.47 \text{N}_\text{s}^{-0.15}\right) \quad \text{for N}_\text{s} \leq 0.1 \tag{3.35}$$

3.2.5 Unresolved issues in two-phase behavior in microgaps

Although there are numerous studies and data on two-phase heat transfer in miniature and micro channels in the literature, nearly all of these address “ideal” channels, i.e., channels that are long enough to produce developed flow and have a uniform heat flux

applied along the channel walls. The application of these results and correlations to the direct cooling of advanced microelectronic chips in non-ideal channels, with non-uniform heating and relatively short channel lengths, requires dealing with several unresolved issues.

As discussed in Chapters 1-2, advanced IC's and especially contemporary microprocessor architectures experience a high level of transistor modularity that directly results in non-uniform heating or zonal heating at the die junction (power) plane. This advancement has resulted in substantial die heating non-uniformity and has necessitated use of die power (heating) maps to correctly determine the chip temperature distribution and evaluate the effectiveness of applied thermal management solutions. . Since the development of the thermal boundary layer in convective heat transfer and wall ebullition in two-phase flow depend strongly on the local wall heat flux, it can not be assumed a priori that the available uniform wall heat flux correlations for the heat transfer coefficients in convection and flow boiling, respectively, will correctly predict "real" microgap channel behavior. Furthermore, the focus on miniaturization and compactness in the development of microgap and microchannel coolers for microelectronic devices results in the design of relatively short channels with strongly developing flow and significant conductive/convective conjugate effects in the thermally conductive semi-conductor chips. The available conventional correlations, with isoflux or isothermal (uniform) boundary conditions are again inappropriate for predicting the thermofluid behavior of such actual

microgap cooler channels. The modeling approached for determining the heat transfer coefficients prevailing in such channels will be discussed in detail in Chapter 5.

Chapter 4:

Experimental Apparatus

4.1 Overall Description

An experiment setup was designed and built for conducting the experimental aspects of this research. The setup was built around the thermal test chip based on the Intel's "Merom" microprocessor [51]. The system was designed to enable flow boiling. An overall 3-D image of the setup is shown in Figure 14. Schematic layout of the overall setup is also shown in Figure 15, including the boiling chamber, filling/venting port, condenser (heat exchanger,) pump, flow meter, inline heater, absolute and differential pressure transducers and various thermistors including channel (boiling chamber) inlet and outlet.

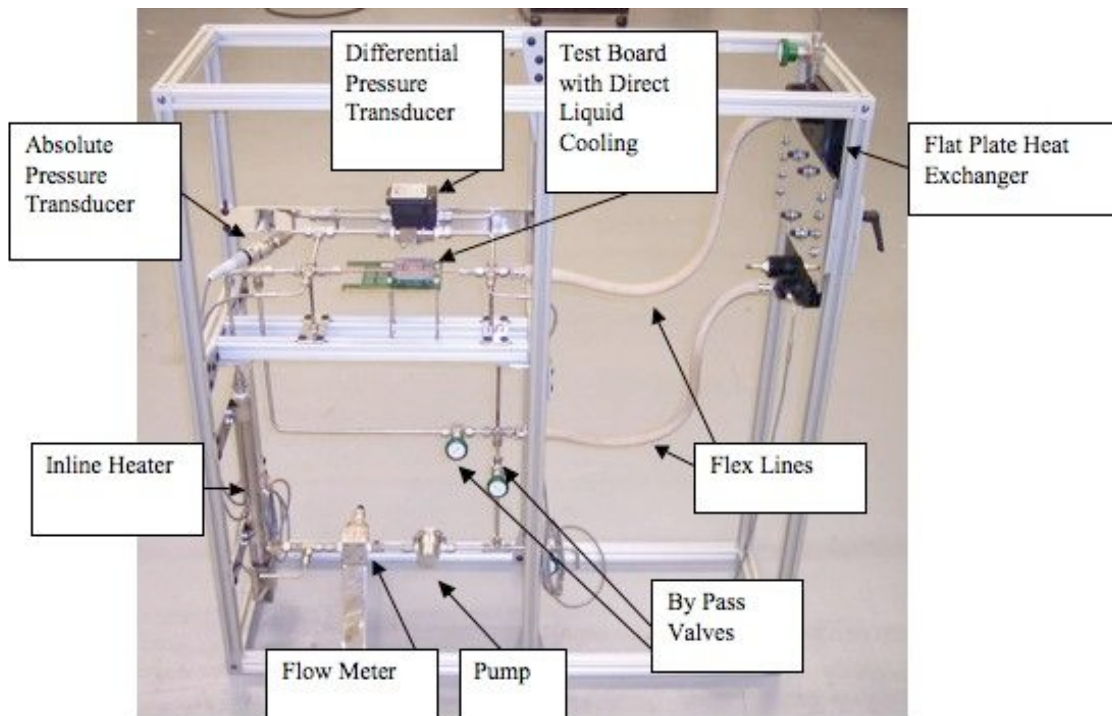

Figure 14: Two-Phase Microgap Channel Test Apparatus

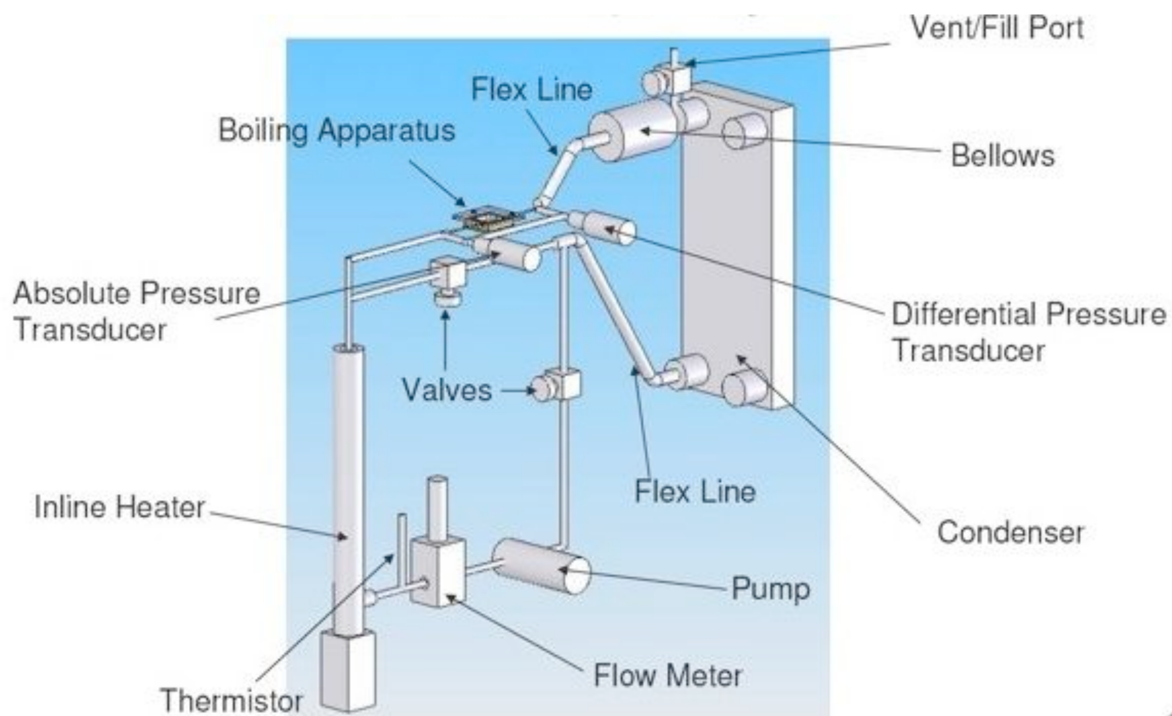

Figure 15: Design Schematics of the Two-Phase Microgap Channel Apparatus

The flow meter is a Kobold Pelton-Wheel Flow meter. It requires a 5V activation voltage and puts out 4mA to 20mA representing the number of turns that the wheel makes per second. The flow meter is equipped with an optical sensor that measures the RPM's of the wheel.

The Pump is a KAG M42x30/I positive displacement, mag-drive, gear pump. It supplies up to around 100 psi positive pressures or a maximum of 9 ml/s volumetric flow rate.

The absolute pressure sensor sends a current range from 4mA to 20mA that linearly represent pressures from -15 psi to 45 psi or -1 atm to 3 atm. The data acquisition system can read the current that the pressure sensor puts out.

The test channel cross-pressure transducer is very similar to the absolute Pressure sensor. The only difference is that it relates a voltage to pressure instead of a current to pressure. It emits a voltage between 0.05 and 5.05 volts that correspond to a pressure differential of 0-2 psi (0-13.8 kPa).

The inline heater is used for preheating the fluid coming into the test channel to whatever desired temperature value. The preheating is done by varying the input voltage to the heater as the later has a predetermined electrical resistance. The preheating process is usually required to produce saturated flow boiling at the entrance of the test channel.

The condenser is a flat plate heat exchanger that can be either cooled by natural convection air or by forced convection water. The later process is usually used in flow boiling in order to condensate the coolant vapor into liquid before it passes again through the pump.

Figure 16 shows this process of externally water cooling the condenser and condensing the working fluid before it flows back to the pump.

Figure 16: External Water-Cooled Condenser for the two-Phase Microgap Channel Apparatus.

A fluid reservoir, as shown in Figure 17, is used in certain high-pressure tests as a pressure relief to the system mainly for saturated boiling.

Figure 17: Pressure Relief Reservoir for the two-Phase Microgap Channel Apparatus.

4.2 Calibration of flow meter

The Pelton wheel flow meter measures flow rate by counting the revolutions of a paddle wheel immersed in the pumped fluid. The number of revolutions per unit time is translated into a flow measurement. The flow meter outputs an electric current value that is proportional to the wheel's RPM. The RPM is converted into flow rate throughout the measurement process. It is thus imperative to calibrate the flow meter against the fluid under consideration as fluid properties, including density and viscosity, influence the flow meter current output. The outcome of the calibration process is to establish the current vs. flow rate calibration curve that is later

programmed into the data acquisition system such that the output by the data file would be the correct fluid flow rate.

Figure18 shows the flow meter current vs. flow rate calibration curves, extracted via this method, for water and HFE-7100, respectively.

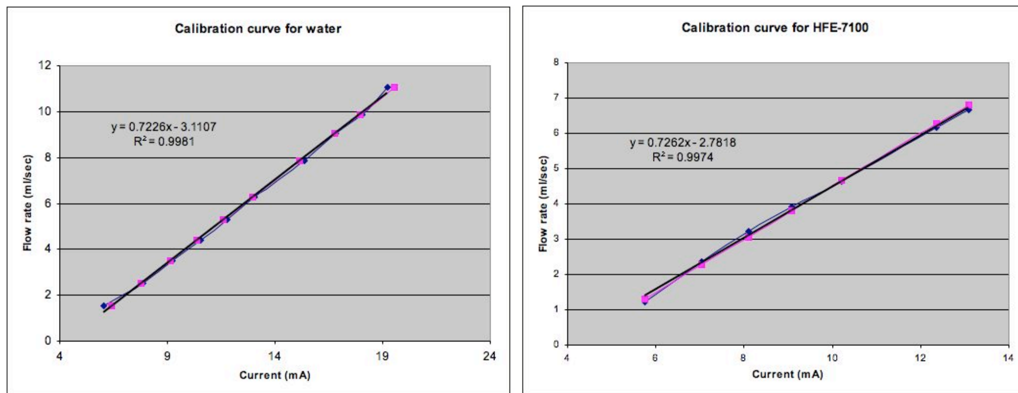

Figure 18: Kobold Flow Meter Calibration Curves for Water and HFE-7100.

4.3 Chip Thermal Test vehicle

The Thermal Test Vehicle (TTV) is a thermal test chip emulating the Intel Merom microprocessor. The chip is packaged in a C4 flip chip die mounted via a BGA layer on an organic substrate. The TTV is depicted in Figure 19.

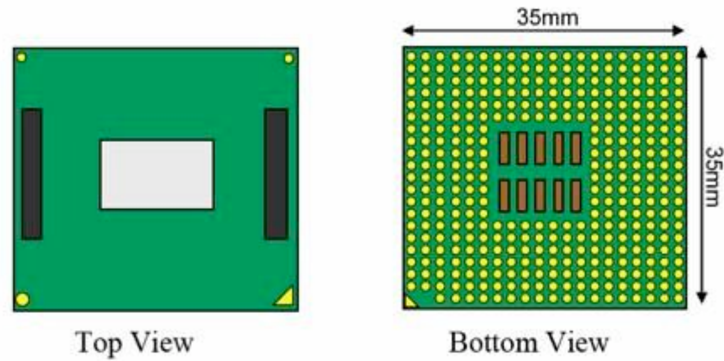

Figure 19: Intel's Merom Processor Thermal Test Vehicle (TTV) [51].

The TTV is equipped with temperature sensors (Figure 20) that are pre-calibrated using a four-wire resistance calibration method. Power dissipation on the test chip is generated by powering, via external power supplies, the three serpentine-type heater zones (Figure 21) embedded in the chip junction plane.

Figure 20: Intel's TTV Schematic Three Different Power (Heating) Zones with Locations of Temperature Sensors.

Figure 21: Intel's TTV Serpentine-Type Heating Zones and Locations of Temperature Sensors [51].

These three zones, superimposed in Figure 22, at the die area, emulate the half-die and the two quadrants of the microprocessor. The TTV is enabled to run the heater zones together to produce uniform power dissipation in the plane pf the resistors or the zones can be run individually or in binary combinations to produce various non-uniform power dissipation distributions. The heat flux achievable for uniform power dissipation is 50 W/cm^2 and it can rise to 200 W/cm^2 for non-uniform power dissipation where the full power is concentrated on one quadrant of the chip area.

Figure 22: Assembled Intel TTV Showing Locations of the Three Heater Zones.

The TTV is mounted via a socket connector onto a test board, as shown in Figure 23, that provides the connection necessary to power the TTV chip and read the resistors from the temperature sensors and convert them into temperature values through the data acquisition system.

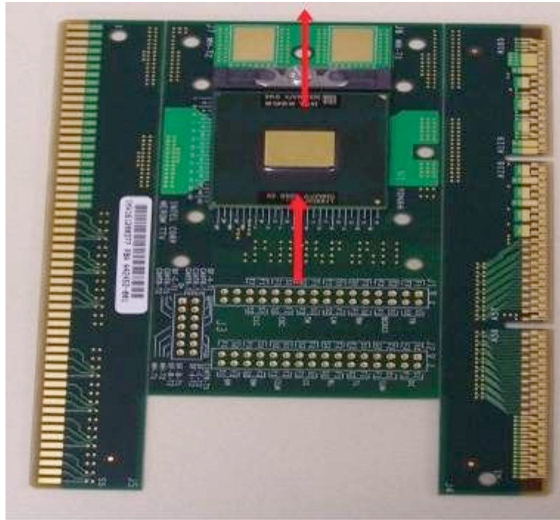

Figure 23: Intel's TTV Board.

4.4 The microgap test channel

An hermetically sealed fluid chamber is assembled on the TTV die to allow the coolant to flow in direct contact with the silicon die. The chamber is constructed with a copper base that is attached to the TTV board via an O-ring. The copper channel (shown in Figures 24, 25) is covered at the top by a plastic cap and attached via a second O-ring. The fluid height in the channel, i.e., the fluid gap, is determined by sandwiched plastic inserts that have variable thicknesses to produce the desired fluid gap, as shown in Figure 25.

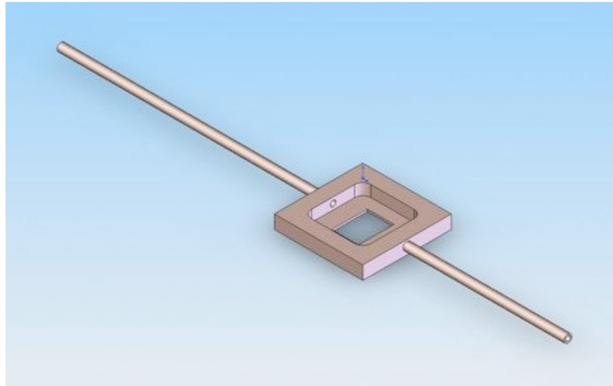

Figure 24: TTV Cooper Channel

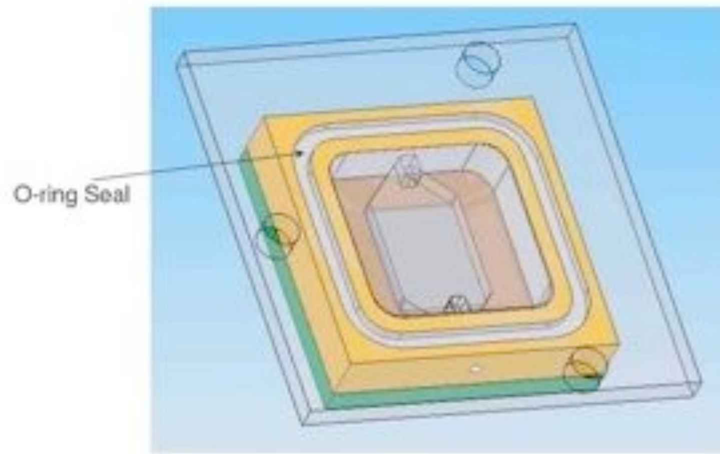

Figure 25: Hermetically Sealed Microgap Channel.

4.5 Chip TTV - Sensor Calibration Procedure

The sensor calibration process is a necessary step in converting the sensor resistances to the actual temperatures. This process, i.e., four-wire resistance calibration, involves placing the TTV in a constant temperature bath, soaking the unit for a sufficient amount of time to establish l thermal equilibrium and measuring the resistance of the temperature sensor along with the temperature of the fluid bath. This step is repeated at four different fluid bath temperatures. Finally, a linear regression is performed to establish the resistance vs. temperature calibration curve. Figure 26, shows a typical sensor calibration curve for the four-wire measurement process.

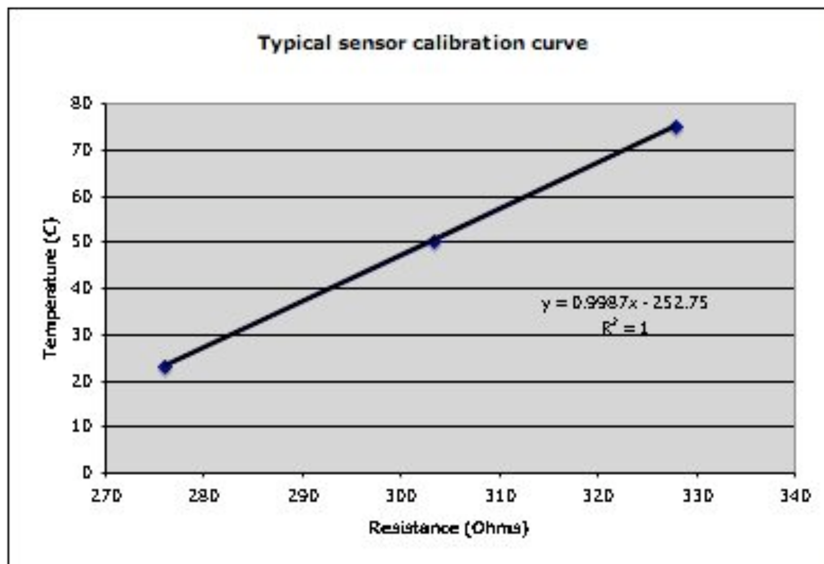

Figure 26: TTV Characteristic Temperature Sensor Calibration.

4.6 Fluid selection and HFE-7100 Novec properties

Water's thermal characteristics including thermal conductivity, specific heat and latent heat of vaporization, make it an ideal and the most popular coolant for a wide variety of thermal management applications. However, water is electrically conductive and could cause device failure and IC shorting, as well as corrosive actions, if a water-cooled thermal management component experiences leakage. The industry, therefore, prefers dielectric fluids for advanced liquid cooling of electronic components.

Historically, the dielectric fluorinerts [52], i.e., the FC family of fluids, along with other refrigerants (such as R134x, etc.) had been extensively used in liquid cooled products. These fluids, however, do not possess good environmental properties, displaying high global warming potential (GWP) and ozone depletion potential (ODP) [52]. The chemical industry led by 3M pioneered a new family of liquid cooling products, Novec, aimed at addressing the environmental and toxicity aspects and characteristics of FC's. 3M™ Novec™ 7100 Engineered Fluid [52], is used in the present work. HFE-7100, chemically known as methoxy-nonafluorobutane (C4F9OCH3), is a clear, colorless and low-odor fluid intended to replace ozone-depleting substances (ODSs) and compounds with high global warming potential (GWP). This proprietary fluid has zero ozone depletion potential and other favorable environmental properties (see Table 1). It has one of the best toxicological profiles (Table 2) of CFC replacement materials, with a time-weighted average exposure guideline of 750 ppm (eight hour average). Table 3, shows published properties from

3M on both FC and Novec family of fluids.

The boiling point and low surface tension of Novec HFE-7100 fluid as well as its chemical and thermal stability, non-flammability and low toxicity make it ideal for use in liquid cooling industrial applications. Table 4, shows the thermal and fluid properties of HFE-7100 compared to water and other refrigerants used for liquid cooling. Figure 27, shows the HFE-7100 temperature-dependent properties used in the present work.

Properties	Novec 7100	CFC-113	HCFC-141b	HCFC-225 ca/cb[1]	HFC-4310mee
Ozone Depletion Potential[2]–ODP	0.00	0.80	0.10	0.03	0.00
Global Warming Potential[3]–GWP	320	6000	700	180/620	1700
Atmospheric Lifetime–ALT (yrs)	4.1	85	9.2	2.1/6.2	17.1
Flashpoint	None	None	None	None	None
Flammability Range in Air	None	None	7.6-17.7[4]	None	None
Exposure Guidelines, ppm (8 hr. time-weighted average)	750	1000	500	50	200
Exposure Ceiling (ppm)	None	None	None	None	400
Acute Toxicity (4 hr. LC_{50} [Rat])	>100,000	55,000	62,000	37,000	11,000

[1] HCFC-225 ca/cb ratio is 45/55 [2] CFC-11 = 1.0 [3] GWP–100 year Integration Time Horizon (ITH)
[4] Vol % by ASTM E681-94 @ 100°C

Table 1: HFE-7100 Environmental Properties [52].

Properties	Novec 7100
Acute lethal inhalation concentration	>100,000 ppm (4 hour)
Oral	Practically non-toxic (>5 g/kg)
Eye irritation	Practically non-irritating
Skin irritation	Minimally irritating
Skin sensitization	Not a skin sensitizer
Developmental toxicity	Detailed results are available
Mutagenicity	Negative in the three assays conducted
Cardiac sensitization	No signs of sensitization at exposures up to 100,000 ppm
Ecotoxicity testing	Complete–very low aquatic toxicity
90-day inhalation	750 ppm exposure guideline Detailed results are available

Table 2: HFE-7100 Toxicity Properties [52].

3M™ Fluorinert™ Electronic Liquids

(All values determined at 25°C unless otherwise specified)

	FC-87	FC-72	FC-84	FC-77	FC-3283	FC-40	FC-43	FC-70
Selection Guidelines (Equipment operating temperature)	Low	Low	Low	Med	Med	High	High	High
Boiling Point (°C)	30	56	80	97	128	155	174	215
Pour Point (°C)	-115	-90	-95	-110	-50	-57	-50	-25
Vapor Pressure (Pa)	81.1×10^{3}	30.9×10^{3}	10.6×10^{3}	5.62×10^{3}	1.44×10^{3}	432	192	15
Density (kg/m³)	1650	1680	1730	1780	1820	1850	1860	1940
Coefficient of Volume Expansion (°C⁻¹)	0.0015	0.00156	0.0015	0.00138	0.0014	0.0012	0.0012	0.0010
Kinematic Viscosity (cSt)	0.28	0.38	0.53	0.72	0.75	1.8	2.5	12
Absolute Viscosity (centipoise)	0.45	0.64	0.91	1.3	1.4	3.4	4.7	24
Specific Heat (J kg⁻¹ °C⁻¹)	1100	1100	1100	1100	1100	1100	1100	1100
Heat of Vaporization @ B.P. (J/g)	103	88	90	89	78	68	70	69
Dielectric Strength (kV, 0.1" gap)	48	38	38	40	43	46	42	40
Dielectric Constant (1 KHz)	1.73	1.75	1.80	1.90	1.89	1.90	1.90	1.98
Volume Resistivity (Ω cm)	10^{15}	10^{15}	10^{15}	10^{15}	10^{15}	10^{15}	10^{15}	10^{15}

3M™ Novec™ Engineered Fluids

(All values determined at 25°C unless otherwise specified)

	HFE-7100	HFE-7200	HFE-7500*
Selection Guidelines (Equipment operating temperature)	Low	Low	Med
Boiling Point (°C)	61	76	128
Pour Point (°C)	-135	-138	-110
Vapor Pressure (Pa)	26.8×10^{3}	15.7×10^{3}	2.1×10^{3}
Density (kg/m³)	1510	1420	1610
Coefficient of Volume Expansion (°C⁻¹)	0.0018	0.0016	0.0013
Kinematic Viscosity (cSt)	0.38	0.41	0.77
Absolute Viscosity (centipoise)	0.58	0.58	1.240
Specific Heat (J kg⁻¹ °C⁻¹)	1180	1220	1130
Heat of Vaporization @ B.P. (J/g)	112	119	88.5
Dielectric Strength (kV, 0.1" gap)	~40	~40	~40
Dielectric Constant (1 KHz)	7.4	7.3	5.8
Volume Resistivity (Ω cm)	10^{8}	10^{8}	10^{8}

Table 3: Characteristics of 3M's Fluorinert and Novec Fluids [52].

Property	HFE-7100	FC-72	R-134a	R-245a	Water
Chemical Formula	C4F9OCH3	C6F14	C2H2F4	CHF2CH2CF3	H2O
Boiling Point (1atm) [°C]	61	56	-26	14.9	100
Density [kg/m³]	1510	1680	1377	1366	1000
Surface Tension [dyne/cm]	12.3	12	15.3	-	58.9
Kinematic Viscosity [cSt]	0.38	0.38	2.74	3.43	2.87
Latent Heat of Vaporization [kJ/kg]	121.2	88	212.1	197.3	2257

Specific Heat [kJ/kg.K]	1.25	1.1	1.28	1.31	4.08
Thermal Conductivity [W/m.K]	0.062	0.057	0.105	0.084	0.681
Dielectric Strength [kV/mm]	11	15	7	-	-
Dielectric Constant	7.4	1.76	9.5	-	78.5

Table 4: HFE-7100 Thermo-Physical Properties Compared to Other Coolants.

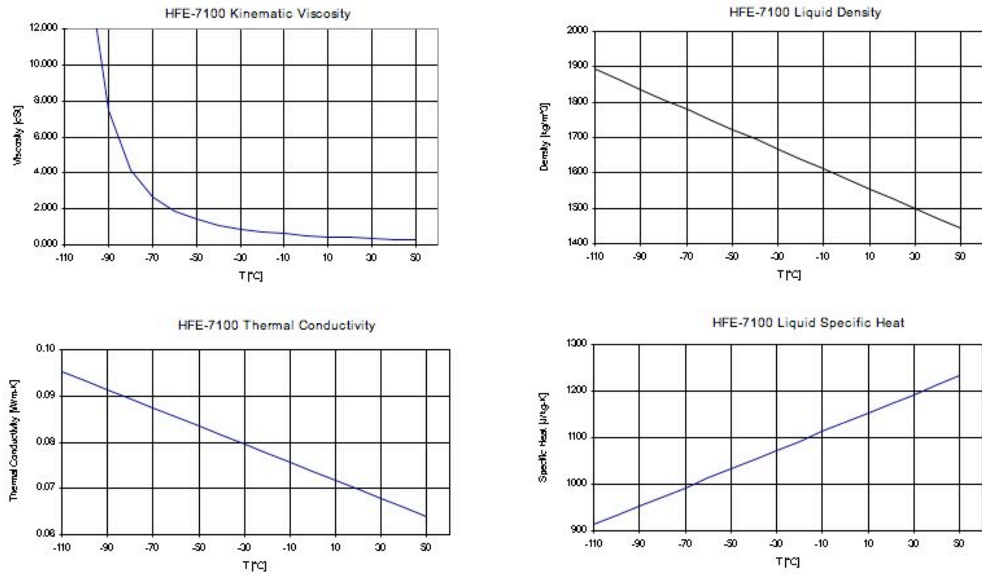

Figure 27: HFE-7100 Thermal and Fluid Properties [52].

Chapter 5:

CFD Model and Simulation

5.1 Introduction

Thermal issues have become a major concern in electronics design reflecting the effect of increasing power densities, demands on reliability, and die junction temperature limits. The industry, therefore, has seen an increased focus on the thermal performance of packaging materials, cooling devices, and design and analysis tools. This focus has resulted in the commercial availability of advanced Computational Fluid Dynamics (CFD) tools to solve the simultaneous equations of fluid dynamics and heat transfer or the so-called conjugate heat transfer problem. These tools are based on the finite element, finite difference, or control volume numerical methods to analyze three-dimensional geometries by solving steady state as well as transient governing equations. In the present work, the commercially available CFD package Icepak [53] from Ansys, was used for the modeling of the test microgap cooling channel and solving the fully conjugate heat transfer-fluid problem.

5.2 Equations Solved and Methodology

The governing equations solved in this CFD simulation are the Navies Stokes partial differential equations for the conservation of momentum, along with equations for the

conservation of mass (continuity) and conservation of energy. The three equations take the following forms

$$\nabla \cdot \vec{u} = 0 \tag{5.1}$$

$$\rho \frac{\partial \vec{u}}{\partial t} + \rho(\vec{u} \cdot \nabla)\vec{u} = -\nabla P + \rho \nabla^2 \vec{u} + \rho \vec{g} \beta (T - T_\infty) \tag{5.2}$$

$$\rho c_p \frac{\partial T}{\partial t} + \rho c_p \vec{u} \cdot \nabla T = \nabla \cdot k \nabla T + S \tag{5.3}$$

The conjugate flow and heat solution is obtained using the Boussinesq approximation for buoyancy forces.

$$-g(\rho - \rho_{amb}) = \rho_{amb} g \beta (T - T_\infty) \tag{5.4}$$

Thermal radiation is a non-linear phenomenon and solved for fully by calculating exchange factors for all surfaces and adding an appropriate term to the energy equation.

$$Q = \sigma \varepsilon A T^4 \tag{5.5}$$

The real physical geometry is discretized (Figure 28) into small volumes known as grid cells. The above equations are applied on each cell and implemented as algebraic equations while temperature, pressure and x, y and z fluid velocities are assumed constants for each cell. The algebraic equations are solved for the entire computational domain (the computational grid) iteratively until an acceptable converged solution is found [54].

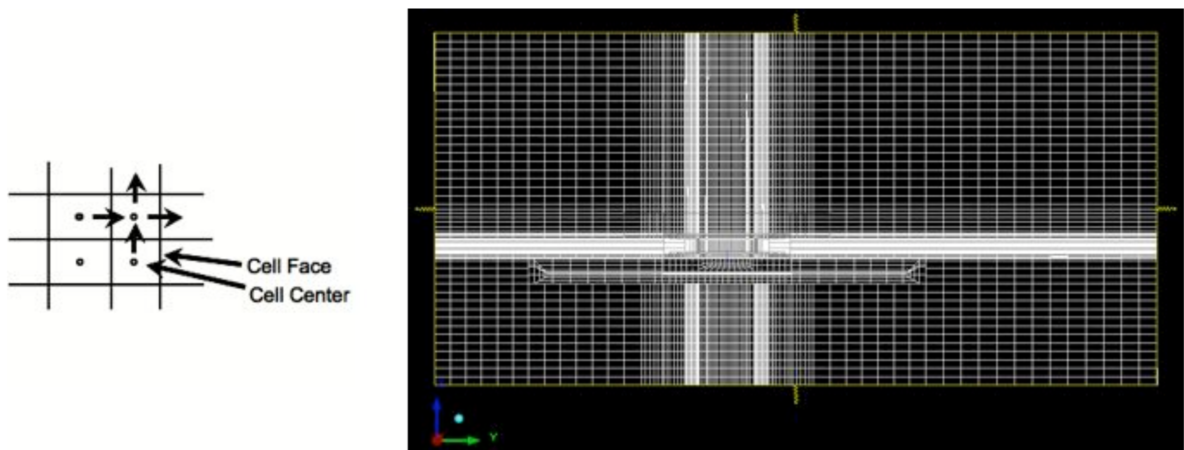

Figure 28: The CFD Computational Grid.

5.3 Model Description and conjugate heat transfer

A Computational Fluid Dynamics (CFD) model was created for the test channel including the entire fluid chamber, silicon die test chip, printed circuit test board and inlet and outlet pipes. The simulation used a fully conjugate heat transfer model, i.e., it solved for heat transfer internal to the channel and external to it involving automatic calculation of convective and radiative hear transfer with both the working fluid and

the ambient room air. A grid sensitivity analysis was conducted to reach a solution that is grid-independent. The computational grid is shown in Figures 29 and 30 for a close-up on the fluid channel and the entire conjugate domain, respectively. Convergence of temperature results for the key chip temperature sensors are shown in Figure 31. The model computational domain reached a grid that is 1.3 million computational cells. Figures 32 and 33 show detailed three-dimensional, XY and YZ views of the computational domain, respectively.

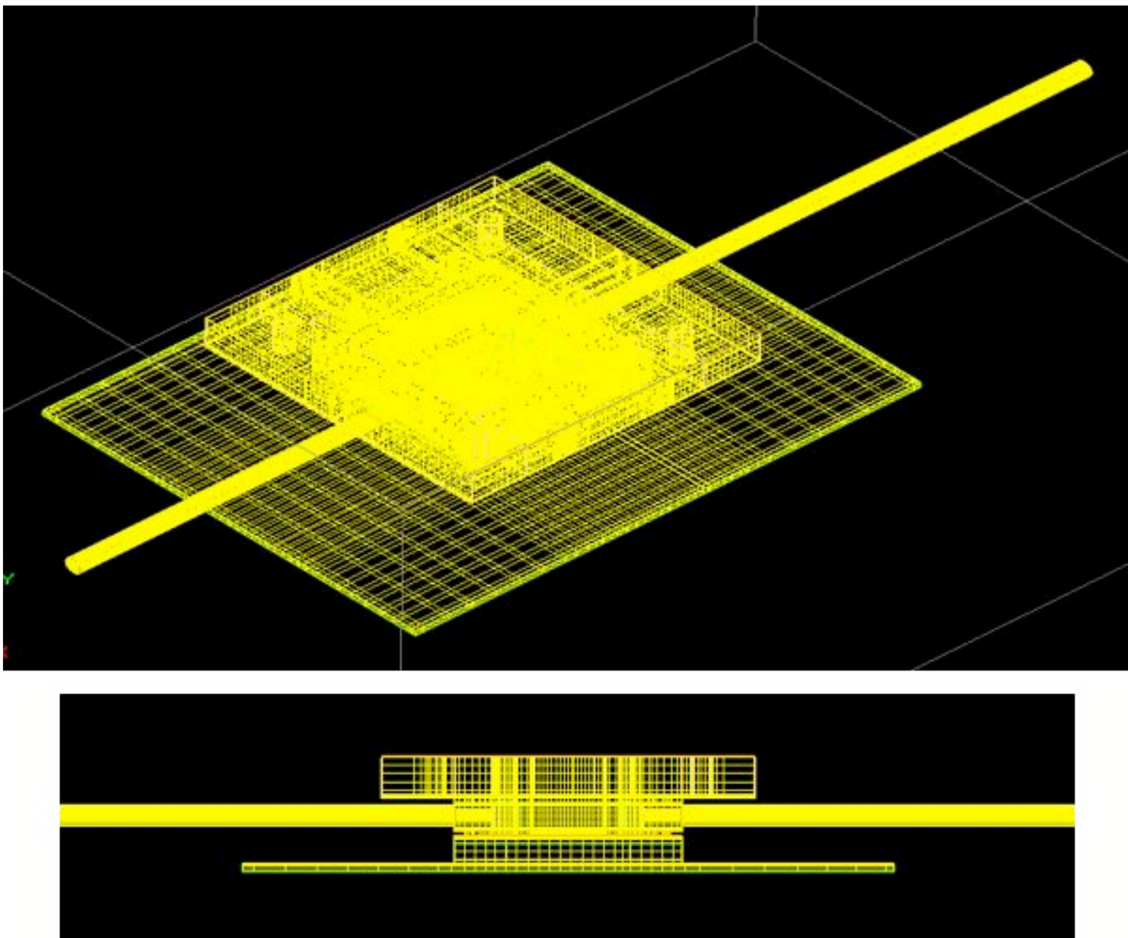

Figure 29: Fluid Channel Grid.

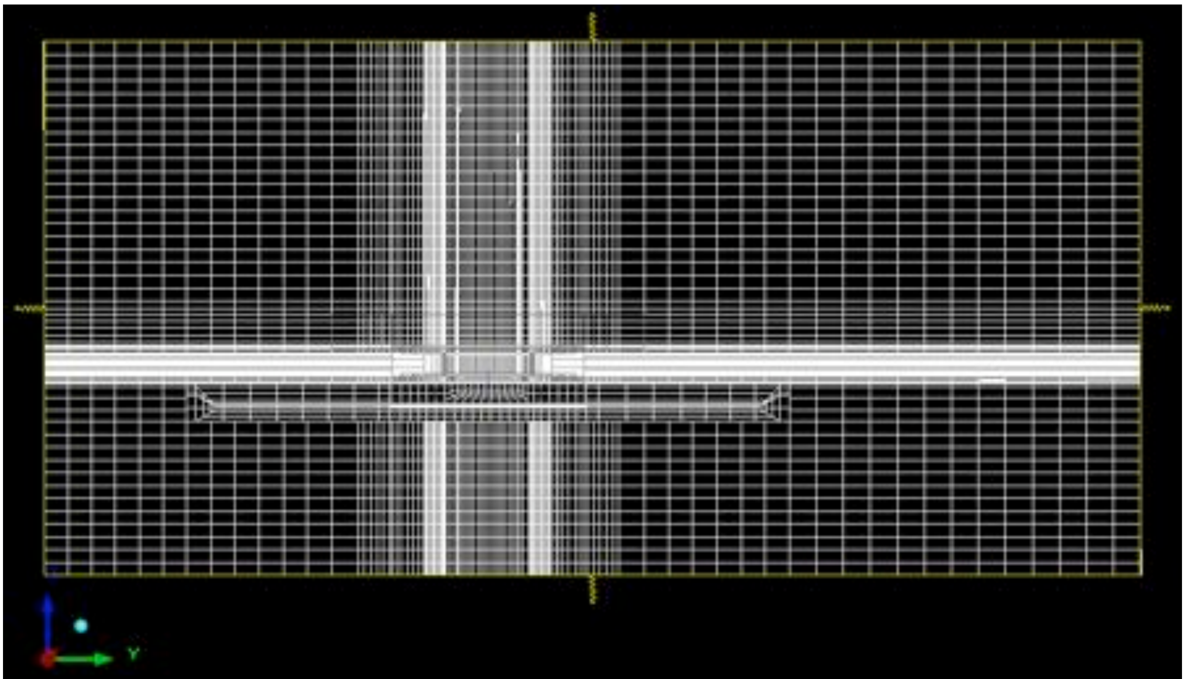

Figure 30: Full Conjugate Domain Grid.

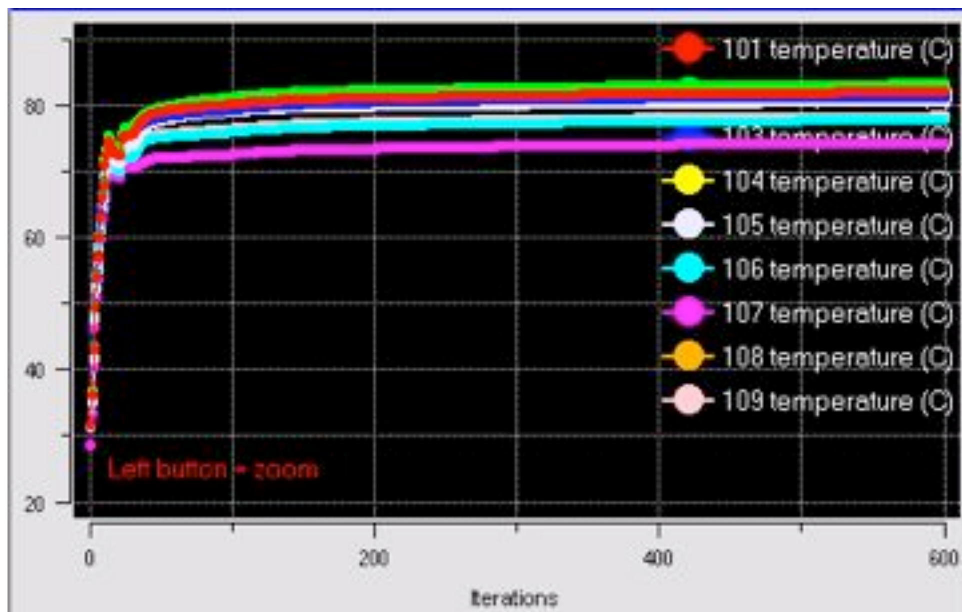

Figure 31: CFD Solution Convergence for Key Temperature Sensors.

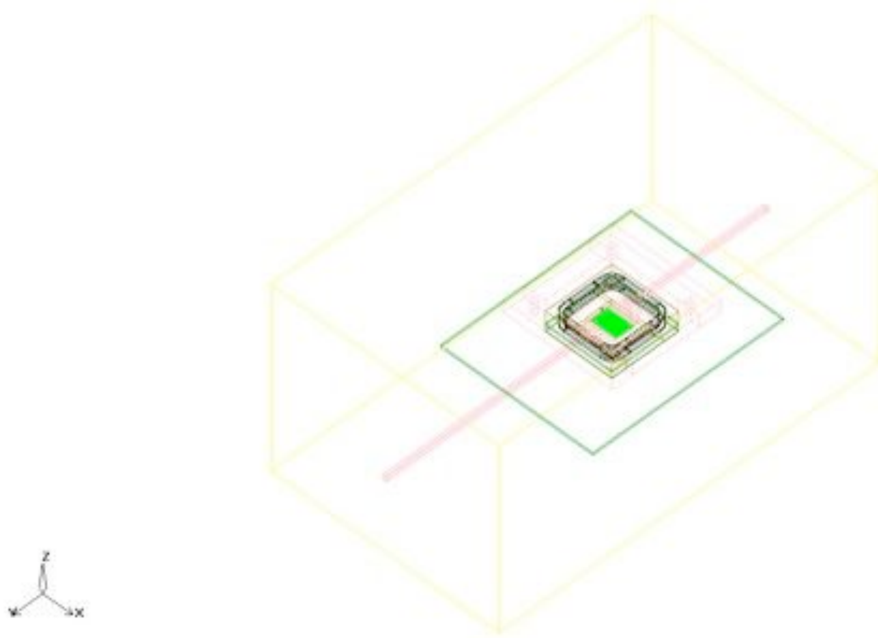

Figure 32: 3-D View of the Microgap Fluid Channel CFD Model.

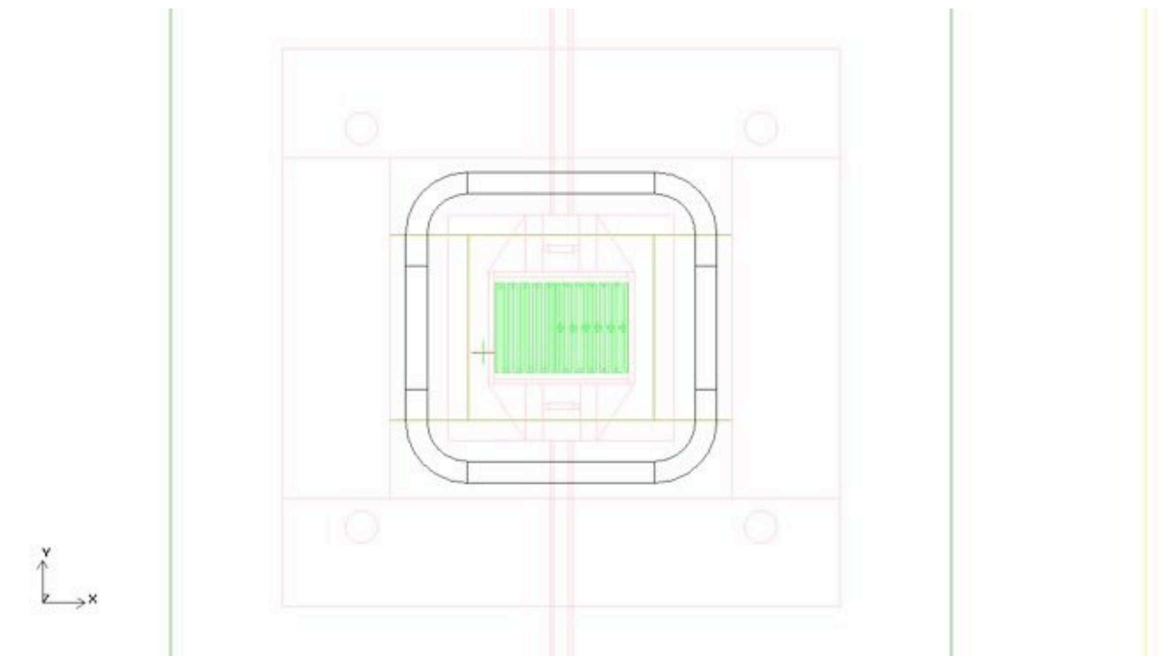

Figure 33: XY and YZ Views of the Microgap Fluid Channel CFD Model.

Note that the domain contains a sufficiently large volume of the surrounding ambient in the calculation such that the radiative and convective heat transfer between the chamber and the surrounding air are automatically calculated by the software and not prescribed or approximated. This makes it possible to precisely determine the heat losses from the test vehicle and to then assess - in all run cases - the fraction of power going into the coolant fluid inside the channels, i.e., the “conversion” rate. The die junction plane (where the power is dissipated) was modeled identically to represent the actual serpentine-like junction plane (Figure 21) in the actual thermal test chip. The half die and two quadrants are easily identified in Figure 34. This enables running uniform and non-uniform power dissipation in the numerical thermal-CFD model.

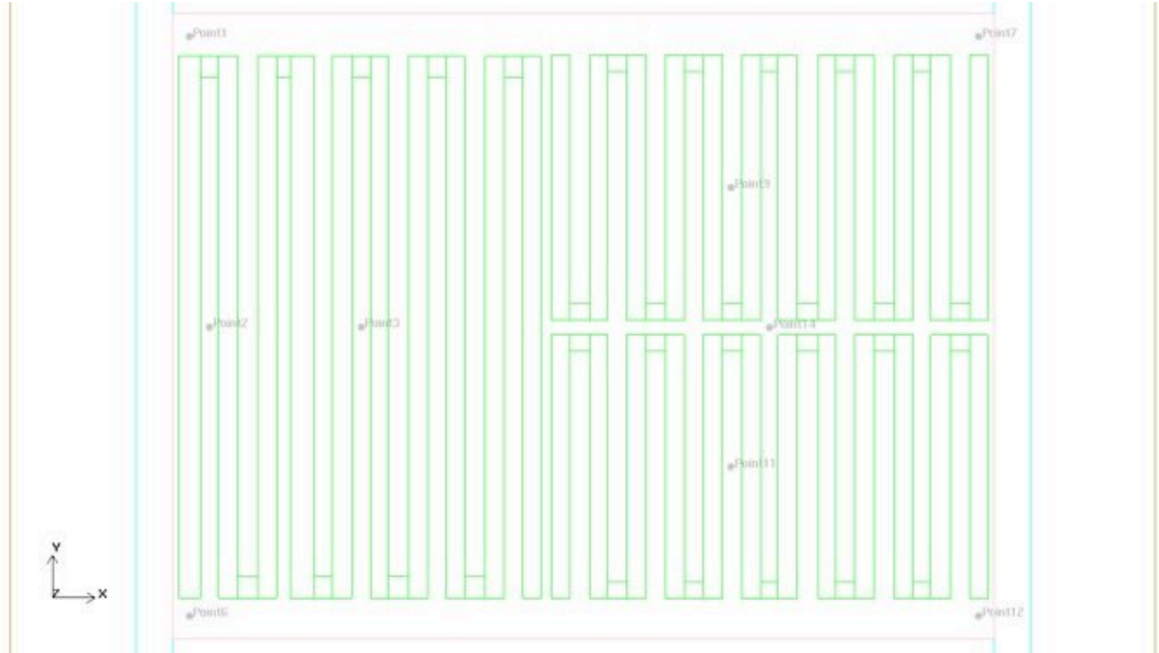

Figure 34: Model of the Junction Plane Showing the Emulated Serpentine-Type Heating Zones.

Chapter 6:

Single-Phase Data and Discussion

6.1 Basic relations

The thermal performance of a micro gap (micro channel) is characterized by the dimensionless Nusslet number (*Nu*) as given by

$$Nu = \frac{hD_h}{k} \tag{6.1}$$

Where k is the fluid thermal conductivity, D_h is the gap hydraulic diameter as given by

$$D_h = \frac{4.(cross\ section\ area)}{wetted\ perimeter} \tag{6.2}$$

and h is the micro gap heat transfer coefficient. The heat transfer coefficient is given by

$$h = \frac{q}{A\Delta T} \tag{6.3}$$

Where, ΔT is the temperature difference between the heated surface (die average temperature) and the fluid average inlet temperature, q is the heat transfer rate to the fluid (heat dissipated into fluid from the die surface) and A is the heated wall surface area. The heat transfer rate can be determined from an energy balance on the channel via the equation

$$q = \dot{m} C_p (T_{outlet} - T_{inlet}) \tag{6.4}$$

Where $\dot{m}$ is the fluid mass flow rate while T_{outlet} and T_{inlet} are the channel fluid outlet and inlet temperatures, respectively.

From the above equations, the heat transfer coefficient and Nusslet number can be calculated by the following expressions,

$$h = \frac{\dot{m} C_p (T_{outlet} - T_{inlet})}{A \Delta T} \tag{6.5}$$

$$Nu = \frac{\dot{m} C_p (T_{outlet} - T_{inlet})}{A \Delta T} \frac{D_h}{k} \tag{6.6}$$

6.2 Error Analysis

The test measurement error can be divided into bias errors and precision errors [54]. The bias error remains constant during the measurements under a fixed operating condition. The bias error can be estimated by calibration, concomitant methodology, inter-laboratory comparison and experience. When measurements are repeated under fixed operating conditions, the precision error is affected by the repeatability and resolution of the equipment used, the temporal and spatial variation of variables, the variations in measured variables, and variations in operating and environmental conditions in the measurement processes. Each measurement error would be combined with other errors in some manner, which increases the uncertainty of the measurement. A first-order estimate of the uncertainty in the measurement due to the individual errors can be computed by the root-sum-square method [55].

The uncertainty in the single-phase heat transfer coefficient, obtained from the channel energy balance equation above, is linear and is affected by the uncertainties in the measured quantities including the flow rate, the temperature of the wall (die sensors), the temperature of inlet and outlet, the stability of the data logger and power supply. It can be expressed mathematically as

$$\left(\frac{\delta h}{h}\right)^2 = \left(\frac{\delta \dot{m}}{\dot{m}}\right)^2 + \left(\frac{\delta q}{q}\right)^2 + \left(\frac{\delta \Delta T_{wall}}{\Delta T_{wall}}\right)^2 \qquad (6.7)$$

Where δh is the uncertainty of the heat transfer coefficient, $\delta \dot{m}$ is the error of flow rate via the flow meter, δq is error of input power via the power supply, $\delta \Delta T_{wall}$ is the measurement error of wall excess temperature. The flow meter's flow rate error is ± 1.5%. The error of the power supply is ± 2.5%. The maximum error in the wall excess temperature measurement is ± 0.25°C which causes maximum error of 1%. Thus, the possible maximum error in measuring the heat transfer coefficient is ±3%.

The uncertainty in the measured pressure drop across the gap (channel) is determined by the accuracy of the pressure transducer (± 0.25% Full Scale). However, uncertainty of the measured pressure drop is linearly dependent on the uncertainty in the measurement of flow. Therefore the resulting uncertainty of measuring pressure drop can be expressed as

$$\left(\frac{\delta \Delta P}{\Delta P}\right)^2 = \left(\frac{\delta \dot{m}}{\dot{m}}\right)^2 + \left(\frac{\delta \Delta P_t}{\Delta P_t}\right)^2 \tag{6.8}$$

Where ΔP is pressure drop and $\delta \Delta P$ is the uncertainty of pressure drop measurement and

$\delta \Delta P_t$ is the error of the pressure transducer. The error of pressure transducer is ± 0.25% FS. Therefore, the possible maximum error in the pressure drop measurement is 1.52%.

It should be noted that the above error analyses for both pressure drop and heat transfer coefficient measurements do not include the uncertainty and variation of HFE-7100 fluid properties, as there is no data (up to the author's knowledge) on the uncertainty of this fluid's properties in the literature.

6.3 Single Phase Results

6.3.1 Comparison of Experimental, CFD and Theoretical Correlations

To initiate operation of the test facility and validate the measurement procedures in preparation for the two-phase experiments, single phase hydrodynamic and heat transfer characteristics of the 100-micron channel, with HFE-7100 coolant, were studied. CFD model runs are compared to actual tests for various flow rates (1-9 ml/s), which correspond to an average velocity range of 0.7-6.5 m/s, and the results are depicted in Figures 35-36. Figure 35 shows the hydrodynamic performance comparisons i.e., pressure drop (ΔP) in the channel while Figure 36 shows the channel average heat transfer coefficient (h) comparisons. The figures also show the error (uncertainty) bar associated with testing data. Good accuracy is established from the CFD model as most of the pressure drop test results fall within 10% of the anticipated ΔP uncertainty error bar, while the heat transfer coefficient errors fall within 4% of the associated h uncertainty error bar. The measurement errors are larger than the predicted uncertainty and this is largely due to the uncertainty and variation of HFE-7100 fluid properties. M.S. El-Genk [56] studied pool boiling using HFE-7100 and

reported correlations errors of 10% larger than the measurement uncertainty of 3.7%. Similar fluid-properties based errors were reported by Kim et al, [19].

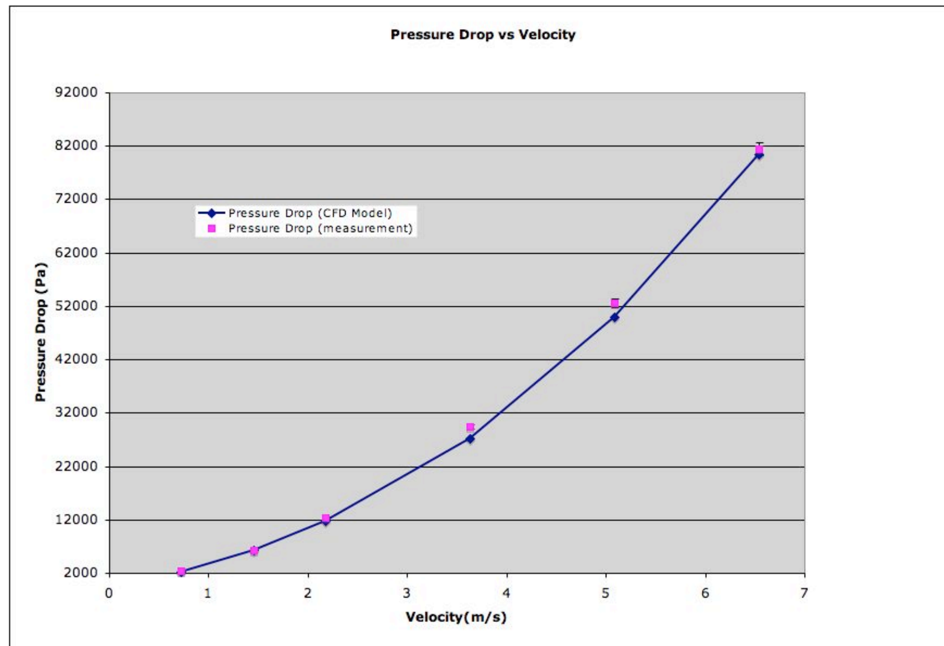

Figure 35: Effect of Fluid Velocity on Single-Phase Pressure Drop in a 100-micron Microgap Channel Flowing HFE-7100 (D_h = 200 micron).

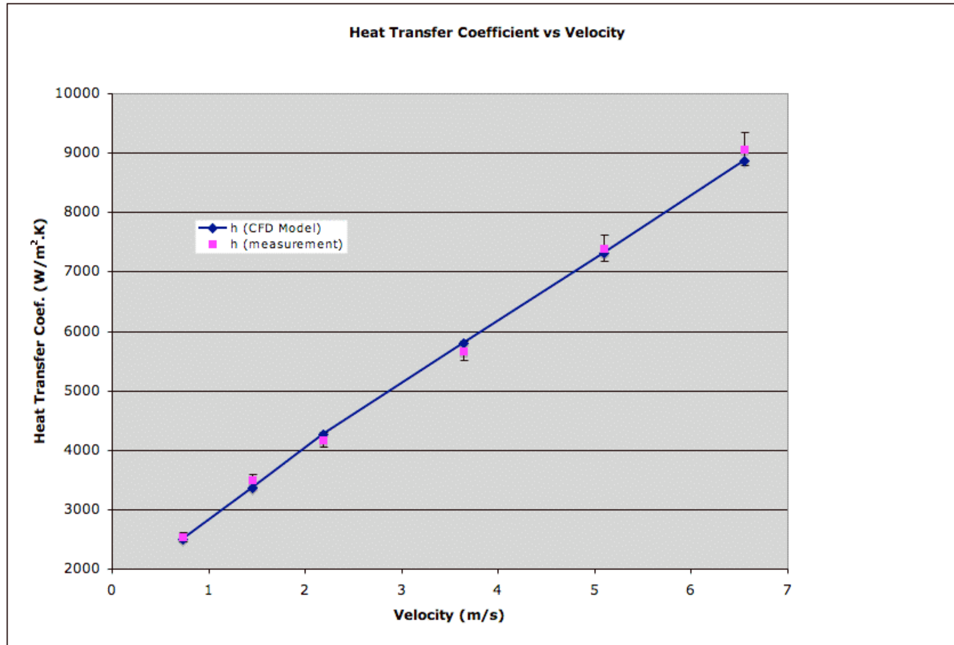

Figure 36: Effect of Fluid Velocity on Single-Phase Heat Transfer Coefficient in a 100-micron Microgap Channel Flowing HFE-7100 (D_h = 200 micron). P=10W, T_{in}=23C.

The single-phase hydrodynamic (pressure drop) and thermal (heat transfer coefficient) correlations discussed in Chapter 2, relate to an ideal channel of ideal boundary conditions, i.e., ideal channel geometries with the characteristics of the uniform flow, laminar-developing flow, uniform wall (planar) heating and negligible conjugate heat transfer effects. Figure 37 depicts the pressure drop as a function of velocity using the ideal channel correlation (in Chapter 2) and the corresponding actual test channel measurements and the CFD model results superimposed across the velocity range considered. Note, that the range of Reynolds number (Re) experienced was 380-3500 for the velocity range considered (0.7-6.5 m/s) where all the data was in the laminar

flow regime except for the last two data points (at 5 m/s and 6.5 m/s velocities or Re of 2700 and 3500, respectively) where the flow was in the laminar-to-turbulent transition regime. On the other hand, due to the very short channel considered (10.5 mm in length), the hydrodynamic entry length - approximately given by $0.05.\mathrm{Re}.D_h$ [25] - was higher than the channel length across the velocity range considered, except for the very low velocities of 0.7 m/s and 1.5 m/s, for which, the channel experienced a combination of developing and fully developed flow. The thermal entry length given by $0.05.\mathrm{Re}.\mathrm{Pr}\,D_h$ [25] was, however, higher than the channel length across the full velocity range considered and thus the thermal transport in the channel was always in the developing flow condition.

While CFD results do not agree well with the correlations, they however can simulate these non-idealities and show good agreement with actual measurements. Using the ideal channel correlation to predict the actual non-ideal channel measured pressure drops, provides a similar trend with fluid velocity but yields an average error of 24% with the largest error at the low velocities. The CFD model, however, provides much better agreement with measurements whereby the average error is reduced to 5%.

Figure 38 depicts the heat transfer coefficient as a function of flow rate using the ideal channel correlation and the corresponding actual test channel measured heat transfer coefficient's, superimposed across the velocity range considered. Very similar conclusions, to those of the hydrodynamic ones, can be drawn for the heat transfer

results. The average error of using the ideal geometry channel heat transfer coefficient correlation to predict the actual complex channel heat transfer coefficient is 7% and the error is largest at the low velocities. The CFD model provides better agreement with measurements whereby the average error is reduced to 4%.

These findings help make two main points; establishing credibility and accuracy of the CFD model of the non-ideal (actual complex geometry) channel and determining the error margin associated with single-phase correlation. The later finding will be very important in the later analysis of two-phase correlation accuracy in later chapters.

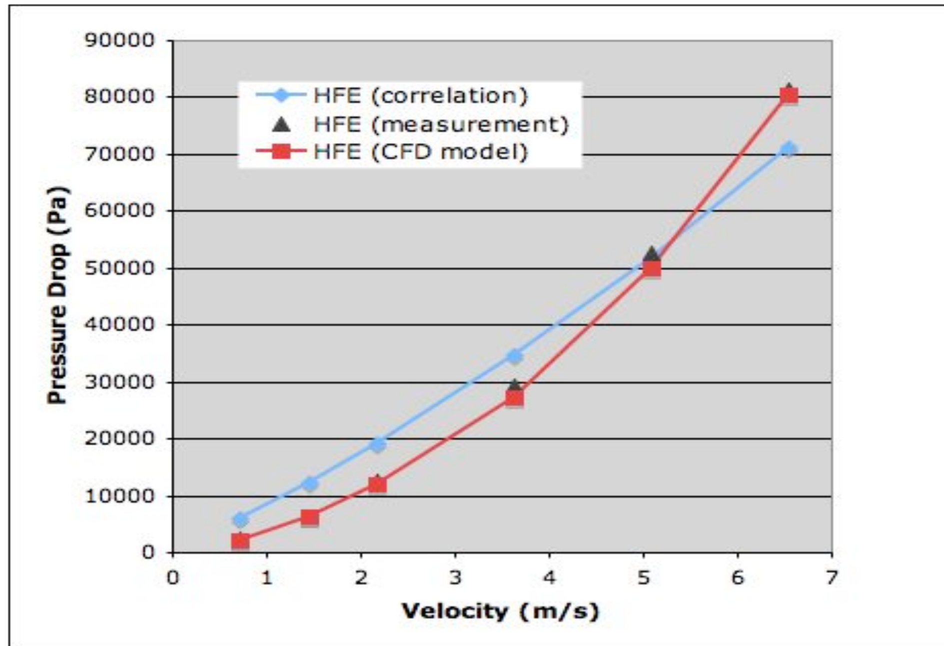

Figure 37: Single-Phase Pressure Drop vs. Velocity for HFE-7100 in a 100-micron Microgap Channel (D_h=200 micron).

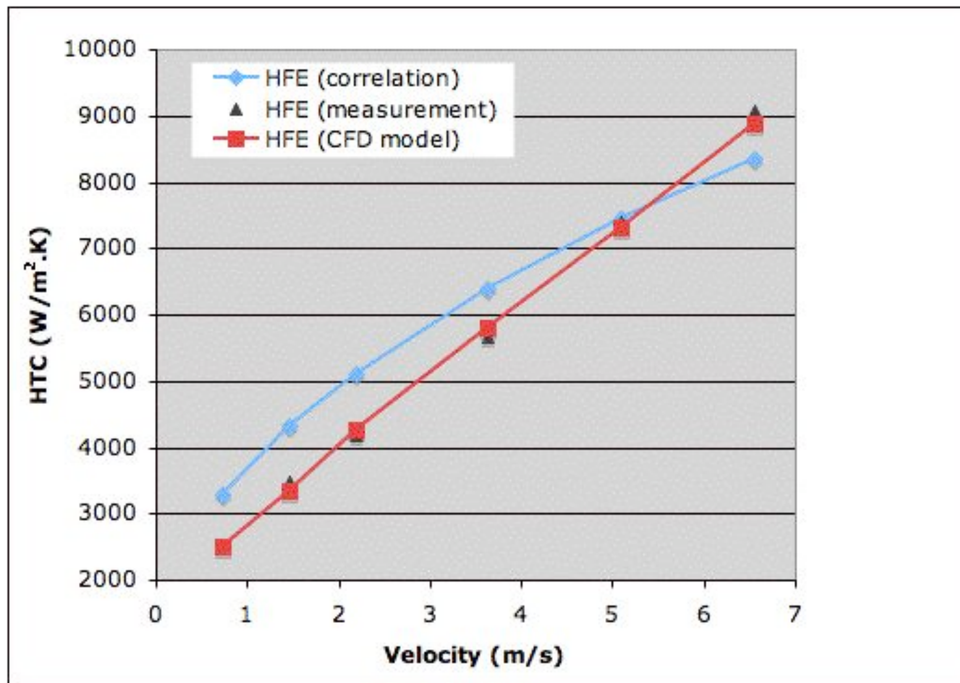

Figure 38: Single-Phase Heat Transfer Coefficient vs. Velocity for HFE-7100 in a 100-micron Microgap Channel (D_h=200 micron). P=10W, T_{in}=23C.

6.3.2 Raw temperature data and Comparison to CFD

The measured temperatures obtained from the sensors embedded in the die surface (wall), due to the nearly-uniform heating across the entire junction plane of die and with HFE-7100 flowing and with 1ml/s and 9 ml/s, respectively, is shown in Table 5. The 1 ml/s and 9 ml/s flow rates correspond to Reynolds numbers of Re=380 and Re=3420, and to velocities of 0.7 m/s and 6.5 m/s, respectively. CFD model results are shown along with the test data. The percentage errors, relative to fluid inlet temperature T_{in}=23C, were calculated and tabulated as well. Good agreement is

established between test and CFD model results as shown in Table 5 with respect to individual sensor temperatures and wall average, minimum and maximum temperatures with maximum error at ~ 5%.

Flow Rate	1 ml/s			9 ml/s		
Sensor	CFD	test	error(%)	CFD	test	error (%)
101	44.8	43.8	4.8	30.9	30.6	3.9
102	45.8	45.9	0.4	31.4	31.2	2.4
103	44.6	44.1	2.4	30.9	31.1	2.5
104	45.6	45.2	1.8	31.5	31.3	2.4
105	43.2	43.7	2.4	29.3	29.1	3.3
106	41.7	41.5	1.1	28.9	28.7	3.5
107	45.5	45.4	0.4	31.4	31.3	1.2
108	43.6	43.1	2.5	29.6	29.5	1.5
109	42.1	41.7	2.1	29.3	29	5
Average	44.1	43.8	1.4	30.4	30.2	2.8
Minimum	41.7	41.5	1.1	28.9	28.7	3.5
Maximum	45.8	45.9	0.4	31.5	31.3	2.4

Table 5: Sensor Temperatures for the Uniformly Heated 100-micron Microgap Channel with the Flow of HFE-7100, T_{in}=23°C, q''=7W/cm^2.

The measured temperatures obtained from the sensors embedded in the die surface (wall), due to the half-die and quadrant-die non-uniform heating across the entire junction plane of die and with HFE-7100 flowing and with 1ml/s and 9 ml/s, respectively, are shown in Tables 6 and 7. CFD model results are shown along the test data. The percentage errors, relative to fluid inlet temperature T_{in}=23C, were calculated and tabulated as well. As with the uniform heating case above, good agreement is established between testing and CFD model data as shown in Tables 6

and 7 with respect to individual sensor temperatures and wall average, minimum and maximum temperatures with maximum error at ~ 10%.

Flow Rate	1 ml/s			9 ml/s		
Sensor	CFD	test	error(%)	CFD	test	error (%)
101	52.6	51.9	2.4	36.2	35.8	3.1
102	40.9	40.1	4.7	27.8	27.5	6.7
103	39.9	39.1	5	27.5	27.7	4.3
104	52	51.8	0.7	36.1	35.8	2.3
105	37.3	36.8	3.6	25.8	26	6.7
106	36.1	36.3	1.5	25.5	25.7	7.4
107	39.8	39.6	1.2	27.3	27.5	4.4
108	50	50.1	0.4	33.5	33.1	4
109	48.2	49.2	3.8	33	32.8	2
Average	44.1	43.9	1	30.3	30.2	1.4
Minimum	36.1	36.3	1.5	25.5	25.7	7.4
Maximum	52.6	51.9	2.4	36.2	35.8	3.1

Table 6: Sensor Temperatures for the Half-Die Heated 100-micron Microgap Channel with the Flow of HFE-7100, T_{in}=23°C, q″=7W/cm^2.

Flow Rate	1 ml/s			9 ml/s		
Sensor	CFD	test	error(%)	CFD	test	error (%)
101	37.9	37.3	4.2	26.3	26.1	6.5
102	55.3	56.4	3.3	39	38.4	3.9
103	43	42.1	4.7	29.5	29.8	4.4
104	39.8	38.9	5.7	27.5	27.7	4.3
105	54.5	56.1	4.8	36.8	36.2	4.5
106	40	39.5	3	27.4	27.2	4.8
107	50.1	50.2	0.4	34.9	35.3	3.3
108	38.6	37.8	5.4	26.5	26.2	9.4
109	35.6	35.1	4.1	25.4	25.2	9.1
Average	43.9	43.7	1	30.4	30.2	2.8
Minimum	35.6	35.1	4.1	25.4	25.2	9.1
Maximum	55.3	56.4	3.3	39	38.4	3.9

Table 7: Sensor Temperatures for the Quadrant-Die Heated 100-micron Microgap Channel with the Flow of HFE-7100, T_{in}=23°C, q″=7W/cm^2.

The die surface (wall) sensor average excess temperature (temperature rise above the 23C inlet) is shown in Figure 39 for the test and CFD model results for 100-micron channel and uniform heating across a range of 1-9 ml/s flow rates (0.7 to 6.5 ml/s velocity). It is worth mentioning that the discrepancy in sensor excess temperature between experimental and CFD simulation results are 2% and 4%, respectively.

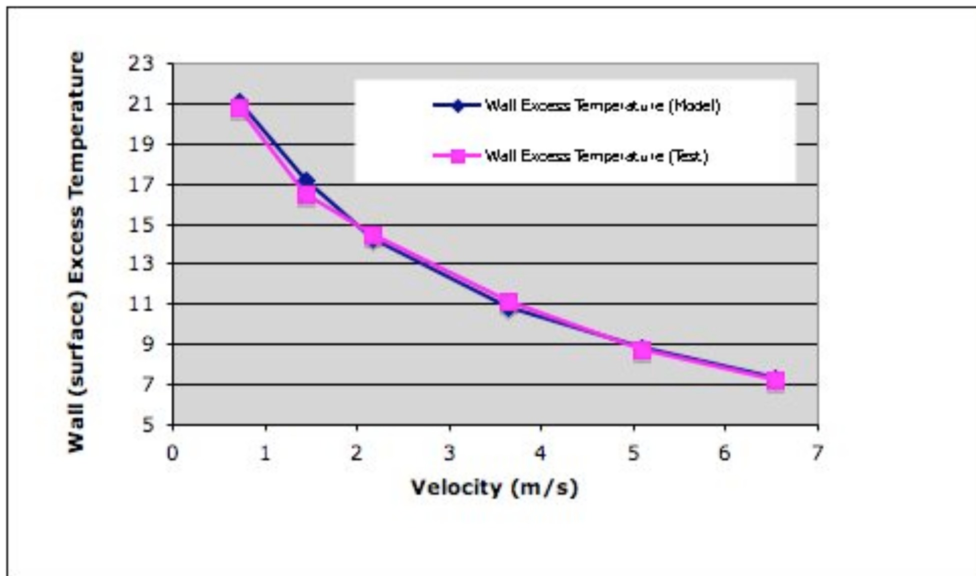

Figure 39: Die Average Sensor Excess Temperature Test Data and CFD Simulation vs. Velocity, HFE-7100 flowing in a 100-micron Microgap Channel and Uniform Heating q''=7W/cm^2.

The accuracy of die sensor temperatures, embedded at the junction plane, compared to the actual wall temperatures (the surface plane), is performed. Tables 8, 9 and 10 show the nine sensor temperatures (101-109) along with their average, minimum and

maximum values at both the junction plane and at the wall (surface plane) for variable flow rates (1-9 ml/s). The sensor average, minimum and maximum temperatures are shown to be close to their footprint locations at the surface (wall) plane with a maximum difference percentage of <2%. While the temperatures at the junction plane are not very different from their footprints at the surface plane, better results can be obtained by using the CFD-derived surface temperatures and this will become more important at the higher heat fluxes of two-phase flow.

Flow rate (ml/s)	1	2	3	5	7	9
101	44.86	40.86	37.90	34.48	32.41	30.93
102	45.81	41.64	38.58	35.05	32.96	31.44
103	44.66	40.90	37.91	34.55	32.44	30.95
104	45.66	41.66	38.63	35.16	33.05	31.53
105	43.24	39.03	36.10	32.73	30.74	29.33
106	41.67	38.07	35.32	32.21	30.24	28.90
107	45.48	41.49	38.46	34.99	32.89	31.38
108	43.59	39.37	36.43	33.03	31.01	29.58
109	42.07	38.44	35.68	32.54	30.54	29.17
Average	44.12	40.16	37.22	33.86	31.81	30.36
Surface Average	44.55	40.57	37.57	34.13	32.04	30.54
Difference Percentage (%)	1	1	0.9	0.8	0.7	0.6
Minimum	41.67	38.07	35.32	32.21	30.24	28.90
Surface Minimum	41.57	37.89	35.11	31.94	29.94	28.59
Difference Percentage(%)	-0.2	-0.5	-0.6	-0.8	-1	-1.1
Maximum	45.81	41.66	38.63	35.16	33.05	31.53
Surface Maximum	45.95	41.82	38.71	35.15	33	31.44
Difference Percentage(%)	0.3	0.4	0.2	0	-0.2	-0.3

Table 8: Sensor Temperatures vs. Flow Rates and Junction vs. Surface (Wall) Temperatures for 100-micron Channel and Uniform Heating with the flow of HFE-7100, T_{in}=23°C, q″=7W/cm^2.

Flow rate (ml/s)	1	2	3	5	7	9
101	52.60	48.18	44.76	40.72	38.14	36.21
102	40.89	36.96	34.12	30.94	29.13	27.85
103	39.92	36.36	33.58	30.56	28.73	27.50
104	52.05	47.76	44.40	40.47	37.99	36.13
105	37.26	33.53	31.00	28.25	26.75	25.76
106	36.09	32.86	30.48	27.94	26.46	25.53
107	39.81	36.09	33.32	30.27	28.51	27.29
108	50.05	45.33	41.95	37.92	35.40	33.54
109	48.20	44.19	41.02	37.29	34.78	32.99
Average	44.09	40.14	37.18	33.82	31.77	30.31
Surface Average	44.51	40.53	37.52	34.09	32	30.51
Difference Percentage (%)	0.9	1	0.9	0.8	0.7	0.6
Minimum	36.09	32.86	30.48	27.94	26.46	25.53
Surface Minimum	35.97	32.7	30.31	27.76	26.29	25.37
Difference Percentage(%)	-0.3	-0.5	-0.6	-0.6	-0.7	-0.6
Maximum	52.60	48.18	44.76	40.72	38.14	36.21
Surface Maximum	52.59	48.05	44.6	40.51	37.95	36.01
Difference Percentage(%)	0	-0.3	-0.4	-0.5	-0.5	-0.6

Table 9: Sensor Temperatures vs. Flow Rates and Junction vs. Surface (Wall) Temperatures for 100-micron Channel and Half-Die Heating with the flow of HFE-7100, T_{in}=23°C, q″=7W/cm^2.

Flow Rate (ml/s)	1	2	3	5	7	9
101	37.87	34.36	31.81	28.97	27.37	26.29
102	55.34	51.00	47.62	43.53	40.97	39.01
103	43.02	39.36	36.40	33.02	30.94	29.47
104	39.82	36.21	33.51	30.46	28.70	27.48
105	54.54	49.75	46.18	41.78	38.91	36.76
106	39.98	36.46	33.73	30.62	28.70	27.40
107	50.10	46.06	42.84	39.03	36.65	34.87
108	38.66	34.90	32.29	29.34	27.68	26.55
109	35.60	32.48	30.19	27.69	26.26	25.36
Average	43.88	40.07	37.17	33.83	31.80	30.35
Surface Average	44.31	40.47	37.51	34.09	32.02	30.53
Difference Percentage (%)	1	1	0.9	0.8	0.7	0.6
Minimum	35.60	32.48	30.19	27.69	26.26	25.36
Surface Minimum	35.47	32.32	30.01	27.51	26.1	25.2
Difference Percentage(%)	-0.4	-0.5	-0.6	-0.6	-0.6	-0.6
Maximum	55.34	51.00	47.62	43.53	40.97	39.01
Surface Maximum	56.44	51.75	48.18	43.82	41.04	38.9
Difference Percentage(%)	1.9	1.5	1.2	0.7	0.2	-0.3

Table 10: Sensor Temperatures vs. Flow Rates and Junction vs. Surface (Wall) Temperatures for 100-micron Channel and Quadrant-Die Heating with the flow of HFE-7100, T_{in}=23°C, q''=7W/cm^2.

6.3.3 Conjugate effects and conduction spreading in advanced microprocessors

The theoretical relations and empirical correlations for single phase heat transfer available in the literature neglect the impact of conjugate heat transfer associated with conduction spreading within the thermally conductive blocks of semiconductor die

chips. These theoretical formulations are based on uniform heat flux or uniform temperature boundary conditions on the surface interacting with the cooling fluid. Similarly, researchers in the field, when conducting single-phase heat transfer experiments, strive to produce either a fixed flux or fixed temperature wetted surface. Thus, nearly all the available formulations for predicting the convective heat transfer coefficient are based on these ideal boundary conditions. Due to the generally non-uniform heating in an operating chip, and despite the high thermal conductivity of silicon, conjugate effects must be included in any effort to achieve a precise temperature prediction for a convectively cooled chip. Consequently, in the current study, a detailed thermofluid numerical model of the test apparatus and the heated chip was created and validated by a comparison of the predicted temperatures at the locations of nine distinct sensors embedded in the "junction" plane of the chip.

The importance of resolving the spatial distribution of heat flux (the heat flux map) at the wall surface and resultant distribution of the surface heat transfer coefficients for the 800-micron thick chip with an average conductivity of 120 W/mK, can not be overstated. Figures 40, 41 and 42 below, graphically illustrate this conduction spreading effect on the three heating patterns studied, i.e., uniform heating, half die heating and quadrant die heating, respectively.

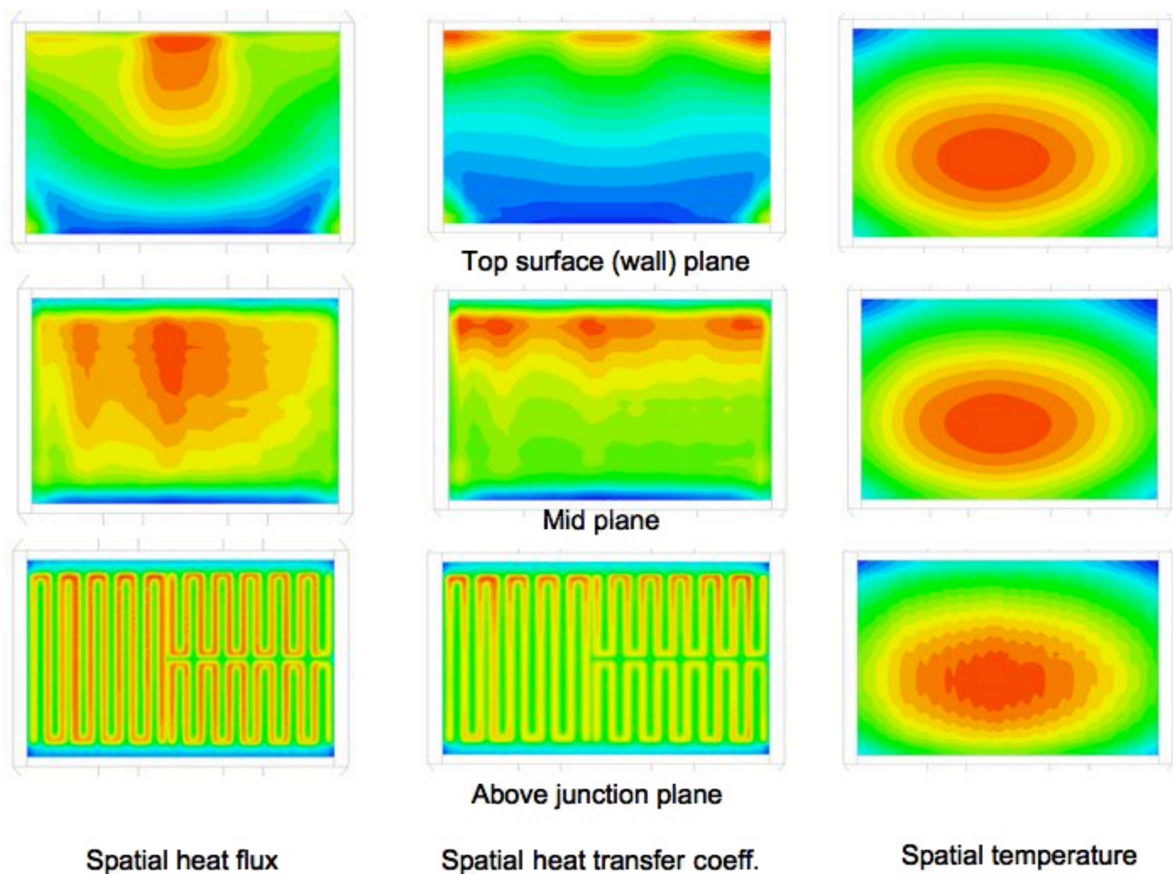

Figure 40: Conduction Spreading Conjugate Effect on Wall Spatial Heat Flux and Heat Transfer Coefficient for Uniformly Heated 100-micron Channel with the Flow of HFE-7100, T_{in}=23°C, q''=7W/cm^2.

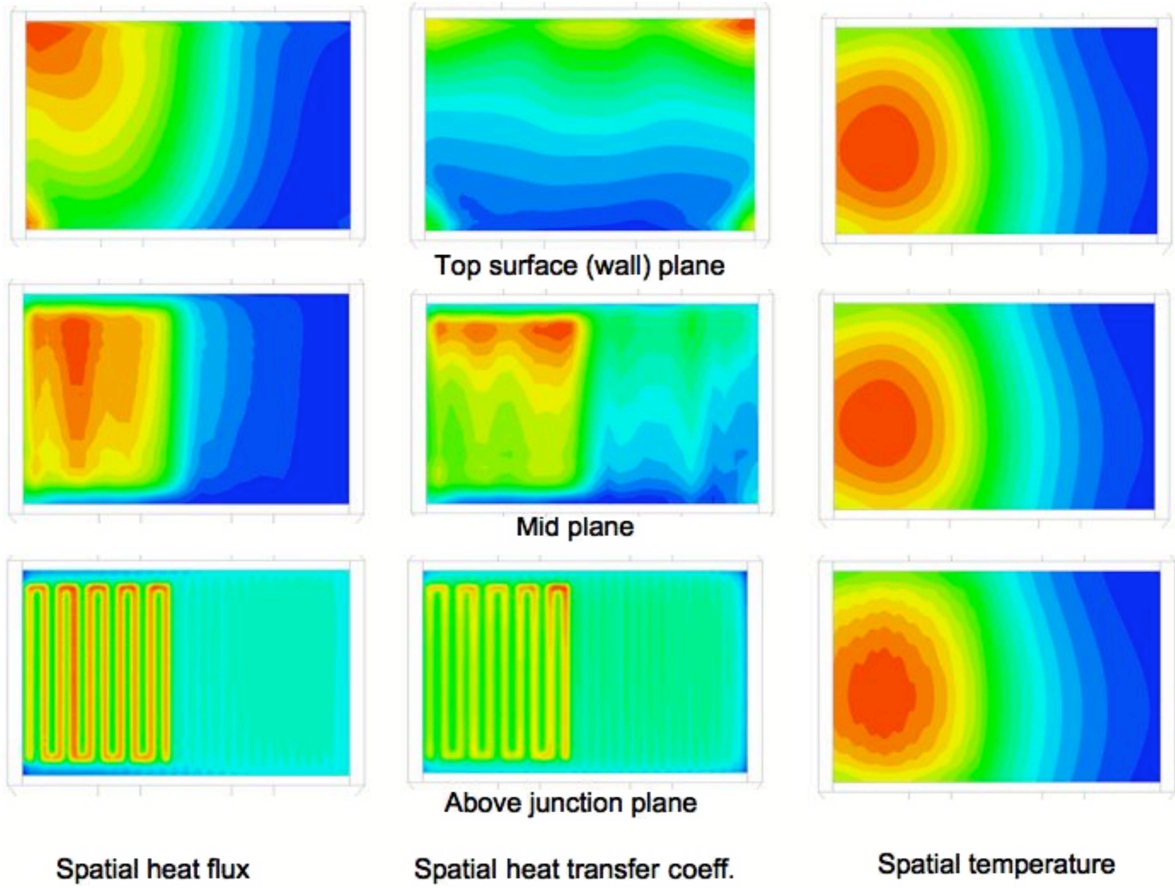

Figure 41: Conduction Spreading Conjugate Effect on Wall Spatial Heat Flux and Heat Transfer Coefficient for Half-Die Heated 100-micron Channel with the Flow of HFE-7100, T_{in}=23°C, q″=7W/cm^2.

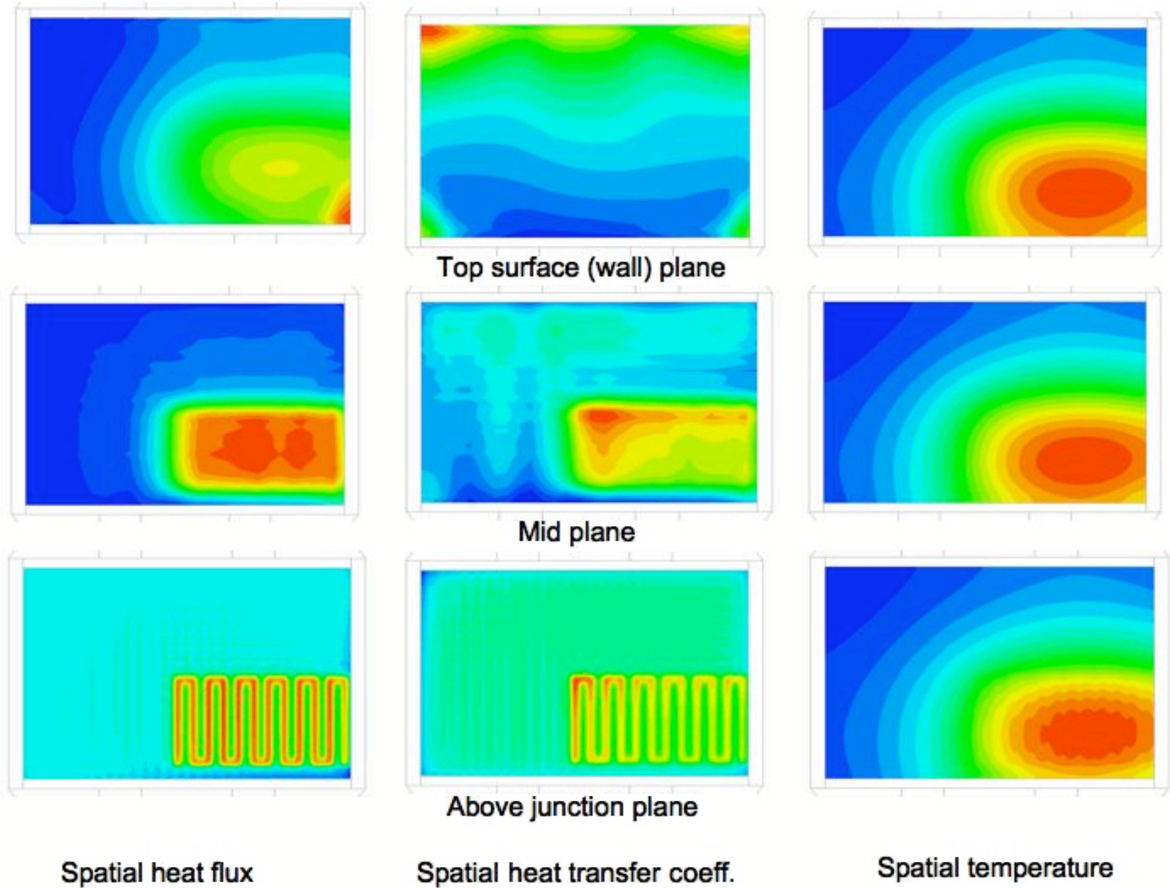

Figure 42: Conduction Spreading Conjugate Effect on Wall Spatial Heat Flux and Heat Transfer Coefficient for Quadrant-Die Heated 100-micron Channel with the Flow of HFE-7100, T_{in}=23°C, q''=7W/cm^2.

Figures 40-42 show the spatial heat flux distribution and spatial temperature distribution on three different planes that slice through the silicon chip: at the junction plane (where the heat is applied,) at mid plane and at the top die surface (wetted wall).

The figures reference the results three different heating patterns of the 100-micron channel flowing HFE-7100 with T_{in}=23°C and q''=7W/cm^2.

While the spatial temperature plots do not change much in pattern, it is clear that the heat flux distribution on the wetted surface changes dramatically across the thickness of the silicon die from the junction (bottom) plane to the top surface.

Most importantly, it is found that while the silicon conduction spreading does smooth out the serpentine pattern applied to the full junction plane of the chip, it does not yield a uniform heat flux wetted surface. Rather, the combined conduction-convection effects on this chip with an average heat flux of 6.5W/cm^2 result in highly non-uniform heat flux at the wetted wall, with a peak heat flux reaching 10W/cm^2 at the axial centerline near the inlet to the microgap channel and steep axial and lateral gradients that yield a flux of 2.5W/cm^2 at the channel outlet along the centerline and 4W/cm^2 at the lateral edges. This highly non-isoflux condition, combined with the non-isothermal condition, lead to a complex temperature-flux distribution on the wetted surface and clearly explains why available uniform heat flux correlations failed to predict accurately the spatial wall heat transfer coefficient.

As with uniform heating, non-uniform heating represented by the half-die heating and quadrant-die heating shown in Figures 41 and 42, the conjugate effect (die silicon block conduction spreading) has a similar effect in changing the resultant surface heat flux and heat transfer coefficient. However, due to the concentrated heat and thus heat flux at the junction plane with these non-uniform heating types, the resultant surface

heat fluxes have a somewhat similar distribution to those at the junction plane. This is clearly shown in Figures 41 and 42 where the highest heat flux is seen at the same locations as in the junction plane, i.e., left half of the die with half-die heating and bottom left quarter of the die with quadrant-die heating.

The availability of the full CFD model makes it possible to refine the calculation of the heat lost from the junction plane to the larger package and housing of the test chamber. Consequently, for the evaluation of the efficacy of the apparatus and for determination of the average heat transfer coefficient, a conjugate thermal analysis was performed to determine the percentage of heat going into the channel fluid, i.e., the heat conversion rate versus the heat conducted into the chip substrate and the surrounding structure. The conversion rate was used in the calculations of the average heat transfer coefficients shown in Figures 36 and 38. The resulting conversion rates are shown in Figure 43 for the fluid inlet velocity range considered. It is clearly shown, that the conversion rate, i.e., heat dissipated across the wetted surface and into the flowing liquid, increases with the fluid inlet velocity, rising from 7.6W to 9.4W of total chip power (10W) as the fluid inlet velocity increases from 0.7 m/s to 6.5m/s.

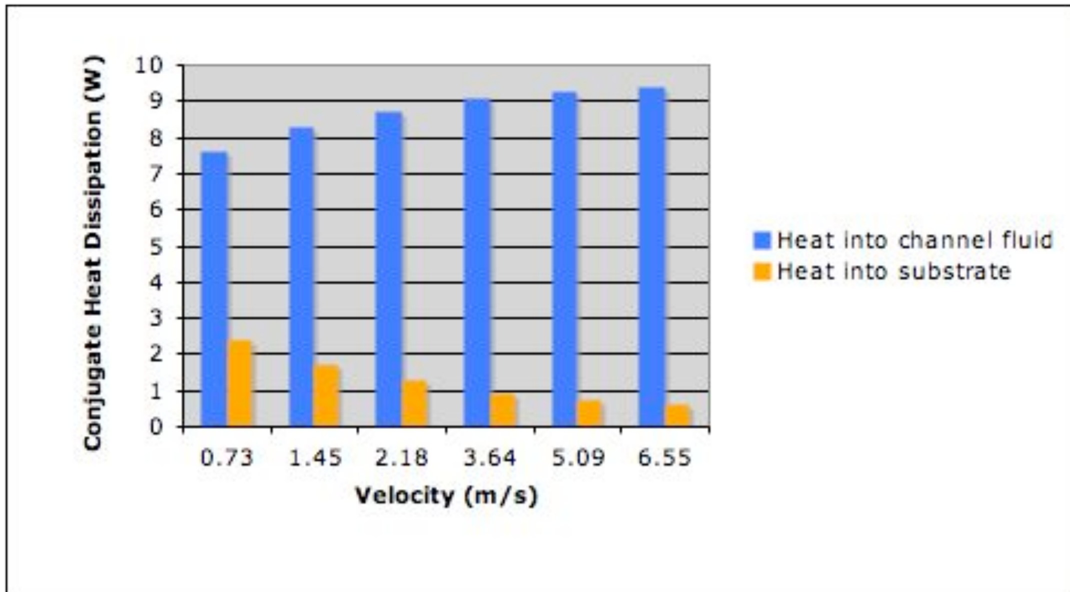

Figure 43: Single-Phase Conjugate Heat Transfer Conversion Rate vs. Fluid Inlet Velocity for the 100-micron Microgap Channel. P=10W, T_{in}=23C.

6.3.4 Temperature Distribution – Uniform Heating

The temperature distribution, obtained from the validated CFD model, at the die surface (wall), due to the nearly-uniform heating across the entire junction plane of the die and with HFE-7100 flowing at velocities of 0.7 m/s and 6.5 m/s (1ml/s and 9 ml/s), respectively, is plotted in Figure 44**.** It is clearly observed, that due to the non-ideal characteristic of the channel, including developing flow heat transfer coefficients and conduction in the silicon chip, as well as the sensible temperature rise in the coolant and despite the nearly-uniform heating in the die junction plane, the temperature distribution is decidedly non-uniform, with a clear main temperature gradient along the axial (flow) direction and a minor temperature variation along the lateral axis. The

temperature profile, with lateral and axial variations of nearly 4.5C, appears to display an almost axisymmetric distribution with the peak temperature located near the centerline of the channel but shifted somewhat downstream from the middle of the die.

Velocity Field:

The fluid flow velocity vectors for 0.7m/s and 6.5m/s, respectively, obtained from the CFD simulation of the microgap channel, are shown in Figure 45, for a plane cutting across the mid-height of the microgap channel. For the lower velocity, the fluid is seen to enter the channel at a nominal velocity of 0.7m/s through the inlet, and to diverge into the channel, impinging on the wetted surface of the die with an oblique – rather than a purely axial velocity of 0.4 m/s. After washing across the surface of the chip, the fluid converges towards the outlet and then exits the test chamber. Interestingly it is seen that some fluid bypasses the center of the chip and flows along the sidewalls through the 0.5 mm gap between the chip and the left and right sidewalls, respectively. This produces variation of fluid velocity across the channel width as the velocity decreases about three folds from the center toward the left and right sides. In an actual chip package, this gap serves as a "keep-out" zone to protect the chip against possible mechanical damage (scratches) and/or electrical shorting but this essential feature of an actual package prevents the fluid from distributing uniformly across the heated surface. The velocity field for the higher 9m/s velocity displays many of the same characteristics as the low velocity configuration but the higher momentum associated with the 6.5m/s inlet velocity results in a jet-like flow down the axial centerline of the

chip, with velocities approaching 5m/s, which is dissipated in the broader flow field well before the outlet.

Pressure Fields:

The pressure distributions through and across the microgap channel are shown in Figure 46 for the two noted velocities, 0.7m/s and 6.5m/s, respectively. Despite the small non-uniformity in the velocity profile across the chip, the pressure distribution is nearly laterally uniform and only varies modestly in the axial direction in the microgap channel itself. Most of the inlet-to-outlet pressure drop, i.e., 2.6kPa for the 0.7m/s and 77kPa for the 6.5m/s fluid velocities, respectively, occurs in the inlet and outlet zones due to the divergence and convergence of the flow. In addition, the flow through two, ninety-degree angles at inlet and outlet, can introduce a significant manifold pressure drop.

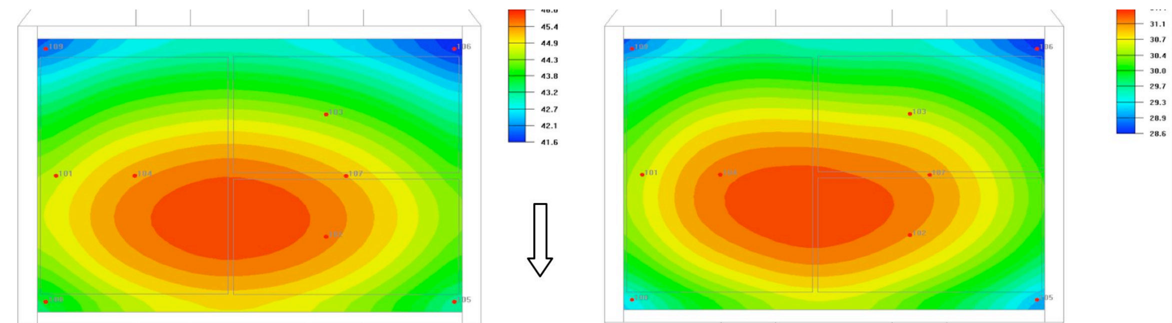

(a) 0.7 m/s (b) 6.5 m/s

Figure 44: Chip Surface (Wall) Temperature Distribution of Uniformly Heated 100-micron Microgap Channel - (a) 0.7m/s (left), (b) 6.5m/s (right), Tin =23C.

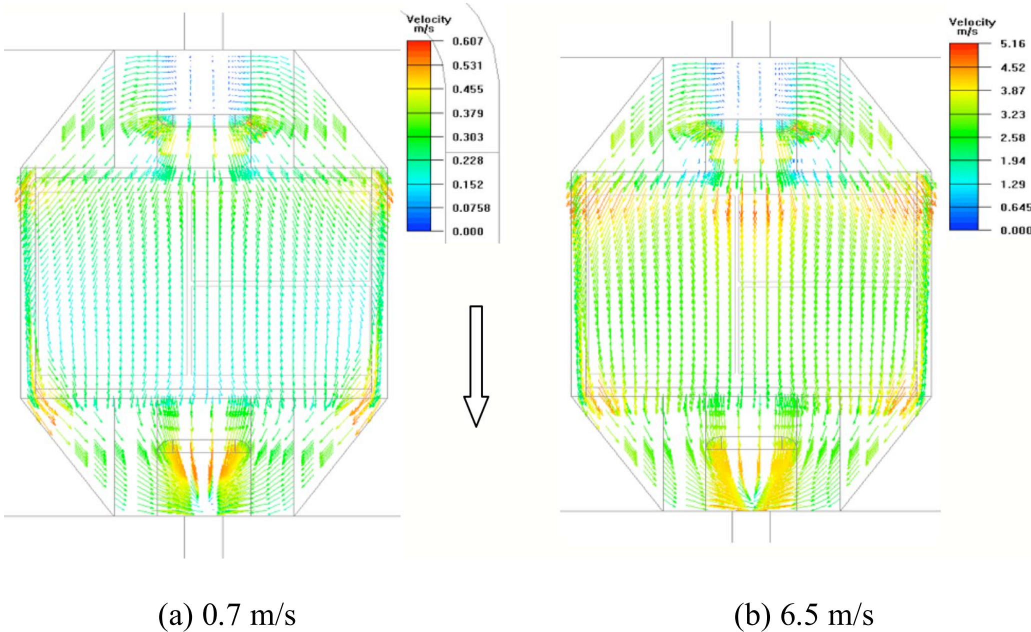

(a) 0.7 m/s (b) 6.5 m/s

Figure 45: Mid-Height Fluid Velocity Vectors Distribution for a 100-micron Uniformly Heated Microgap Channel - (a) 0.7m/s (left), (b) 6.5m/s (right).

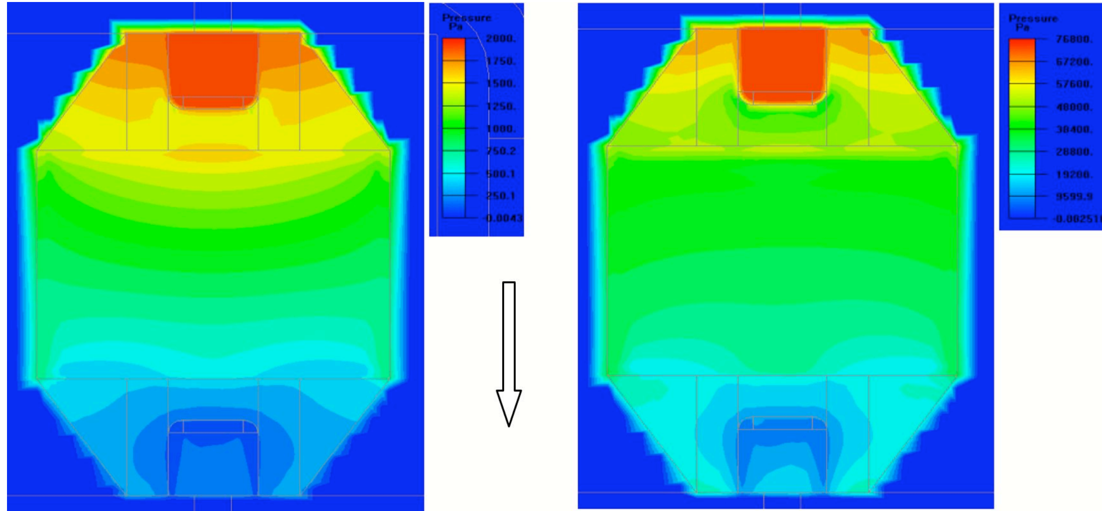

(a) 0.7 m/s (b) 6.5 m/s

Figure 46: Mid-Height Pressure Distribution for a 100-micron Uniformly Heated Microgap Channel - (a) 0.7m/s (left), (b) 6.5m/s (right).

6.3.5 Temperature Distribution – Half-Die and Quadrant-Die Heating

The temperature distribution obtained from the simulations performed with the validated CFD model at the channel wall, due to the non-uniform heating of the die, is plotted in Figures 47 and 48, for the half-die heating and quadrant-die heating, respectively, and a fluid inlet temperature of 23°C. It is clearly shown that the temperature distribution is highly non-uniform. The maximum wall temperature is located around the middle of the heated half-die and heated quadrant-die for both non-uniform heating cases, respectively. Larger temperature gradient across the die wall is seen with the non-uniformity cases compared to the earlier uniformly heated case. A temperature gradient of 16C is seen with the half-die heated channel and inlet fluid

velocity of 0.7 m/s with a maximum temperature of 52.6C and a minimum temperature of 36C. The die wall gradient increases with the quadrant die heating to 20C with a maximum temperature of 56.4C and a minimum temperature of 35.5C.

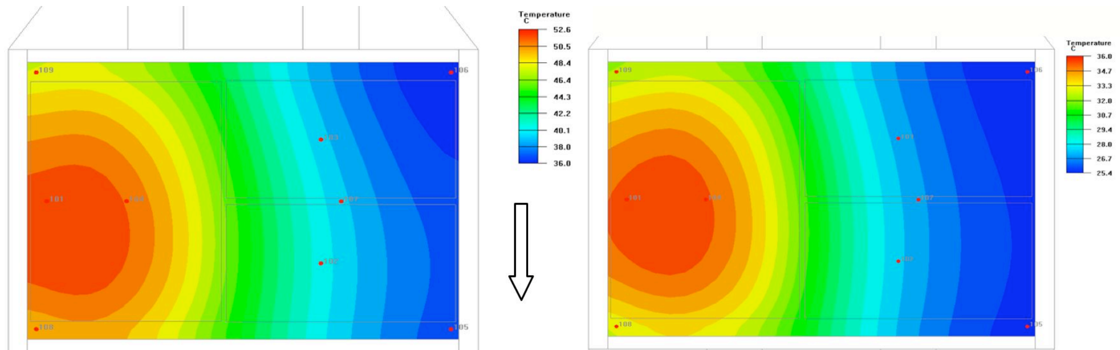

(a) 0.7 m/s (b) 6.5 m/s

Figure 47: Chip Surface (Wall) Temperature Distribution of Half-Die Heated 100-micron Microgap Channel - (a) 0.7m/s (left), (b) 6.5m/s (right), Tin=23C.

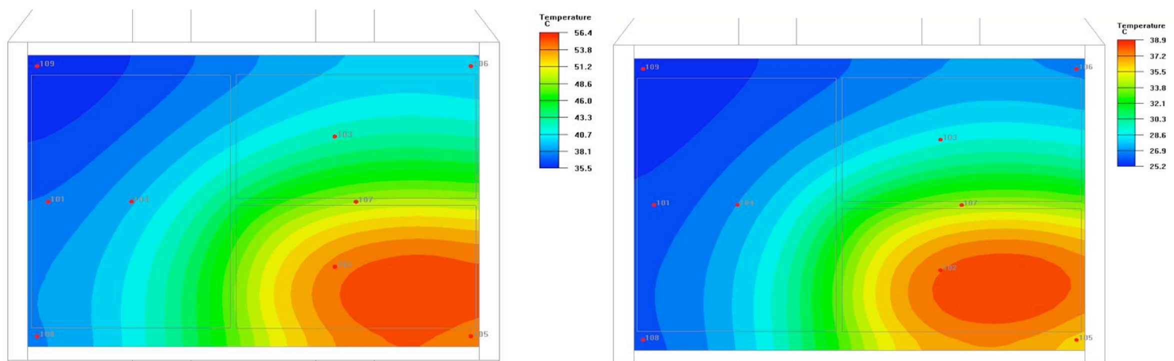

(a) 0.7 m/s (b) 6.5 m/s

Figure 48: Chip Surface (Wall) Temperature Distribution of Quadrant-Die Heated 100-micron Microgap Channel - (a) 0.7m/s (left), (b) 6.5m/s (right), Tin=23C.

6.3.6 Inversely Determined Heat Transfer Coefficients

The availability of the detailed thermo-fluid model of the resistance-heated chip developed in this study also makes it possible to determine the local heat transfer coefficient, on a cell-by-cell basis, across the die surface based on knowing the cell temperature and heat flux and the reference temperature, which was assigned to be the inlet fluid temperature. Applying Newton's law of cooling on a cell-by-cell basis, the spatial variations of the heat transfer coefficient across the die surface are shown in Figure 49 for 0.7m/s and 6.5m/s inlet fluid velocities, respectively. The heat transfer coefficient distribution for the 0.7m/s inlet fluid velocity, with Re of 380 is nearly uniform in the lateral direction but varies by a factor of nearly 3.5 in the axial direction, from a high of 2600 W/m^2K at the upstream edge of the chip to 937 W/m^2K at the downstream edge of the chip. The heat transfer coefficient distribution for the 6.5 m/s inlet fluid velocity case, with Re of 3420, is highly non-uniform laterally and axially, varying from a high of 10200 W/m^2K at the upstream edge of the chip to 4223 W/m^2K at the downstream edge of the chip. The higher values of the heat transfer coefficient and its variation are largely due to the higher fluid velocity associated with the higher flow rate and the enhanced velocities, previously seen in Fig 41, at the center and sides of the silicon chip near the liquid inlet to the microgap channel.

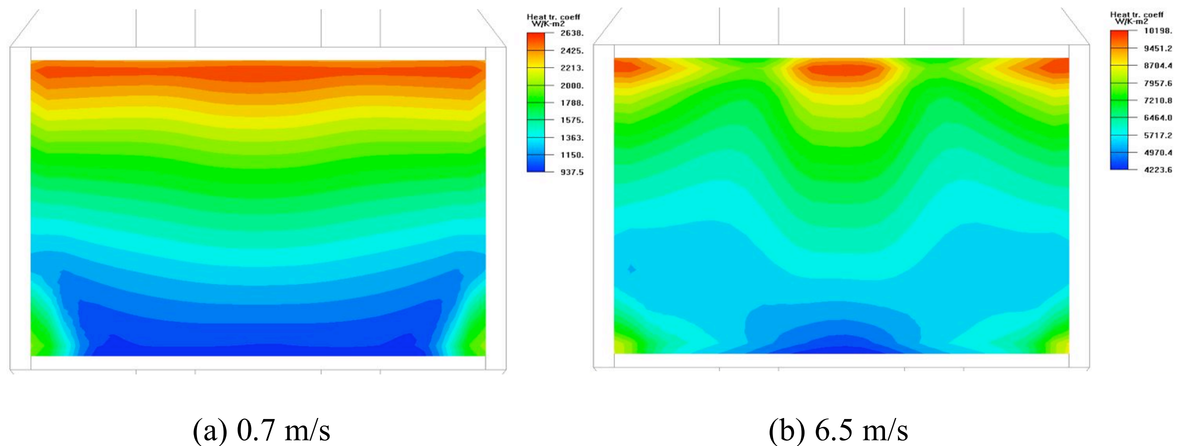

(a) 0.7 m/s (b) 6.5 m/s

Figure 49: Spatial Variation of Heat Transfer Coefficient for Uniformly Heated 100-micron Microgap Channel - (a) 0.7m/s (left), (b) 6.5m/s (right), Tin=23C.

The spatial (local) variations of heat transfer coefficient across the die surface for the half-die and quadrant-die non-uniform heating are shown in Figure 50 and 51, respectively. The slight difference of the heat transfer coefficient variations for these non-uniform heating cases is due to the higher non-uniformity and the skewed symmetry toward the higher heat flux zones of the chip compared to those of the uniform heating cases. Similar variation in the axial direction across the chip is seen in all cases due to the flow velocity profiles as noted earlier. It appears that the flow field dominates the behavior of the heat transfer coefficient and that due to conduction spreading in the chip the differences in the thermal boundary condition are minimized and have only a weak effect on the heat transfer coefficient distribution.

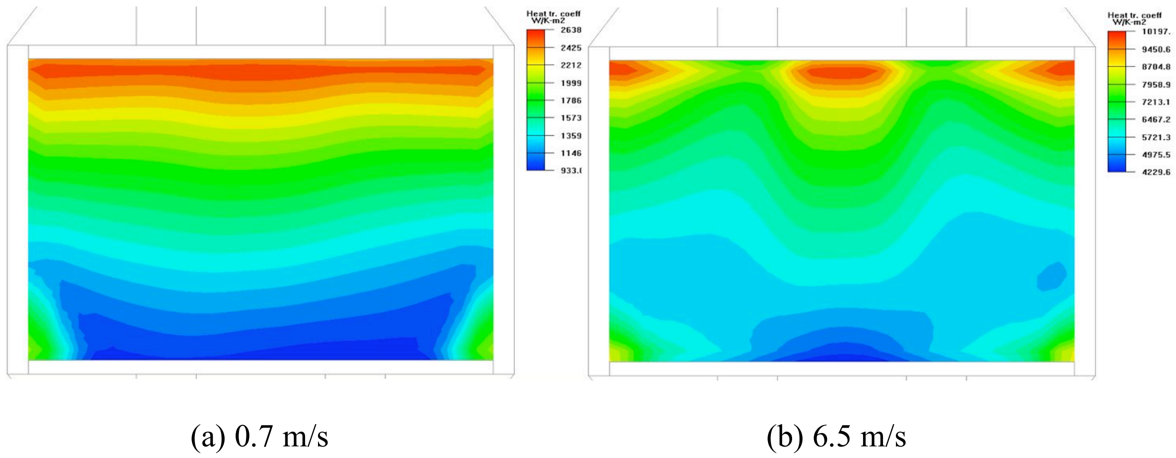

(a) 0.7 m/s (b) 6.5 m/s

Figure 50: Spatial Variation of Heat Transfer Coefficient for Half-Die Heated 100-micron Microgap Channel - (a) 0.7m/s (left), (b) 6.5m/s (right), Tin=23C.

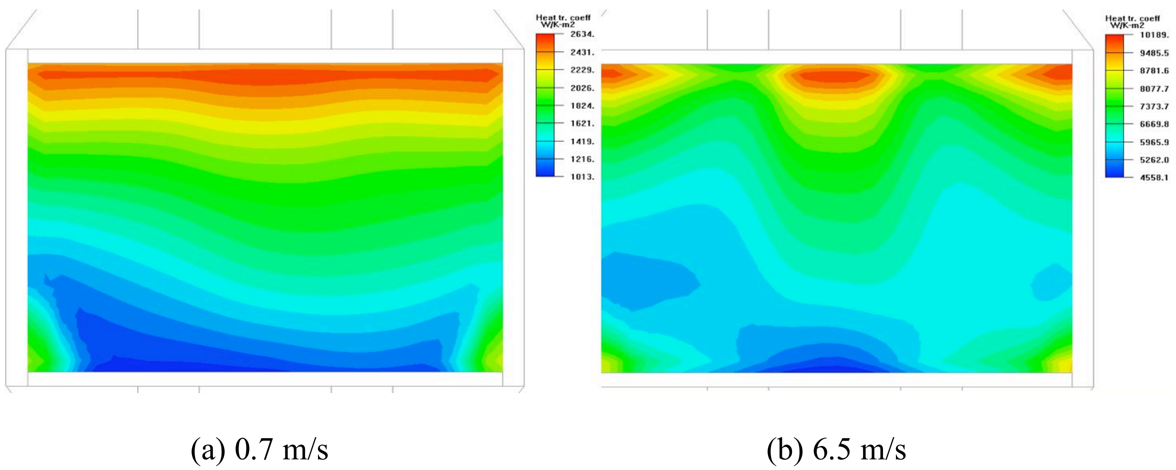

(a) 0.7 m/s (b) 6.5 m/s

Figure 51: Spatial Variation of Heat Transfer Coefficient for Quadrant-Die Heated 100-micron Microgap Channel - (a) 0.7m/s (left), (b) 6.5m/s (right), Tin=23C.

6.4 Overall single-phase hydraulic and thermal performance

The overall hydraulic (pressure drop) and thermal performance (heat transfer coefficient) of the micro gap cooler can be characterized as a function of flow rate, represented by the corresponding channel Reynolds number (Re,) for the various channel heights considered in this study, i.e., 100, 200 and 500-micron channels. The single-phase pressure drop and heat transfer coefficients obtained in this part of the study are shown in Figures 52 and 53, respectively. It is interesting to note that the Re is a linear function of the channel mass flow rate (or velocity) as the velocity-hydraulic diameter product ($v.D_h$) in Re equation is constant and equal to twice the velocity of the channel.

It is quite clear, and as expected, that the pressure drop increases with the Reynolds number in a nearly quadratic fashion, but this dependence is affected somewhat by the transition from laminar to turbulent flow at a Re of approximately 2300. Moreover, the pressure drop is also inversely proportional to the channel height for a fixed Re number (fixed velocity) and follows a second-degree polynomial as per the literature [26]. For a fixed velocity of 6.5 m/s the pressure drop increases from around 20,000 Pa for the 500-micron channel to 80,000 Pa for the 100-micron channel.

The heat transfer coefficient is also inversely proportional to the channel height for a fixed Re number (fixed flow rate.) The heat transfer coefficient varies as a pseudo linear function of Re number, for values that span the range from laminar flow (at the

low flow rates) to turbulent (at high velocities, above 5 m/s.) The heat transfer coefficient reaches approximately round 9 kW/m^{2}K for the 100-micron channel at Re = 3500 (6.5 m/s velocity) and decreases to below 4 kW/m^{2}K for the 500-micron channel. The relation between the heat transfer coefficient and Re is mathematically fit to a power function (as shown in the Figure 53) where the heat transfer coefficient varies as $Re^{0.57}$, $Re^{0.52}$ and $Re^{0.38}$ for the 100-, 200- and 500-micron channels, respectively. This is in the range of expected exponents of literature correlations for laminar developing flow and fully developed turbulent flow as the heat transfer coefficient varies between $Re^{0.33}$ and $Re^{0.8}$ for laminar developing flow and turbulent flow [25].

The single-phase hydraulic and thermal performance of the micro gap cooler, with water as coolant, was also studied. Figures 54 and 55, show the water-based pressure drop and heat transfer coefficient performance of micro gap channels as a function of Re.

The thermal performance for water is much better than with HFE-7100, providing heat transfer coefficients that are approximately three times larger than that of the HFE-7100 values. The heat transfer coefficient performance with water reaches a value of 27 kW/m^{2}K at 6.5 m/s velocity compared to 9kW/m^{2}K with HFE-7100 at the same velocity. The relation between the heat transfer coefficient and Re is mathematically fit to a power function (as shown in the Figure 55) where the heat transfer coefficient varies as $Re^{0.49}$, $Re^{0.33}$ and $Re^{0.38}$ for the 100-, 200- and 500-micron channels,

respectively. This is in the range of expected exponents of literature correlations for laminar developing flow and turbulent flow as the heat transfer coefficient varies between $Re^{0.33}$ and $Re^{0.8}$ for laminar developing flow and turbulent flow [25].

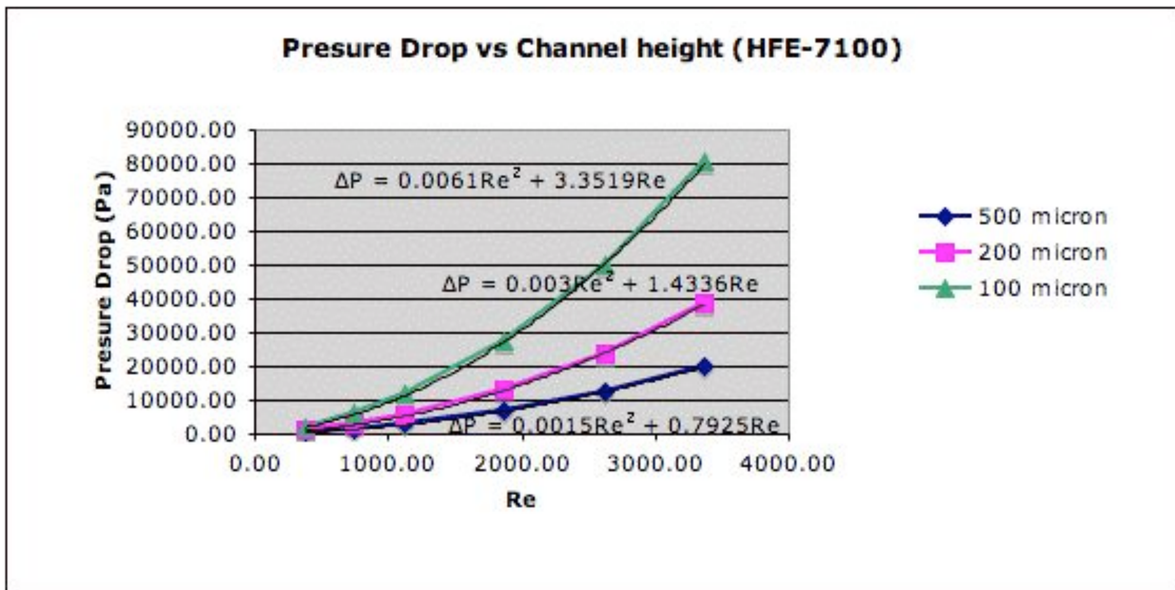

Figure 52: Pressure Drop vs. Re for a Microgap Channel with Various Channel Heights, flowing HFE-7100, T_{in}=23°C, q″=7W/cm^2.

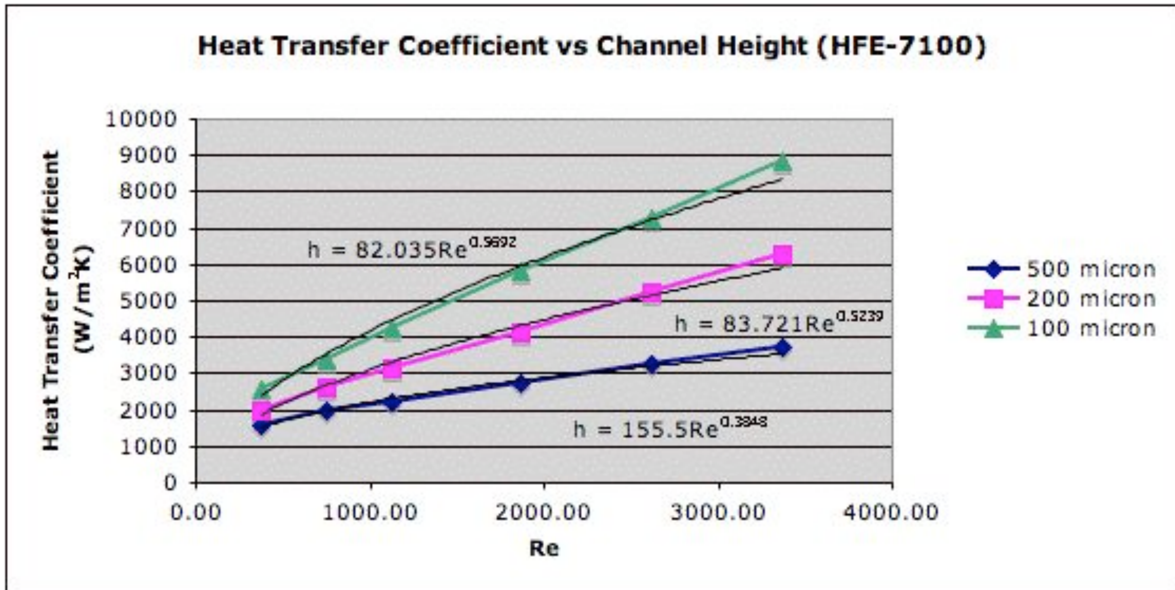

Figure 53: Heat Transfer Coefficient vs. Re for a Microgap Channel with Various Channel Heights, flowing HFE-7100, T_{in}=23°C, q″=7W/cm^2.

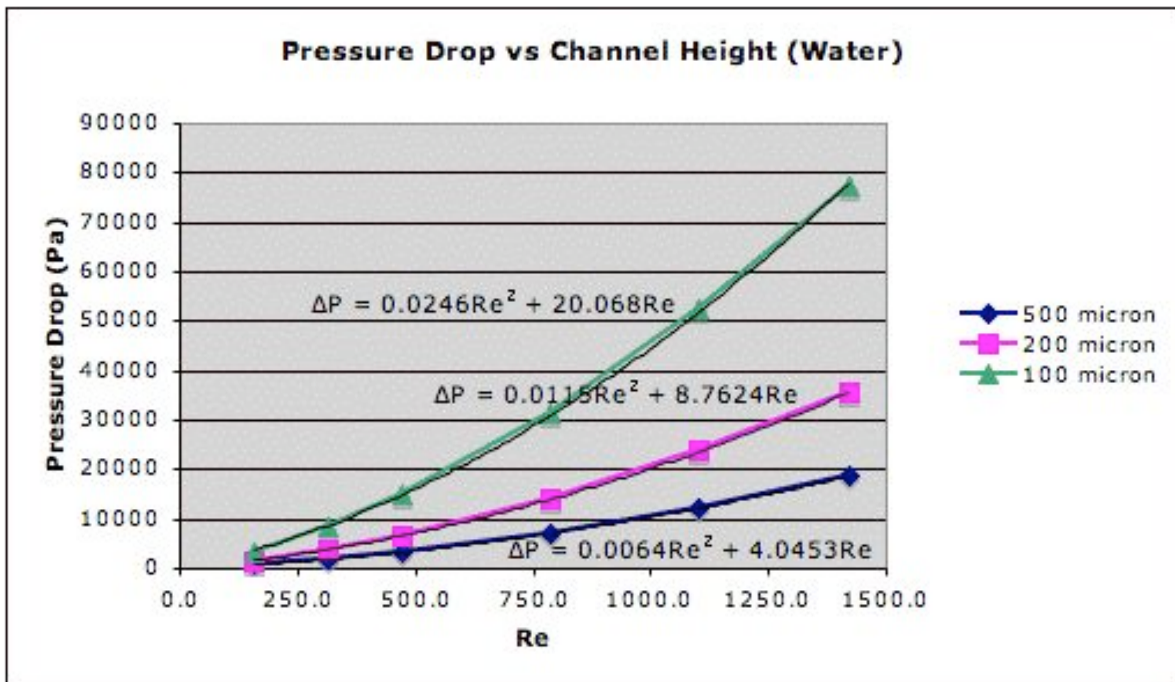

Figure 54: Pressure Drop vs. Re for a Microgap Channel with Various Channel Heights, flowing Water, T_{in}=23°C, q″=7W/cm^2.

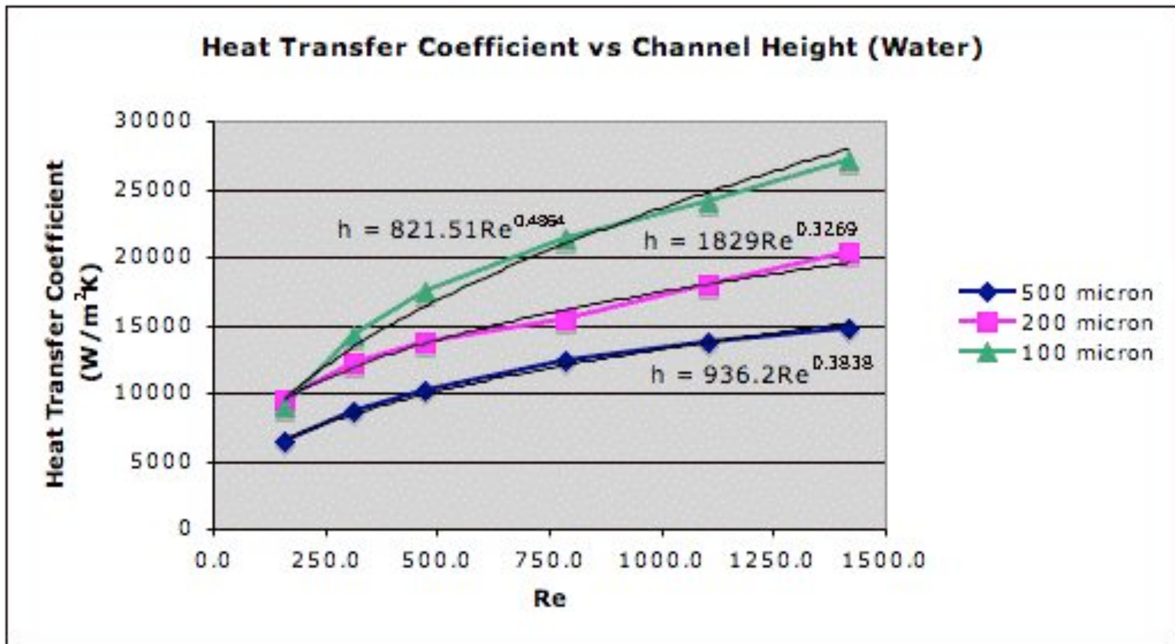

Figure 55: Heat Transfer Coefficient vs. Re for a Microgap Channel with Various Channel Heights, flowing Water, T_{in}=23°C, q″=7W/cm^2.

6.5 Conclusions

The chapter discusses in detail the various aspects of single-phase heat transfer for a chip-scale micro gap channel cooler. Overall pressure drop and heat transfer coefficient were studied for the various channels considered and with HFE-7100, as well as water, as the working fluids. The pressure drop was found to be inversely proportional to the channel height for a fixed Re number (fixed flow rate.) For HFE-

7100, the pressure drop, for a fixed velocity of 6.5 m/s, increases from around 20,000 Pa for the 500-micron channel to 80,000 Pa for the 100-micron channel. The heat transfer coefficient is also inversely proportional to the channel height for a fixed Re number (fixed velocity.) The heat transfer coefficient function is pseudo linear as a function of Re number spanning the range from laminar to turbulent at high flow rates (above 5 m/s.) For HFE-7100, the heat transfer coefficient reaches around 9 kW/m^2K for the 100-micron channel at around Re = 3500 (6.5 m/s velocity.) This heat transfer coefficient decreases to below 4 kW/m^2K for the 500-micron channel.

The single phase pressure drop performance of micro gap channels, with water, is similar to that of HFE-7100 across all Re. The thermal performance for water, however, is much better than with HFE-7100. It is around three times larger than that of HFE-7100. The heat transfer coefficient with water reaches a value of 27 kW/m^2K at 6.5 m/s velocity compared to 9 kW/m^2K with HFE-7100 at the same velocity.

The literature correlations for pressure drop and heat transfer coefficient are well suited for ideal channels with ideal boundary conditions, i.e., channel geometries with the characteristics of uniform the flow, laminar-developing flow, uniform thermal boundary conditions (flux or temperature) and neglected conjugate heat transfer effects. The present work focused on a practical channel (non-ideal) with developing flow, non-uniform heating, non-ideal geometry, and full conjugate heat transfer effects. Although single-phase correlations captured the general dependence of the pressure

drop and the heat transfer coefficient on the flow rate in this microgap channel, they have proven not to be accurate, especially at the low flow rate range. For HFE-7100 the average error of using the ideal channel pressure drop correlation is 24% and is highest at the low velocity range (0.7-1.5 m/s.) Similarly, the average heat transfer coefficient error is 7% and is highest at similar low velocity range (0.7-1.5 m/s.) Numerical modeling using computational fluid dynamics software (CFD) was used in order to overcome the inappropriateness of the available correlations. A CFD model predicted well the conjugate heat transfer effects (the rate of heat dissipated by the fluid as convective flow) versus the heat conducted through the chip substrate. It was found, as predicted, that this conversion rate increases proportionally with the flow rate and inversely with the channel height. Furthermore, CFD simulations correlated well with experimental data with an error of 5% and much better than ideal channel-based literature correlations (20% error) as the CFD model takes into account all the geometric and boundary condition complexities not considered in the simple correlations. CFD modeling not only predicted well the overall pressure and the heat transfer coefficient for the various channels considered (5% error) but also predicted well the junction plane temperature distribution. Another very important and rather critical aspect that CFD modeling uncovered was the spatial distribution of heat flux at the wall (die top surface) and resultant wall spatial the heat transfer coefficient. Conduction spreading of the die silicon block (800-micron thick) played an important role in changing the wall heat flux variations for all heating patterns considered (uniform and non-uniform.) It was found that silicon conduction did obscure the

serpentine pattern on the wetted surface but always resulted in highly non-uniform heat flux at the wall even when the heat was applied across the entire junction plane of the chip. This provides a clear explanation for why available uniform heat flux correlations failed to predict accurately the heat transfer coefficient. Knowing the wall spatial variations of temperature and heat flux, CFD was used to inversely calculate the spatial variations of wall the heat transfer coefficient. The spatial the heat transfer coefficient was more non-uniform with non-uniform heating and was characterized by the skewed symmetry toward the higher heat flux zones of the chip compared to uniform heating**.** The flow field dominates the behavior of the heat transfer coefficient and due to conduction spreading in the chip the differences in the thermal boundary condition are minimized and have only a weak effect on the heat transfer coefficient distribution.

Chapter 7:

Two-Phase Heat Transfer Experimental Data and Discussion

7.1 Introduction and basic relations

Two-phase heat transfer experiments of the 100, 200 and 500-micron channels, with HFE-7100 coolant, with three different heating patterns (uniform, half die and quadrant die heating,) were performed and analyzed under fully saturated conditions. As noted in Chapter 3, the saturated two-phase experiments were performed on a silicon thermal test chip resembling a commercially available microprocessor with a total die surface area of 1.44 cm^2. The thermal test chip was mounted in a hermetically sealed chamber, with a predetermined channel height, i.e., 100-, 200- and 500- micron, whereby cooling fluid HFE-7100 was pumped into it at a preset flow rate. An in-line heater was used to heat up the fluid, incoming into the test channel, in order to achieve the saturated condition immediately at the channel inlet. This saturated liquid condition was determined by cross comparing the fluid inlet temperature against the fluid inlet pressure, measured by the installed absolute pressure transducer, at the channel inlet.

The thermal chip is 13.75 mm wide and 10.47 mm long (along the flow direction.) This very short length is a key characteristic of this non-ideal channel as it causes the fluid to be developing in the entire channel. The chip is heated by an embedded

serpentine heater at the junction plane of the silicon thermal chip. The embedded heater enabled for various levels of heat fluxes at the thermal chip and various heating patterns, i.e., uniform heating, half-die and quadrant-die non-uniform heating. A detailed and overall description of the microgap channel two-phase apparatus is found in Chapter 3.

The wall (die top surface) temperatures were captured by nine embedded temperature diodes (sensors) spread at various locations at the thermal chip junction plane. The heated (two-phase) fluid exiting the microgap channel is run through an externally water-cooled flat plate heat exchanger to condense the two-phase mixture. The condensate fluid is pumped through a centrifugal pump at a pre-determined flow rate back into the channel through the in-line heater. A flow rate meter is installed at the outlet of the pump to measure the fluid flow rate.

A set of saturated two-phase experiments were run through the 100, 200 and 500 micron channels, with variable mass flow rates and variable heat fluxes at the thermal test chip.

The average wall temperature was calculated by averaging out the nine temperature sensors embedded in the test chip. The heat conversion rate, i.e., the percentage of heat going into the test channel as opposed to the heat conducted through the chip substrate into the test board, is extracted from the output of the pseudo two-phase CFD model based on the validated single-phase CFD model. The model, for each fixed flow rate, heat flux and channel height, was run iteratively by altering the fluid properties until

the wall average temperature agreed with the experimental temperature data. The CFD model can then provides the heat going into the channel versus the heat conducted into the substrate, thus helping to resolve the conjugate heat transfer problem. The heat flux is calculated by dividing the calculated “conversion rate” (i.e., heat flowing into the channel) by the entire chip surface area (1.44 cm^2). The two-phase exit quality of the channel is calculated using the fully saturated channel energy equation as:

$$q'' \cdot A = \dot{m} \cdot h_{fg} \cdot x \tag{7.1}$$

Where q'' is the heat flux into the channel, A is the chip surface area, $\dot{m}$ is the mass flow rate, h_{fg} is the latent heat of vaporization and x is vapor exit quality. Due to the very short microgap channel length, this calculated exit quality is used to characterize the two-phase state of the test channel. The wall average two-phase channel heat transfer coefficient is calculated by

$$q'' = h_{TP}(T_{Wall} - T_{Sat}) \tag{7.2}$$

Where h_{TP} is the wall average two-phase heat transfer coefficient, T_{wall} is the wall average temperature and T_{sat} is the channel average saturation temperature.

The uncertainty in the two-phase heat transfer coefficient, obtained from the channel energy balance equation above, is linear and is affected by the uncertainties in the

measured quantities including the flow rate, the temperature of the wall (die sensors), the temperature at the inlet, and the stability of the data logger and power supply. It can be expressed mathematically as

$$\left(\frac{\delta h}{h}\right)^2 = \left(\frac{\delta \dot{m}}{\dot{m}}\right)^2 + \left(\frac{\delta q}{q}\right)^2 + \left(\frac{\delta \Delta T_{wall}}{\Delta T_{wall}}\right)^2 \tag{7.3}$$

Where δh is uncertainty of heat transfer coefficient, $\delta \dot{m}$ is the error of flow rate via the flow meter, δq is error of input power via the power supply, $\delta \Delta T_{wall}$ is the measurement error of wall super heat temperature. The flow meter's flow rate error is ± 1.5%. The error of the power supply is ± 2.5%. The maximum error in the wall super heat temperature measurement is ± 0.25°C which causes maximum error of 1%. Thus, the possible maximum error of measuring the two-phase heat transfer coefficient is ±3.1%.

The single-phase heat transfer experimental work detailed in Chapter 5, served to validate the overall approach of measuring the channel heat transfer coefficient while identifying the difficulty in applying classical correlations to actual chip cooling with all the non-idealities we have encountered including flow-based, geometrical, boundary conditions non-idealities.

The experimental data were reported as average heat transfer coefficient h_{TP} versus wall average heat flux, q'', and vapor quality, x, for the range of mass fluxes considered. The mass flux (G), for each experiment, was calculated by dividing the mass flow rate $\dot{m}$ by the channel cross-section area.

The range of mass flux considered was 350 kg/m^{2}s to 1500 kg/m^{2}s reflecting an overall flow rate range of 0.4-3 ml/s. The range of heat flux considered was 20-250 kW/m^2. The area average heat transfer coefficient data for uniform heating is plotted against the channel heat flux and the calculated vapor quality at the channel exit as shown in Figures 56, 57 and 58, respectively.

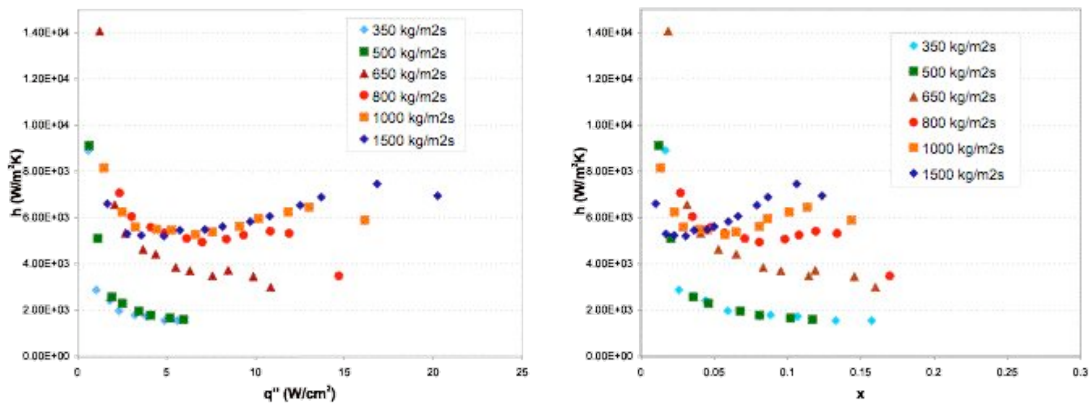

Figure 56: Two-phase h vs. q″ and x for Uniform Heated 100-micron Channel Flowing HFE-7100.

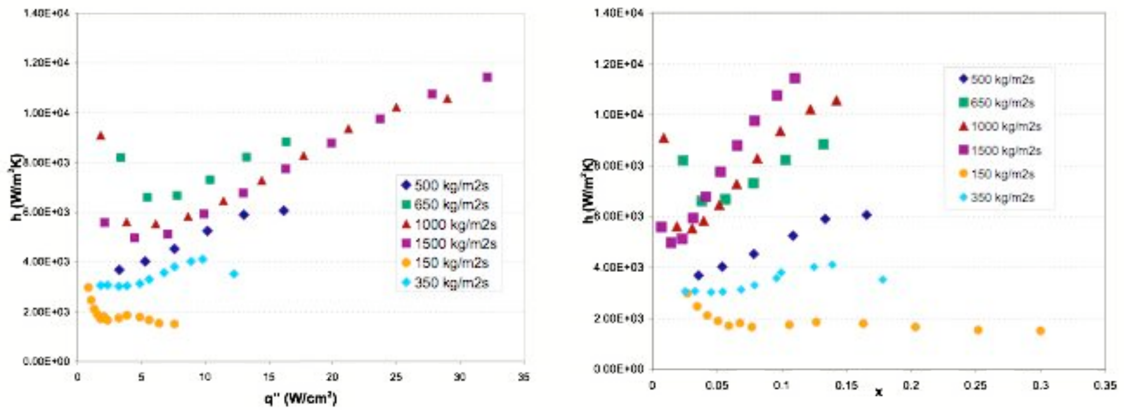

Figure 57: Two-phase h vs. q″ and x for Uniform Heated 200-micron Channel Flowing HFE-7100.

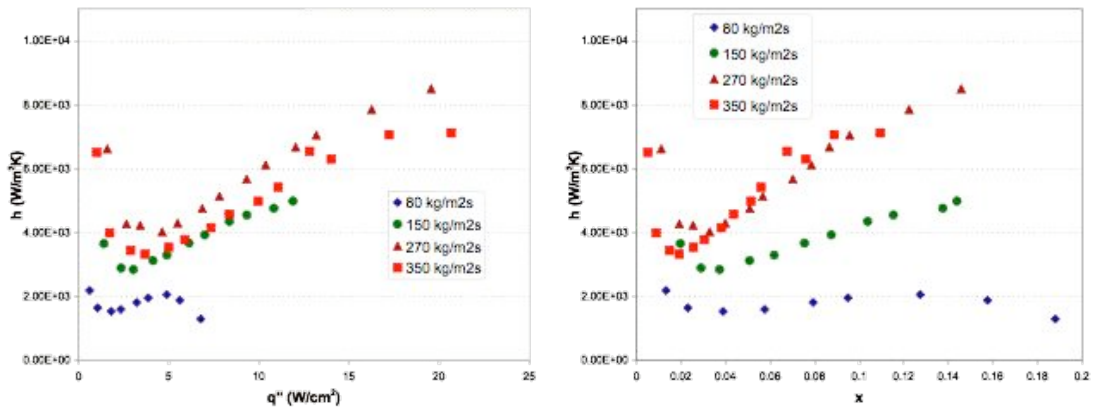

Figure 58: Two-phase h vs. q″ and x for Uniform Heated 500-micron Channel Flowing HFE-7100.

7.2 Taitel-Dukler Flow Regime Map

Following Bar-Cohen and Rahim [20], classical Taitel-Dukler flow regime modeling was performed on the 100-, 200- and 500-micron uniformly heated channels and the

locus of the two-phase mixture, as well as the heat transfer coefficient data, was superimposed on the TD flow regime maps, as shown in Figures 59-61.

The map's coordinates are the superficial gas velocity and superficial liquid velocity given by

$$U_G^S = x\frac{G}{\rho_G} \qquad U_L^S = (1-x)\frac{G}{\rho_L} \tag{7.4}$$

Where U_G^S is the superficial gas velocity and U_L^S is the superficial liquid velocity while G (kg/m^{2}s) is the mass flux, x is the exit quality and ρ_G and ρ_L (kg/m^3) are the gas and liquid density, respectively.

The TD map model determines the flow regime, i.e., Stratified, Bubbly, Intermittent or Annular, for each binary set of superficial gas velocity and superficial liquid velocity values.

The channel average heat transfer coefficient data calculated for various heat fluxes are overlaid on the TD maps as a function of the superficial gas velocity (representing the exit quality x) for a specific mass flux G.

The map has a characteristic angled transition line between the Annular and Intermittent flow regimes (as shown in Figs 59-61). A modified Intermittent/Annuar transition line was proposed by Rahim et al [57]. The modified line is a vertical one at a fixed superficial gas velocity (as shown in Figs 59-61). The basis for the modified vertical transition line will be discussed later.

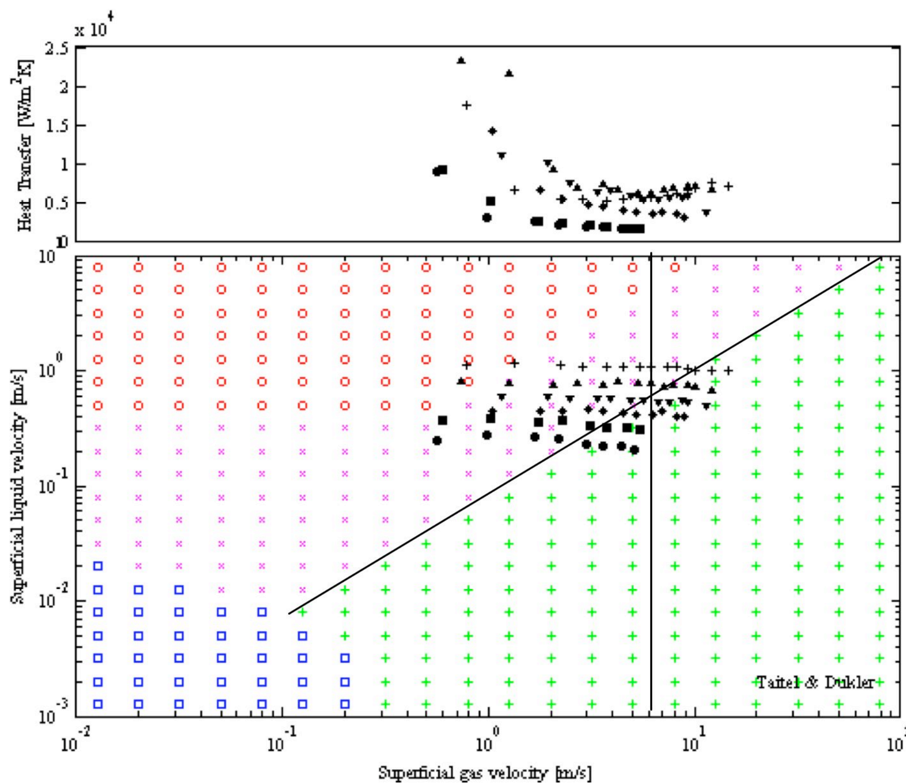

Figure 59: Taitel-Dukler Map with Flow Regimes and h's for Uniform Heating and 100-micron Channel. G=350, 500, 650, 800, 1000 and 1500 kg/m^{2}s.

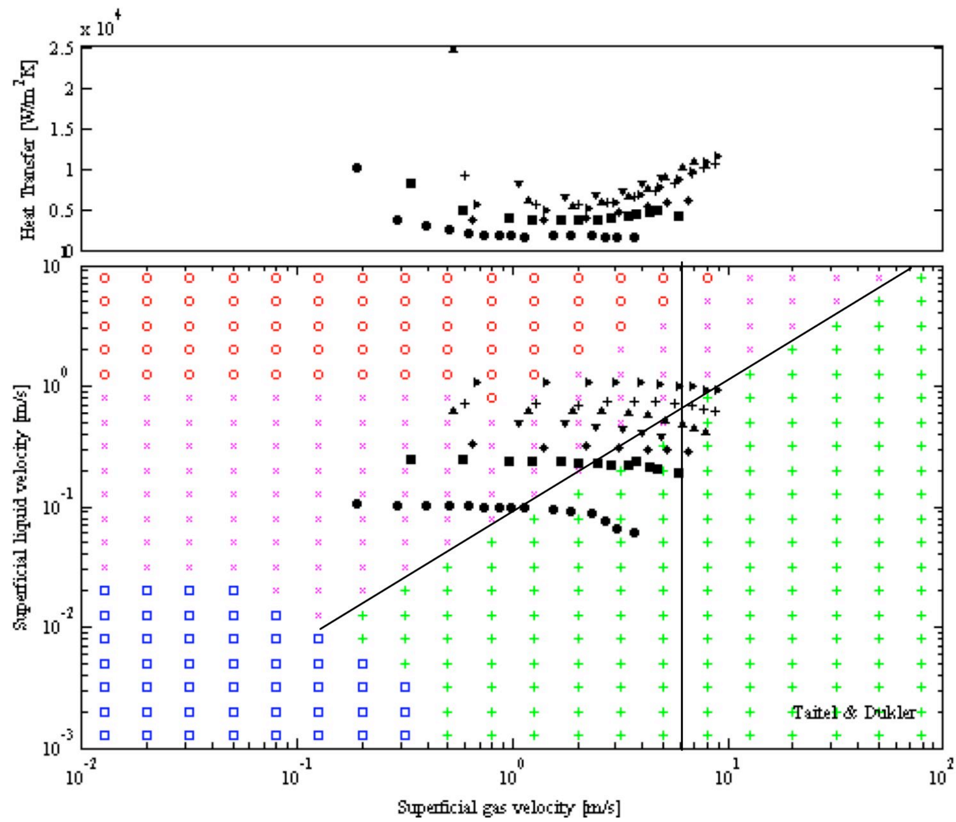

Figure 60: Taitel-Dukler Map with Flow Regimes and h's for Uniform heating and 200-micron Channel. G=150, 350, 500, 650, 800, 1000 and 1500 kg/m^{2}s.

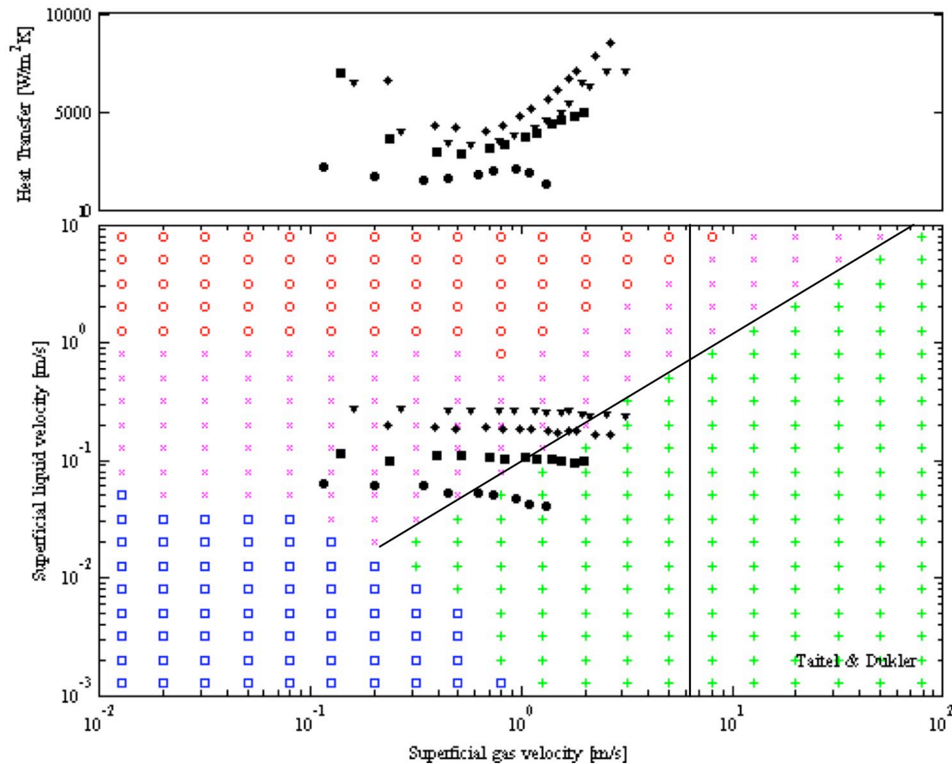

Figure 61: Taitel-Dukler Map with Flow Regimes and h's for Uniform Heating and 500-micron Channel. G=80, 150, 270 and 350 kg/m^{2}s.

Examining Fig 59, the flow regime map for the uniformly heated channel wall, it may be seen that the two-phase loci for the mass fluxes examined in this study (350-1500 kg/m^{2}s) traverse the superficial velocity plane at relatively high liquid velocities, entering in (or close to) Bubble flow progressing through the Intermittent regime, and terminating in the Annular regime. In this classical Taitel-Dukler map, the Intermittent regime appears to dominate the behavior of the uniformly heated microgap channel for the operating conditions studied. Similar observations can be made on the 200- and 500-micron channel flow regime maps shown in Figures 60 and 61, respectively. The

two-phase loci for these channels, with the mass fluxes studied (150-1500 kg/m^2s for the 200-micron channel and 80-350 kg/m^2s for the 500-micron channel) experience similar behavior to that of the 100-channel, however at lower overall superficial liquid velocities such that the loci dos not start with Bubble but rather with Intermittent regime (especially with the 500-micon channel) terminating at the Annular regime.

Although this mapping methodology has been used successfully for miniature channels [20] and has helped to establish that Annular flow is the dominant flow regime for two-phase flow in this form factor, it is to be noted that the present 100-micron microgap channel, with the exception of the study by Kim et al [19], is substantially smaller than, and operates at relatively higher mass fluxes, than nearly all the data examined in the past. While the Tabatabai and Faghri flow regime map [44] attempts to define a flow regime map for very small diameter tubes, Fig 62 reveals that this map differs only in the boundary between Bubble and Intermittent flow and does not alter the location of the Annular flow regime. It has also been suggested that the Confinement Number, Co, defined as the ratio of the theoretical bubble departure diameter to the tube diameter, could be used to identify true micro-channels [30]. For $Co > 0.5$, individual vapor bubbles could be expected to fill the entire tube, leading to Intermittent flow, and Co substantially larger than unity, as occurred in the present work ($Co = 4.5$ for 100-micron channel and HFE-7100 coolant), would appear to imply that Annular flow prevails in the channel.

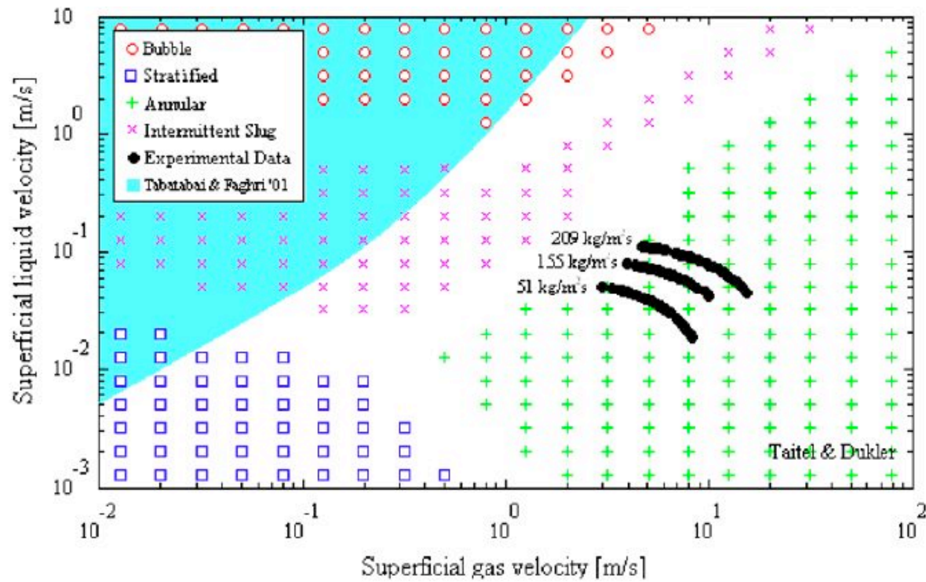

Figure 62: Tabatabai & Faghri's Modification to the Taitel-Dukler Map Showing the Proposed Transition Line to Annular Flow [20].

Interestingly, Rahim et al [57] recently completed a detailed analysis of the flow regimes encountered in the flow of refrigerants in sub-millimeter tubes. While the T&D map was found to properly account for 2/3rds of the observations, use of modified criteria for the transition from Intermittent to Annular flow, along with a modification of the Bubble-to-Intermittent boundary, resulted in a correct determination of the flow regime for more than 90% of the experimental data. A modified Intermittent/Annular transition superficial gas velocity was proposed as

$$U_G^S = \frac{6.2[\sigma g(\rho_L - \rho_G)]^{1/4}}{\rho_G^{1/2}} \tag{7.5}$$

This modified transition line, is also defined as a function of Weber number and Bond number, as

$$\frac{We^{1/2}}{Bo^{1/4}} = 6.2 \tag{7.6}$$

Applying this modified transition superficial gas velocity to HFE-7100 yields a transition value of $U_G^S = 6.55$ m/s. This modified vertical transition line, along with the original diagonal transition line, were superimposed on Figs 59-61 for the TD maps for the 100, 200 and 500-micron channels, respectively. The proposed vertical transition line, superimposed on the 100- and 200-micron channels, leads to more data points falling in the Annular regime at higher mass fluxes while it makes all the data points fall in the Intermittent regime at the low mass fluxes. While on the 500-micron channel, the proposed vertical transition line makes the entire data set fall in the intermittent regime.

Taitel-Dukler flow regime modeling was also performed on the 100-, 200- and 500-micron non-uniformly heated channels and the locus of the two-phase mixture, as well as the heat transfer coefficient data, was superimposed on the TD flow regime maps. The two types of non-uniformity studied are half-die and quadrant-die heating, and

their TD flow regime maps as shown in Figures 63-65 and Figures 66-68, for the two heating types, respectively.

Examining the TD maps for the non-uniformly-heated channels in Figs 63-65, shows that the two-phase loci for the mass fluxes examined in this study experience similar trends to the uniformly heated channel, as they traverse the superficial velocity plane at relatively high liquid velocities, entering in Bubble or Intermittent flow, depending on the channel diameter, progressing through the Intermittent regime, and terminating in the Annular regime, with the exception of higher mass fluxes (1000-1500 kg/m^{2}s) as they terminate at the Intermittent (or at boundary of Intermittent-Annular) regime. Intermittent regime appears to dominate the behavior of the non-uniformly heated channel (similarly to the uniformly-heated channel) for the operating conditions studied.

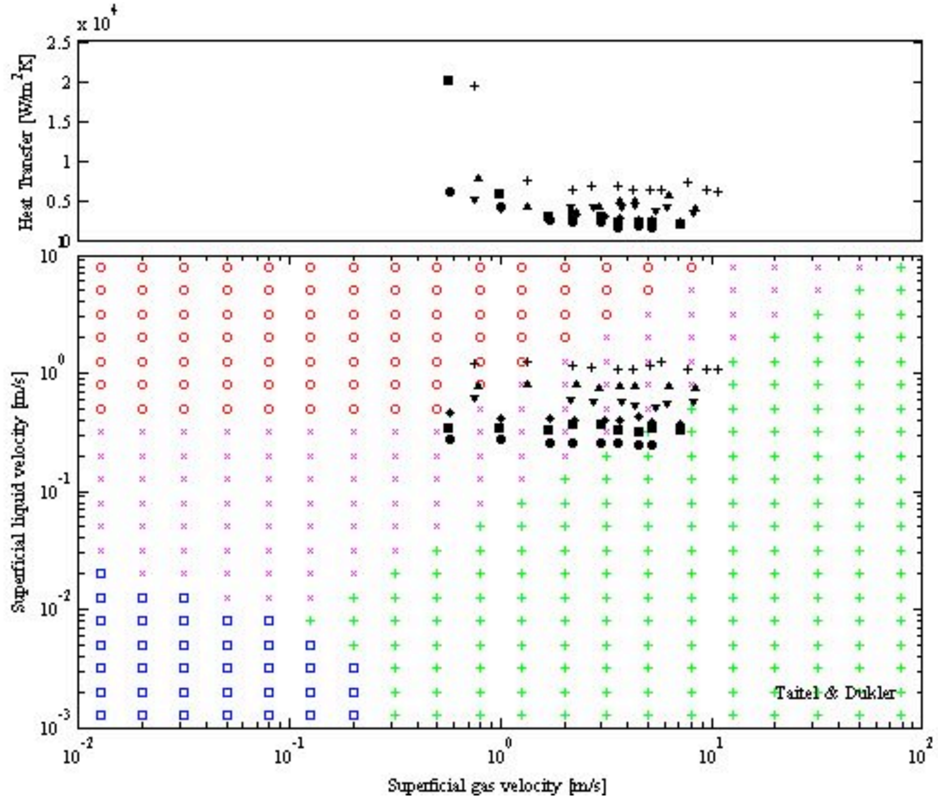

Figure 63: Taitel-Dukler Map with Flow Regimes and h's for Half-Die Heating and 100-micron Channel. G=350, 500, 650, 800, 1000 and 1500 kg/m^{2}s.

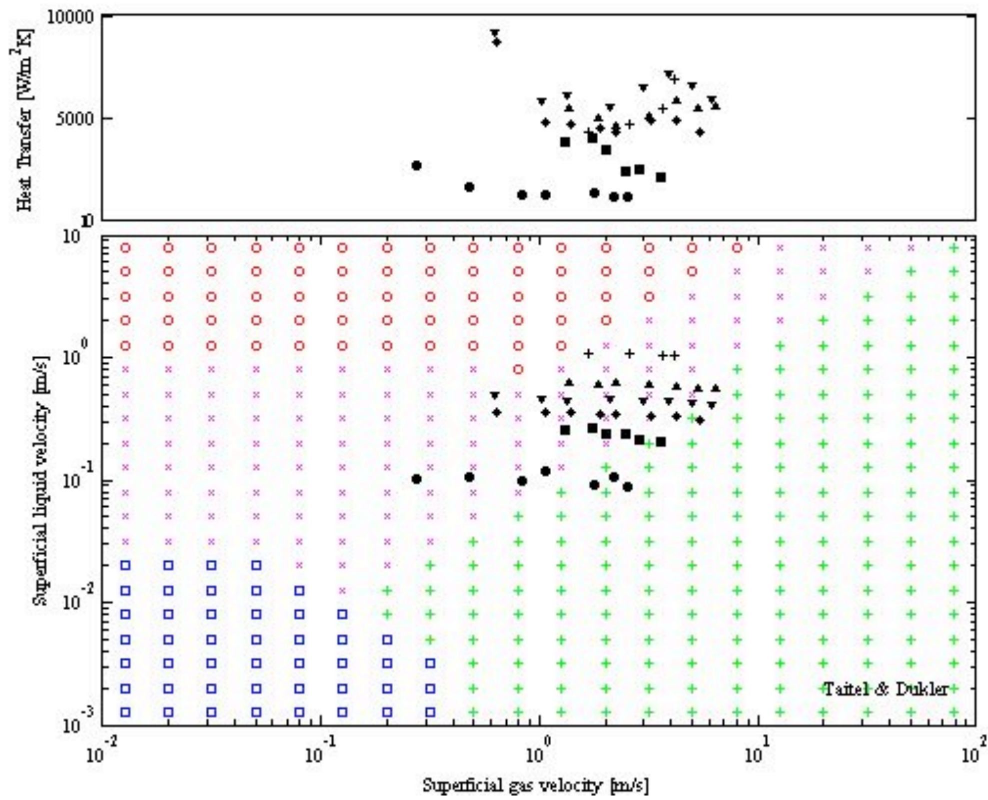

Figure 64: Taitel-Dukler Map with Flow Regimes and h's for Half-Die Heating and 200-micron Channel. G=150, 350, 500, 650, 800 and 1500 kg/m²s.

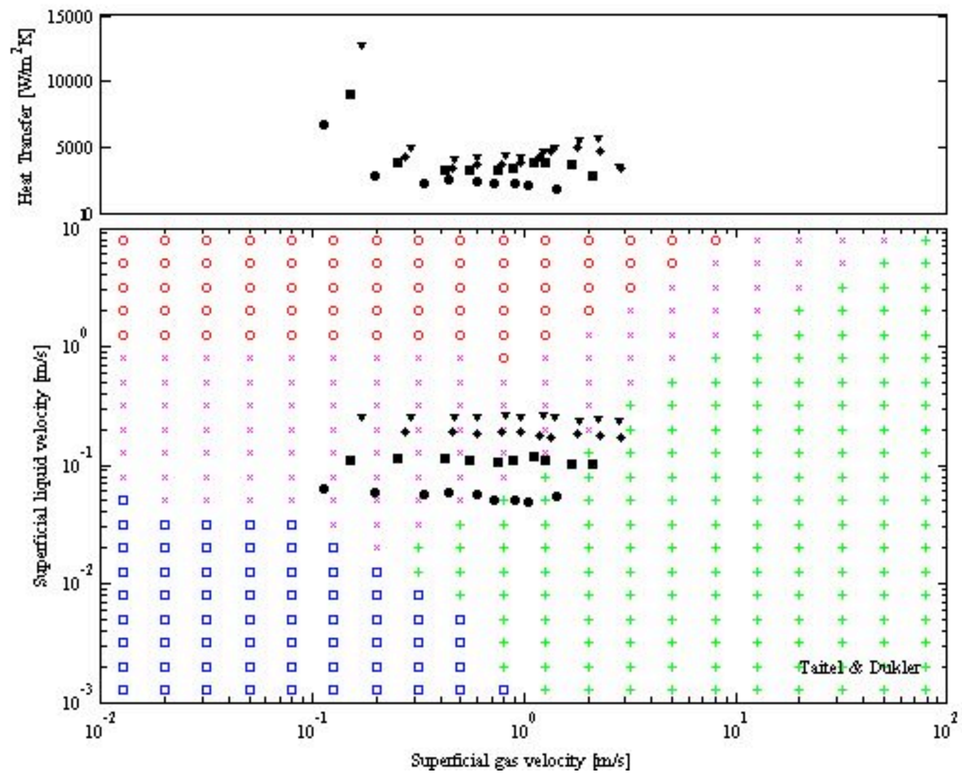

Figure 65: Taitel-Dukler Map with Flow Regimes and h's for Half-Die Heating and 500-micron Channel. G=80, 150, 270 and 350 kg/m^{2}s.

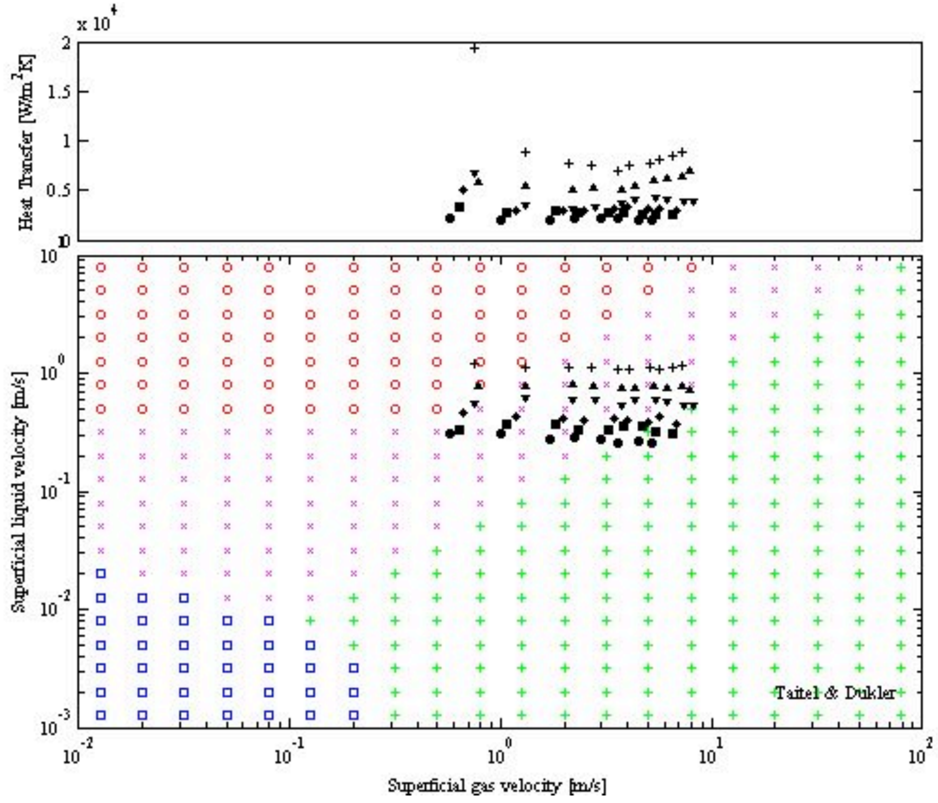

Figure 66: Taitel-Dukler Map with Flow Regimes and h's for Quadrant-Die Heating and 100-micron Channel. G=350, 500, 650, 800, 1000 and 1500 kg/m^{2}s.

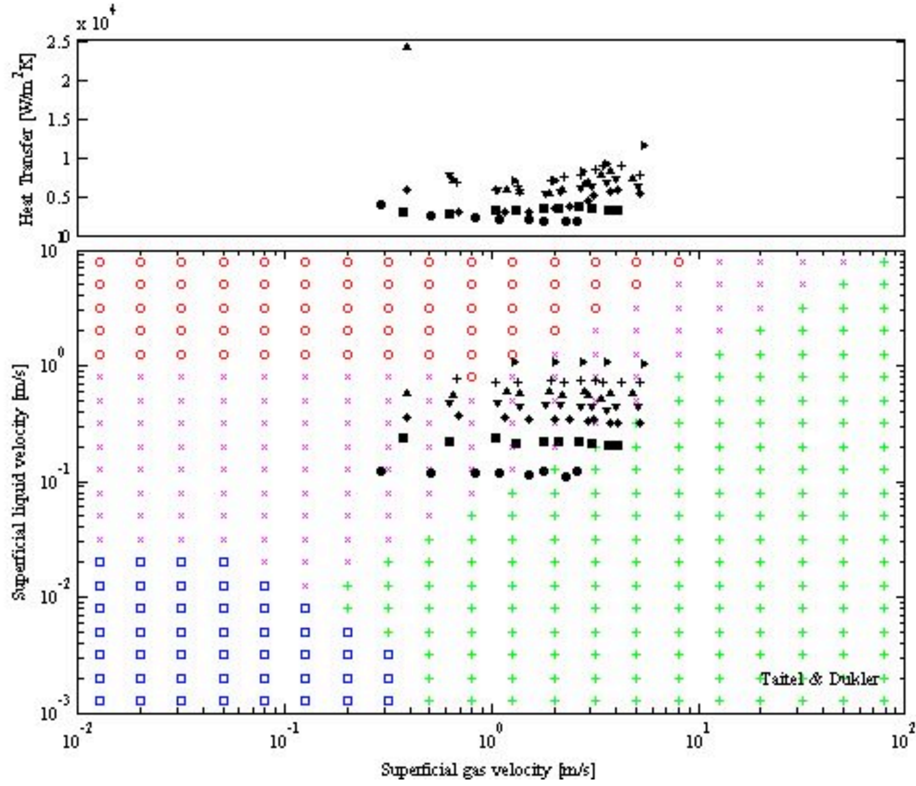

Figure 67: Taitel-Dukler Map with Flow Regimes and h's for Quadrant-Die Heating and 200-micron Channel. G=150, 350, 500, 650, 800, 1000 and 1500 kg/m^{2}s.

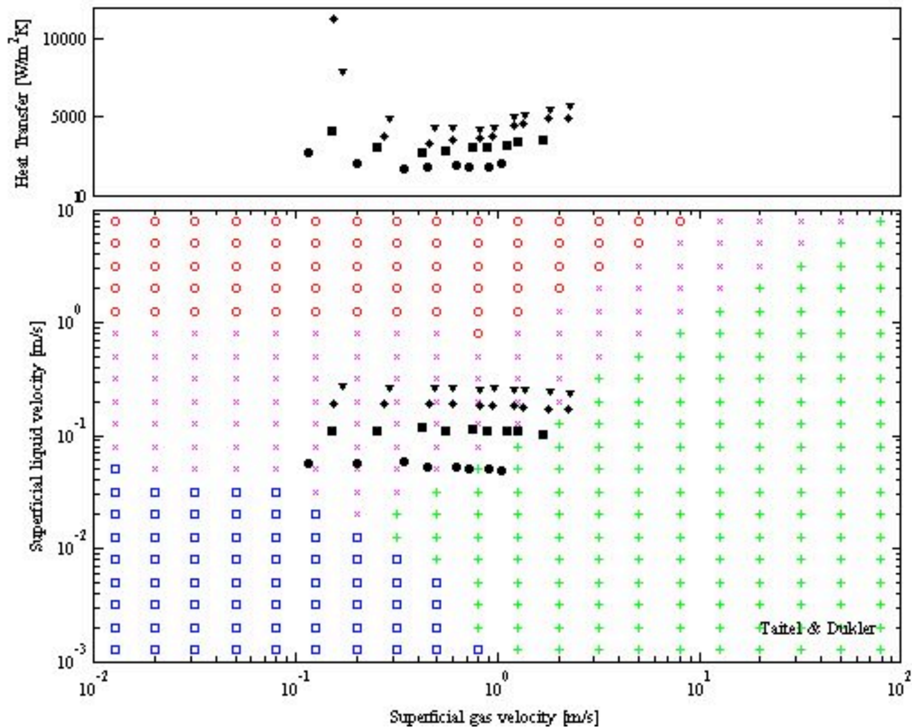

Figure 68: Taitel-Dukler Map with Flow Regimes and h's for Quadrant-Die Heating and 500-micron Channel. G=80, 150, 270 and 350 kg/m^{2}s.

7.3 Heat transfer characteristics

As previously indicated the figures containing the predicted flow regime maps for uniformly heated 100 micron channel, i.e., Figs 59-61, also display the variation of the surface-average heat transfer coefficient with the exit superficial velocities. Examining Fig 59, it may be seen that for most of the mass fluxes studied the heat transfer coefficients at low qualities (or superficial vapor velocity) display values close to 10 kW/m^{2}K and then decrease steeply as the quality increases, bottoming at heat transfer coefficient of 3-4 kW/m^{2}K, then reversing and rising modestly or substantially

depending on the specific conditions. Some of the operating conditions display a second maximum at higher qualities and then revert to lower h values.

The two-phase average heat transfer coefficients vs. exit quality, for the 100, 200- and 500-micron channels, shown in Figs 56-58 appear to display the key segments of the M-shape characteristic curve reported in the literature for two-phase flow in miniature channels [20].

Thus the data from Yang and Fujita [37] using R113 refrigerant and Diaz et al [38] using n-Octane, presented by Bar-Cohen and Rahim [20] and displayed in Fig 69, clearly show this behavior, with a decreasing trend in intermittent flow, a minimum close to the transition to Annular flow, then a positive slope and a second peak for h in the Annular regime, at higher qualities. While this characteristic behavior, including the second peak is seen in the present data, for the 100-micron channel, the inflection points do not correspond well to the regime transition shown in the classical T&D map. Alternatively, when the recently proposed Intermittent/Annular transition criteria [57] is applied to the present data, the heat transfer coefficient trough is seen to correspond more closely to the onset of Annular and the up-sloping branch of the h curve is almost entirely contained within the Annular regime.

The 100-micron channel data as well as the 200-micron and 500-micron channels are plotted in Figures 70, 71 and 72, respectively, and show that heat transfer coefficient

curve, across the various ranges of mass flux, can be mathematically fitted with a third-degree polynomial that is characterized by a minimum point right after the transition to from intermittent to annular flow and a maximum point (peak) in annular flow before dry-out starts taking place. It should be noted that the heat transfer coefficient curves at low mass fluxes, for example, those of the 100-micron channel at 350-650 Kg/m^{2}s do not show a distinctive minimum before the transition to Annular regime and a distinctive peak at the Annular regime and could also be fitted by a descending power function. However, examining Figs 71 and 72, for the 200-micorn and 500-micron channels, respectively, it is seen that the third-degree polynomial is the more general form of the heat transfer coefficient variation with quality.

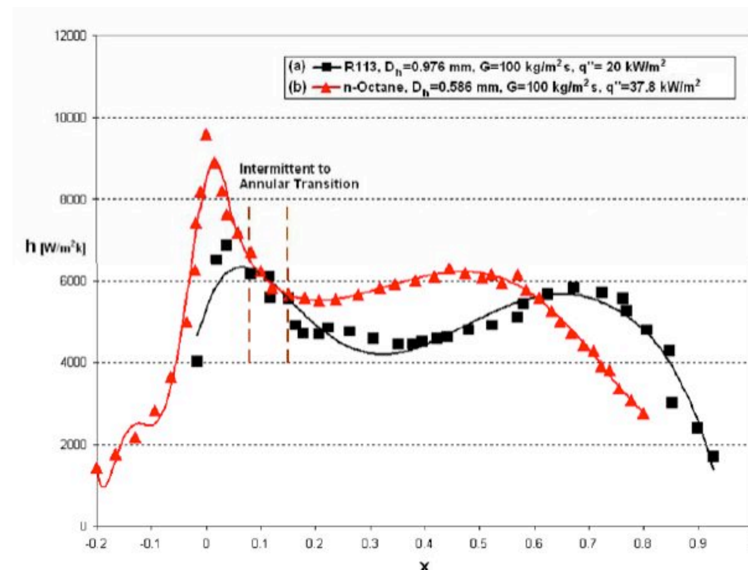

Figure 69: Two-Phase h vs. Exit Quality x of the Yang&Fujita [37] and Diaz et al [38] Data [20].

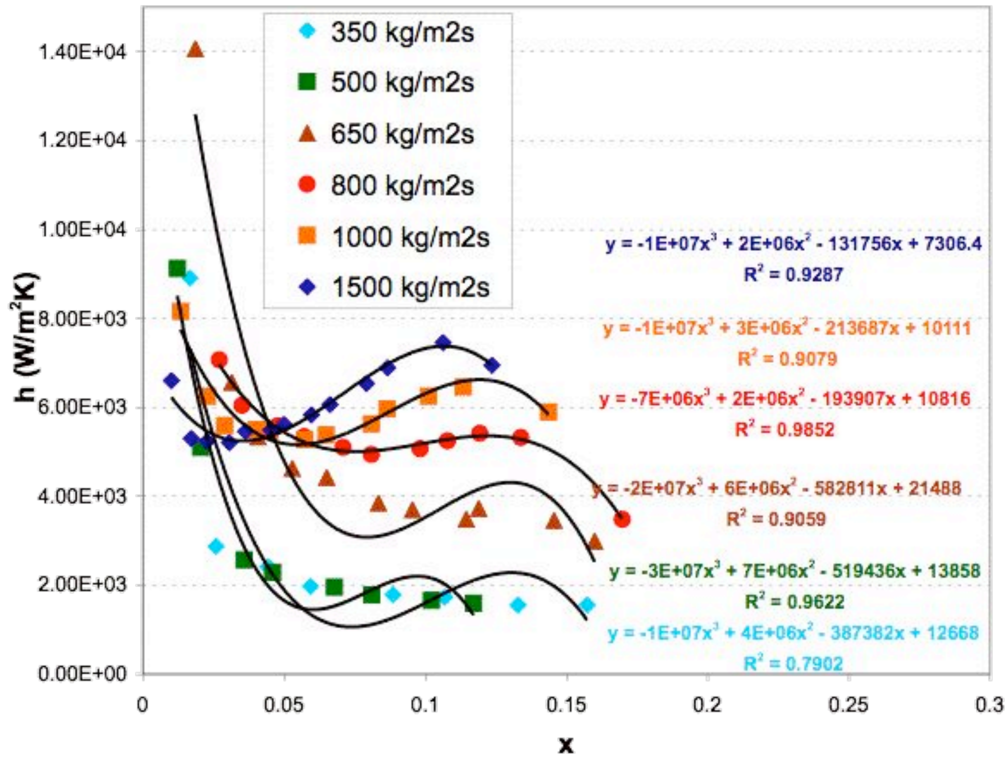

Figure 70: Two-Phase h vs. Exit Quality x of the Uniformly Heated 100-micron Microgap Channel.

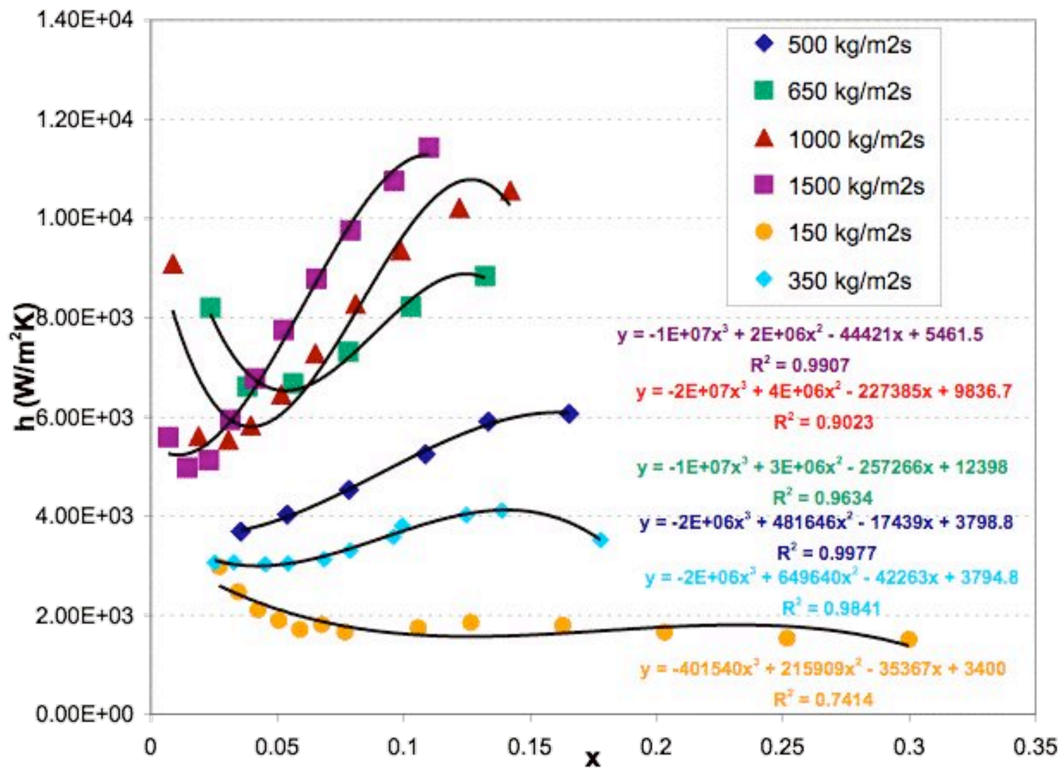

Figure 71: Two-Phase h vs. Exit Quality x of the Uniformly Heated 200-micron Microgap Channel.

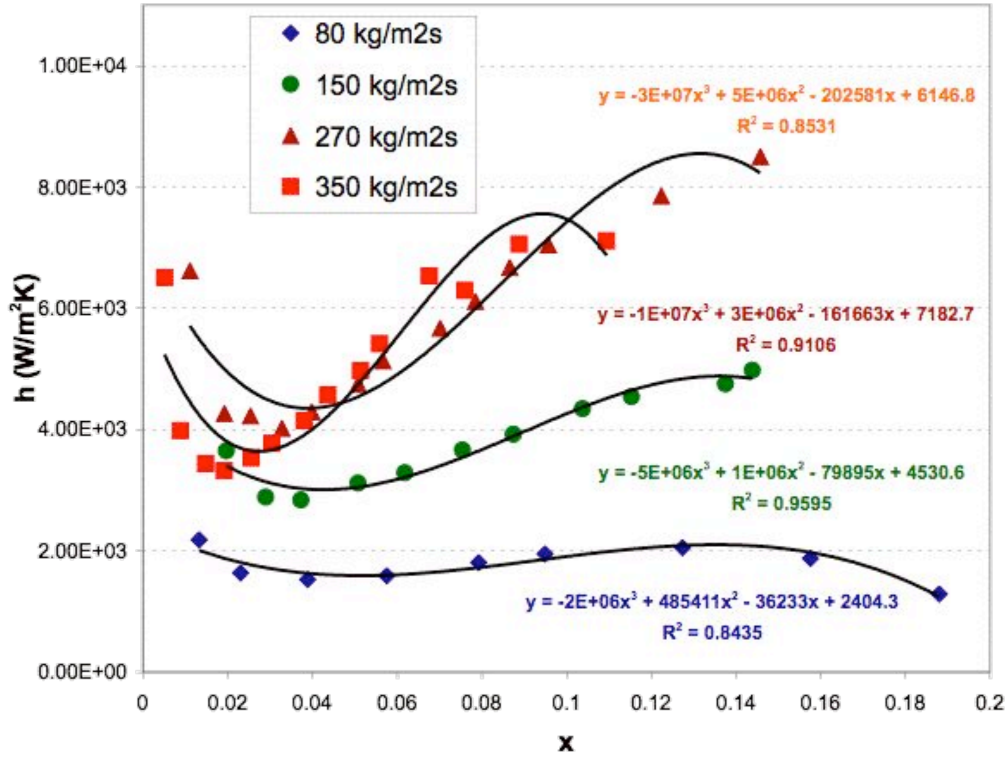

Figure 72: Two-Phase h vs. Exit Quality x of the Uniformly Heated 500-micron Microgap Channel.

It may be observed that, with the exception of the mass flux of 270 kg/m^{2}s in the 500-micron channel, for each channel diameter the higher the mass flux the higher the achievable two-phase heat transfer coefficient. It should be noted that in two-phase flow in the 100-micron channel, the peak heat transfer coefficient in the Annular flow regime reaches ~ 7-.8 kW/m^{2}K at G=1500 kg/m^{2}s and vapor quality of x=10%, while only reaching h values around 2 kW/m^{2}K at the low mass flux of G=350 kg/m^{2}s. Using the third-degree polynomial equation relation, embedded in Figure 70, the peak

annular h value is extrapolated to reach 11.5 kW/m^{2}K in the 200-micron channel at a similar mass flux of G=1500 kg/m^{2}s and at x=14%. In a 500-micron channel, h could be expected to reach 9 kW/m^{2}K at 270 kg/m^{2}s mass flux and 14% vapor quality, according to the third-polynomial equation fit, $h = -1e7x^3 + 3e6x^3 - 161663x + 7183$.

7.4 Heat transfer characteristics with non-uniform heating

Two-phase heat transfer experiments of the 100, 200 and 500-micron channels, with HFE-7100 coolant, with non-uniform heating patterns (half die and quadrant die heating,) were performed and analyzed under fully saturated conditions. The range of mass flux considered was 350 kg/m^{2}s to 1500 kg/m^{2}s. The area average heat transfer coefficient data (using the full area of the chip) for non-uniform heating is plotted against the channel (average on the chip) heat flux and the calculated vapor quality at the channel exit as shown in Figures 72-77.

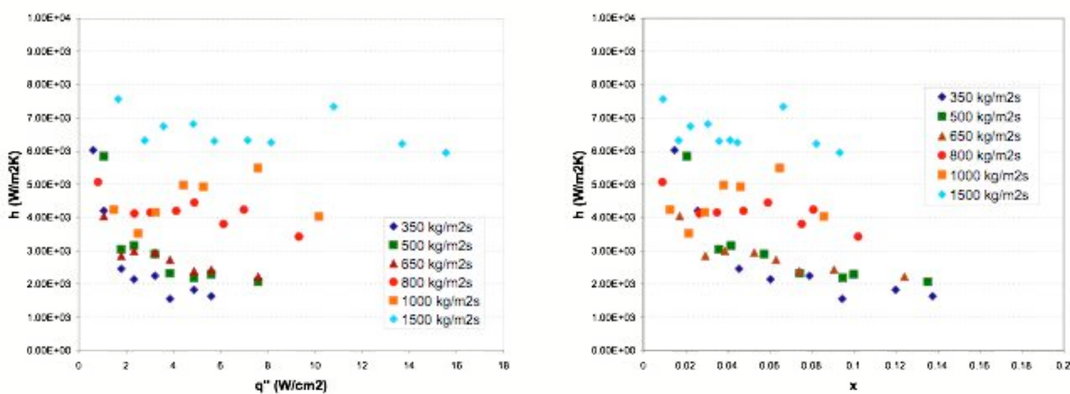

Figure 73: Two-Phase h vs. q and x for Half-Die Heating and 100-micron Channel.

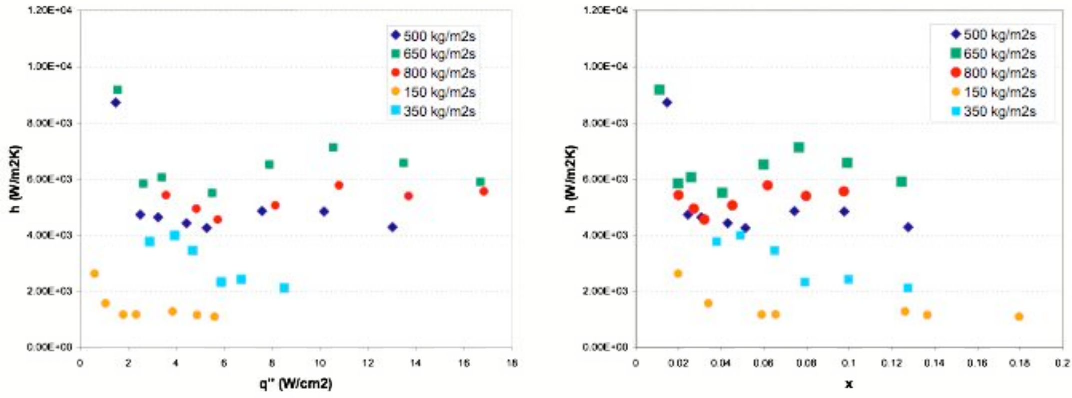

Figure 74: Two-Phase h vs. q and x for Half-Die Heating and 200-micron Channel.

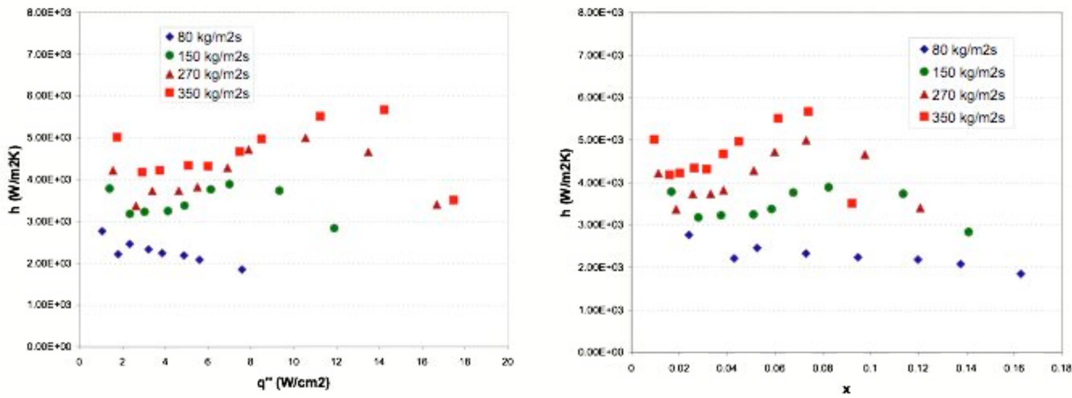

Figure 75: Two-Phase h vs. q and x for Half-Die Heating and 500-micron Channel.

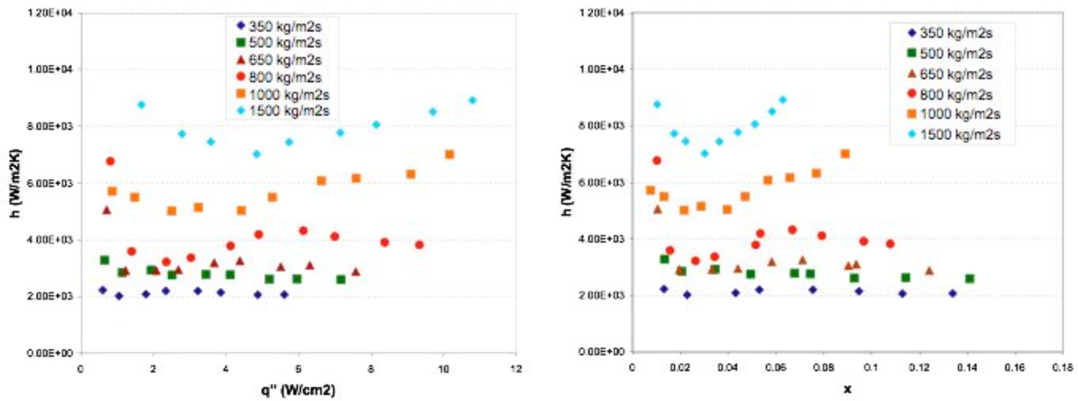

Figure 76: Two-Phase h vs. q and x for Quadrant-Die Heating and 100-micron Channel.

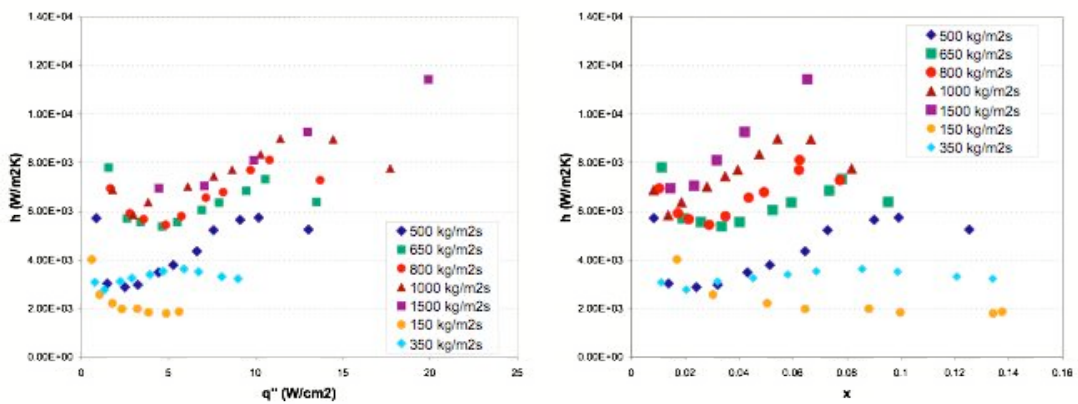

Figure 77: Two-Phase h vs. q and x for Quadrant-Die Heating and 200-micron Channel.

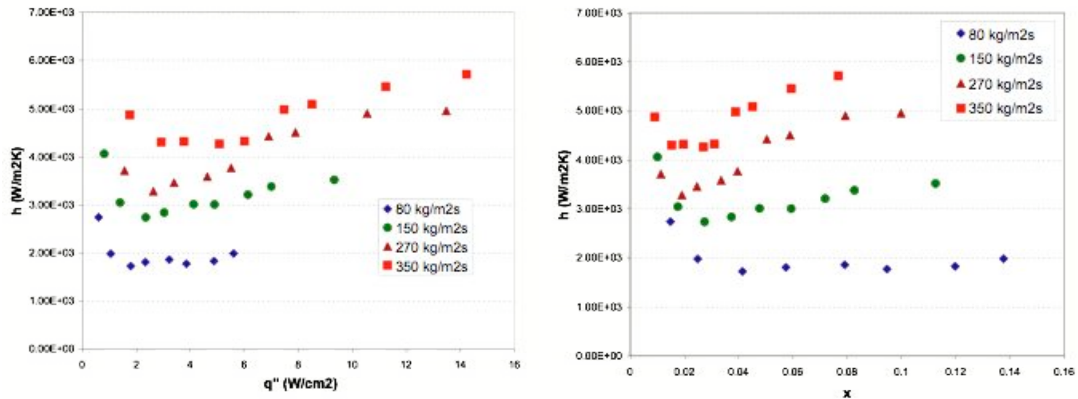

Figure 78: Two-Phase h vs. q and x for Quadrant-Die Heating and 500-micron Channel.

As with the uniform heating cases, the general trend with non-uniform heating is that the higher the mass flux (G) the higher achievable two-phase heat transfer coefficient (h) except with the 200 micron channel in which, G=650 kg/m^{2}s delivers higher h than G=800 kg/m^{2}s.

It is important to note the spatially fluctuating heat transfer coefficient behavior in the 100-micron channel with half die non-uniformity heating, at the various power levels applied as displayed in Fig. 72. This fluctuating behavior, i.e., h experiences more than two peaks, could reflect errors in the inverse determination of the heat transfer coefficients. Alternatively, these results could represent some inherent local instability in the channel, and/or wave phenomena in the two-phase flow prevailing in the channel, though – it should be noted that – no globally unstable flow conditions were encountered in these experiments. The fluctuation in h appear to be suppressed at

higher channel heights and higher mass fluxes and can be seen only at low mass flux levels with the 200 micron channel and completely vanishes with the 500-micron channel.

Similar h values can be seen with the non-uniform half die heating cases as with the uniform-heating cases. It should be noted that, with the 100-micron channel h reaches an annular flow peak of ~7.5 kW/m^2K at G=1500 kg/m^2s and vapor quality of x=7%, while h levels around 2 kW/m^2K at the low mass flux of G=350 kg/m^2s. The h value is extrapolated to increase to around 10 kW/m^2K with 200-micron channel at similar mass flux level of 1500 kg/m^2s and at around 8% vapor quality. The two-phase h, however, goes down to around 2.2 kW/m^2K at annular regime peak at G=350 kg/m^2s and at x=8%. At 500-micron channel, h would reach 6 kW/m^2K at 350 kg/m^2s mass flux and 9% vapor quality level.

Quadrant-die non-uniformity heating shows no h fluctuation observed earlier with half-die heating. Higher h levels, than those with uniform heating, are observed with 100-micron channel at the high mass flux level of 1500 kg/m^2s where the annular flow regime peak is estimated to be around 10 kW/m^2K level and at 8% quality. Similar h levels, to those with uniform heating, are observed with 200- and 500-micron channels where h can reach an h value of 13 kW/m^2K at 1500 kg/m^2s mass flux with the 200-micron channel and an extrapolated value of 20 kW/m^2K at the same mass flux with the 500-micron channel.

Chapter 8:

Heat Transfer Correlations

8.1 Introduction

Chapter 6 provided a detailed calculation procedure of the two-phase heat transfer coefficients for the various channel heights studied under the three different heating patterns considered. The heat transfer coefficients obtained for the 100-, 200- and 500-micron microgaps were compared to the predictions of the aforementioned Chen and Shah correlations detailed in Chapter 4. Statistical analysis was performed to determine the discrepancy between the values predicted by each of the correlations and the channel heat transfer data. The relative discrepancy in the prediction of heat transfer coefficients was calculated as:

$$\varepsilon_i = \frac{\left|h_{measured} - h_{correlation}\right|}{h_{measured}} \times 100 \qquad (8.1)$$

And the average relative discrepancy for a set of data was calculated as:

$$\varepsilon_{AVE} = \sum_{i=1}^{n} \frac{\varepsilon_i}{n} \qquad (8.2)$$

A total number of 459 data points (experiments) were performed on all channels (100, 200 and 500-micron) and with three different heating types, i.e., uniform, half-die and quadrant -die heating.

8.2 Dependence on Two-Phase Reynolds Number

As previously noted in Chapter 3, the dependence of the two-phase heat transfer coefficient on the two-phase Reynolds Number underpins many of the classical and commonly used two-phase heat transfer correlations. It is, therefore, of interest to examine the variation of the two-phase heat transfer coefficient as a function of the two-phase Reynolds number, defined in equation (3.16). The two-phase data of the uniformly heated 100-, 200- and 500-micron microgap channels are plotted in Fig 79. Figure 79 illustrates that the heat transfer coefficient versus two-phase Reynolds number data are widely scattered, with no clear trend but an apparent tendency for a stronger dependence at the lower Reynolds Numbers and a weaker dependence at the higher values. The best fit found for the data is a power function $h=68.3Re_{tp}^{0.68}$ with an average error of 25.3% (equal to $R^2=0.67$) and a maximum error of 106%.

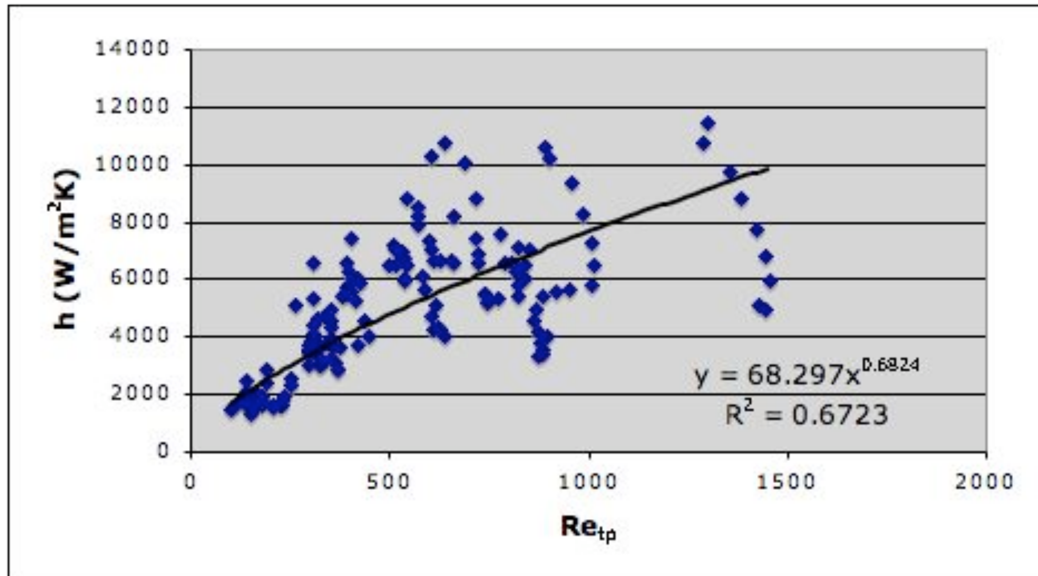

Figure 79: Two-Phase Heat Transfer Coefficient versus Re_{tp} for All Uniformly Heated Microgap Channels.

This less than satisfactory power law dependence on the two-phase Reynolds Number is thought to reflect the inherent contribution of the distinct flow regimes encountered in two-phase flow in the microgap channel. It is, thus, appropriate to look at the data sorted by the different two-phase flow regimes as a way of improving the comparison and correlation of the heat transfer coefficients. This approach is discussed in detail in the subsequent sections.

8.3 Flow regime sorting based on TD transition line

The T&D flow regime maps for uniformly heated channels, shown in Chapter 7, are used to sort the two-phase datasets into Annular and Intermittent flow regimes. Two

criteria for the transition line between Intermittent and Annular flow regimes were implemented, namely, the classical T&D angled transition line and the modified $\frac{We^{1/2}}{Bo^{1/4}} = 6.2$ based superficial gas velocity vertical line [57]. The Chen correlation was used to predict the heat transfer coefficients in the Annular flow regime while the Shah correlation was used to predict those in the Intermittent flow regime. The errors (ε_{AVE}), in percentages, associated with Chen and Shah correlations for both transition criteria, in the uniformly heated channels, are shown in Table 11.

		All Channels		100 micron		200 micron		500 micron	
		A	I	A	I	A	I	A	I
T&D	# Data Points	50	100	13	30	23	39	14	31
	error (%)	41	86	45	98	42	105	39	50
We/Bo	# Data Points	24	126	15	28	9	53	0	45
	error (%)	31	93	45	87	11	124	N/A	59

Table 11: Average error (ε_{AVE}) of Heat transfer Coefficient Predictions Sorted by Annular and Intermittent Flow Regimes per Classical T&D Line and $\frac{We^{1/2}}{Bo^{1/4}} = 6.2$ Based Line-Uniformly-Heated Channel.

As it can be seen from the data in Table 11, the Chen correlation applied to Annular flow shows better overall accuracy (41% with T&D and 31% with $\frac{We^{1/2}}{Bo^{1/4}} = 6.2$) than the Shah correlation applied to Intermittent flow (86% with T&D and 93% with $\frac{We^{1/2}}{Bo^{1/4}} = 6.2$), using both transition line criteria. Using either transition line criteria, the

Shah correlation overall is not good in prediction of data in the Intermittent flow regime. The $\frac{We^{1/2}}{Bo^{1/4}} = 6.2$ modified transition line criterion shows better accuracy than the classical T&D transition line criteria in the Annular flow and. While the $\frac{We^{1/2}}{Bo^{1/4}} = 6.2$ modified transition line shows a very good overall accuracy of 31%, its best accuracy is with the 200-micron channel in which the error is 11%.

Intermediate parameters used in the calculation of Chen heat transfer coefficients were tabulated Table 12, for the 100 micron channels with two nominal mass fluxes G=1000 kg/m^{2}s and G=1500 kg/m^{2}s. The intermediate parameters include channel hydraulic diameter D_h, heat flux q”, channel average quality x, mass flux G, Martinelli parameter X_{tt}, convective boiling enhancement factor F, two-phase Reynolds number Re_{tp} and pool boiling suppression factor S. The table also includes experimental (testing) and the Chen based heat transfer coefficient and the error (ε_i) associated with it.

D_h (mm)	q' (W/m^2)	average x	G (Kg/m^2s)	X_{tt}	F	Re_{tp}	S	h_{tp} (Chen) W/m^2K	h (test) W/m^2K	error (%)
0.0002	66262.5	0.0286345	1095.6005	3.063288	1.492045	883.9004	0.9929637	6.27E+03	6011.719	4
0.0002	75819.44	0.0323986	1107.9718	2.731477	1.572012	950.4645	0.9923446	6.83E+03	5980.5	14
0.0002	90977.78	0.0404459	1064.9642	2.220341	1.737343	1026.603	0.9916284	7.54E+03	6534.717	15
0.0002	101631.9	0.0431896	1114.1037	2.087597	1.792235	1113.362	0.9908025	8.04E+03	6710.84	20
0.0002	118436.1	0.0505479	1109.3173	1.799441	1.936407	1211.757	0.9898542	8.78E+03	6926.088	27
0.0002	130187.5	0.0567135	1086.8196	1.612895	2.0543	1269.907	0.9892883	9.25E+03	7066.873	31
0.0002	161486.1	0.071799	1064.857	1.285629	2.334119	1436.243	0.9876496	1.15E+04	6476.716	78
0.0002	35777.78	0.0112656	1503.5988	7.206691	1.089194	833.171	0.9934307	4.90E+03	5239.606	6
0.0002	48434.03	0.0152387	1504.7947	5.471285	1.187922	925.6227	0.9925764	5.72E+03	5209.672	10
0.0002	57364.58	0.0181427	1496.9856	4.663988	1.257097	985.412	0.9920169	6.18E+03	5460.376	13
0.0002	71500	0.0226133	1496.9822	3.809577	1.359716	1082.018	0.991102	7.04E+03	5483.289	28
0.0002	81416.67	0.024966	1543.968	3.477345	1.41214	1167.202	0.990285	7.64E+03	5617.517	36
0.0002	97031.25	0.0297591	1543.7144	2.955826	1.516136	1269.142	0.9892958	8.43E+03	5828.909	45
0.0002	107934	0.0330992	1543.8874	2.677643	1.586693	1338.92	0.988612	8.91E+03	6060.753	47
0.0002	125027.8	0.0395362	1497.2232	2.268206	1.718989	1425.607	0.9877553	9.48E+03	6538.388	45
0.0002	136916.7	0.0432972	1497.171	2.082718	1.794374	1498.238	0.9870318	9.90E+03	6892.935	44
0.0002	168364.6	0.0530767	1501.8317	1.717965	1.985052	1687.687	0.9851221	1.11E+04	7460.297	49

D_h (mm)	q' (W/m^2)	average x	G (Kg/m^2s)	X_{tt}	F	Re_{tp}	S	h_{tp} (Chen) W/m^2K	h (test) W/m^2K	error (%)
0.0002	66262.5	0.0286345	1095.6005	3.063288	1	536.0137	0.9960686	5.03E+03	6011.719	16
0.0002	75819.44	0.0323986	1107.9718	2.731477	1	539.9658	0.9960348	5.38E+03	5980.5	10
0.0002	90977.78	0.0404459	1064.9642	2.220341	1	514.6897	0.9962503	5.75E+03	6534.717	12
0.0002	101631.9	0.0431896	1114.1037	2.087597	1	536.899	0.996061	6.05E+03	6710.84	10
0.0002	118436.1	0.0505479	1109.3173	1.799441	1	530.4811	0.9961159	6.46E+03	6926.088	7
0.0002	130187.5	0.0567135	1086.8196	1.612895	1	516.3476	0.9962362	6.69E+03	7066.873	5
0.0002	161486.1	0.071799	1064.857	1.285629	1	497.8223	0.9963931	8.40E+03	6476.716	30
0.0002	35777.78	0.0112656	1503.5988	7.206691	1	748.7773	0.9941979	4.61E+03	5239.606	12
0.0002	48434.03	0.0152387	1504.7947	5.471285	1	746.3616	0.9942197	5.10E+03	5209.672	2
0.0002	57364.58	0.0181427	1496.9856	4.663988	1	740.2988	0.9942742	5.35E+03	5460.376	2
0.0002	71500	0.0226133	1496.9822	3.809577	1	736.9264	0.9943046	5.88E+03	5483.289	7
0.0002	81416.67	0.024966	1543.968	3.477345	1	758.2267	0.9941126	6.27E+03	5617.517	12
0.0002	97031.25	0.0297591	1543.7144	2.955826	1	754.3755	0.9941474	6.73E+03	5828.909	16
0.0002	107934	0.0330992	1543.8874	2.677643	1	751.8628	0.9941701	6.98E+03	6060.753	15
0.0002	125027.8	0.0395362	1497.2232	2.268206	1	724.2835	0.9944181	7.20E+03	6538.388	10
0.0002	136916.7	0.0432972	1497.171	2.082718	1	721.4222	0.9944437	7.38E+03	6892.935	7
0.0002	168364.6	0.0530767	1501.8317	1.717965	1	716.2705	0.9944899	8.03E+03	7460.297	8

Table 12: Parameters of Two-Phase Heat Transfer Chen Correlation on 100-micron Channel, Showing Error Reduction by Setting Convective Enhancement Term F=1.

Examining the intermediate parameters used in the calculations of Chen correlations, listed in Table 12, it is important to note that the value of the nucleate boiling suppression factor (S) across all cases studied was very close to 1 (this is actually true for the entire 459 data sets used in the study.) Also, the two-phase Reynolds number (Re_{tp}) experienced very low values across the data set (< 1700). In addition, the

average superficial gas velocity of the data points in Fig 59 is ~ 5m/s while the average superficial liquid velocity is ~ 0.5 m/s. Therefore, for the expected void fractions in the channel of more than 50%, relatively modest differences between the actual liquid and vapor velocities might be encountered for the conditions studied in the channel, suggesting that the convective enhancement in this study could be modest and that setting F equal to unity may better capture the heat transfer rate in the studied microgap channel. This was implemented and the values predicted by the Chen correlation with F=1 were shown in the same table (Table 1) above.

8.4 Pseudo flow regime sorting based on the heat transfer coefficient characteristic curve

While sorting the data based on the T&D flow regime maps, utilizing the two criteria mentioned above for transition between Intermittent and Annular flows, did not show very good overall accuracy, an attempt was made to sort the entire data based on the characteristic features of the heat transfer coefficient vs. quality curve discussed in details in Chapter 7. The sorted flow regimes, based on the characteristic h vs. x curve, will be denoted "Pseudo Intermittent" and "Pseudo Annuar".

The errors (ε_{AVE}) associated with pseudo Chen and pseudo Shah correlations were tabulated in Tables 13-18, where Tables 13-14 are for uniform heating, Tables 15-16 are for half-die non-uniform heating while Tables 17-18 are for quadrant-die non-uniform heating. As can be seen from the error tables, for each heating pattern, the error data was categorized by channel height, i.e., 100, 200 or 500 micron, and was

further sorted by the pseudo flow regime based on the characteristic h curve discussed earlier in Chapter 7, and illustrated in the example shown in Figure 80 below for the uniformly heated 100 micron channel with mass flux G=1500 kg/m^{2}s.

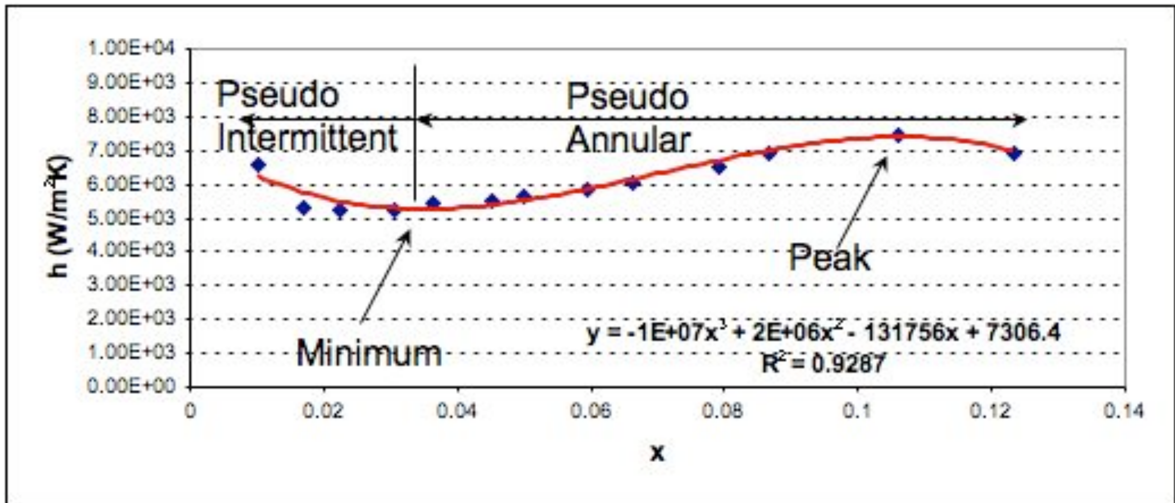

Figure 80: Characteristic Heat Transfer Coefficient Curve with Illustrated Ranges of Pseudo Annular and Pseudo Intermittent Flow Regimes, Uniformly-Heated 100-micron Channel, G =1500 kg/m^{2}s.

	# Data Points	Uniform Heating		
		Chen	Chen F=1	Shah
All	150	74	65	152
100	42	98	77	217
200	58	62	59	149
500	50	56	55	67

Table 13: Average Error (ε_{AVE}) of Heat Transfer Coefficient Predictions Using Chen and Shah Correlations for Uniformly Heated Channels.

		Uniform Heating		
		Pseudo Annular		Pseudo Intermittent
	# Data Points (A/I)	Chen	Chen F=1	Shah
All	108/42	22	19	38
100	23/19	30	9	46
200	46/12	17	20	35
500	39/11	23	23	27

Table 14: Average Error (ε_{AVE}) of Heat Transfer Coefficient Predictions Sorted by Pseudo Annular and Pseudo Intermittent Flow regimes Graphically per (h vs. x) Characteristic Curve, for Uniformly Heated Channels.

		Non-Unifrom (Half-Die) Heating		
	# Data Points	Chen	Chen F=1	Shah
All	78	95	83	162
100	23	94	73	220
200	25	123	113	171
500	30	68	66	77

Table 15: Average Error (ε_{AVE}) of Heat Transfer Coefficient Predictions Using Chen and Shah Correlations for Half-Die Heated Channels.

		Non-Unifrom (Half-Die) Heating		
		Pseudo Annular		Pseudo Intermittent
	# Data Points (A/I)	Chen	Chen F=1	Shah
All	52/26	18	16	30
100	15/8	22	14	30
200	16/9	18	17	40
500	21/9	15	18	22

Table 16: Average Error (ε_{AVE}) of Heat Transfer Coefficient Predictions Sorted by Pseudo Annular and Pseudo Intermittent Flow regimes Graphically per (h vs. x) Characteristic Curve, for Half-Die Heated Channels.

		Non-Unifrom (Quadrant-Die) Heating		
	# Data Points	Chen	Chen F=1	Shah
All	146	52	47	120
100	42	60	47	177
200	59	53	47	137
500	45	50	48	63

Table 17: Average Error (ε_{AVE}) of Heat Transfer Coefficient Predictions Using Chen and Shah Correlations for Quadrant Heated Channels.

		Non-Unifrom (Quadrant-Die) Heating		
		Pseudo Annular		Pseudo Intermittent
	# Data Points (A/I)	Chen	Chen F=1	Shah
All	109/37	32	33	32
100	31/11	21	20	35
200	44/15	25	29	34
500	34/11	50	48	27

Table 18: Average Error (ε_{AVE}) of Heat Transfer Coefficient Predictions Sorted by Pseudo Annular and Pseudo Intermittent Flow regimes Graphically per (h vs. x) Characteristic Curve, for Quadrant Heated Channels.

Looking at the uniform heating category as a reference for comparing the Chen and Shah correlations, as these correlations were established for uniform heat flux wall pipes in the first place, it is clear the Chen and Shah correlations predict well data in the pseudo Annular and pseudo Intermittent flow regimes, respectively. Chen's overall average error for predicting pseudo Annular flow regime data is 22% while that of Shah for predicting pseudo Intermittent flow regime data is 38%. Chen's best accuracy is with the 200-micron channel (17%) followed by the 500-micron channel (23%) and the 100-micron channel (30%). The accuracy of the Shah correlation prediction in the intermittent regime improves with the increase of channel height, where it is of an average error of 46% for the 100-micron channel, 35% for the 200-micron channel and 27% for the 500-micron channel.

Categorizing the data for the non-uniform heating patterns and showing the two different types of non-uniformity considered in the study, along with the sorting by the slope of the heat transfer coefficient curve, as shown in Tables 13 and 15, shows similar results to the uniform heating, relative to the accuracy of the Shah predictions. With the exception of the half-die heating pattern for which the error of the 200-micron channel (40%) is higher than that of the 100-micron channel (30%) and the 500-micron channel experiences the best accuracy with 22% average error. On the

other hand, the Chen correlations show best accuracy with half-die heating (18%) as compared to that of quadrant-die heating (32%).

The implementation of setting the Chen's convective boiling enhancement term F equal to is shown on the correlations accuracy Tables (13-18) for the entire data set. The biggest effect of setting Chen with F=1 was on the uniformly heated 100 micron channel, where the error decreases from 30% to 9%. This modification was not helpful with the higher channels heights.

Looking at the non-uniformly heated channel data in Tables 16 and 18, it can be seen that similar effect of setting F=1 can be obtained for the 100 micron channel as with the uniformly heated channel, where the error is reduced from 22% to 14% in the half-die heated channels and from 21% to 20% in the quadrant-die heated channels. For the 200- and 500-micron channels, this modification of F=1 has also a positive impact on the overall accuracy error as it dropped by a few percentage points.

8.5 Inverse calculations of spatial heat transfer coefficient

In this section, the previously validated single-phase CFD model is used to inversely determine the spatial distribution of the two-phase heat transfer coefficient. Unfortunately, today's CFD codes are incapable of directly modeling two-phase flow and it is, thus, not possible to simulate ebullient heat transfer in a microgap channel. Alternatively, it is possible to iteratively change the channel fluid properties, i.e.,

specific heat and thermal conductivity, until the model produces wall temperature distributions, which closely match the values and the pattern of the experimental results. The experimental and iteratively simulated temperature data are shown in Table 19, for the three heating patterns in a 100 micron microgap channel, with 25W heating and mass flux G=1500 Kg/m^2s. The number of trials (using Icepack CFD code [53]) needed for the iterative process was 4-5 per each case, while the final values for the adjusted fluid properties, including specific heat and thermal conductivity, were ~ 3.2 times higher than those of the single-phase (liquid-only) properties. While it was very difficult to reach a good agreement, with all the sensor temperature data, on the wall temperature distributions with the uniformly heated channel case, an attempt was made to maintain the same wall average temperature as with the experimental results (shown in Table 19.)

It is interesting to mention that a good agreement, with all the sensor temperature data, was achieved with the non-uniformly heated channels both in temperature distributions and wall average temperatures.

The conversion rate, i.e., the percentage of heat going into the channel and the spatial wall heat flux were determined from the model by solving the conductive resistance on cell-by-cell basis. Knowing the spatial wall heat flux and temperature distribution as well as the pre-assigned fluid inlet temperature (saturated temperature from the experimental cases,) the model was used to calculate and post process the wall heat transfer coefficient on cell-by-cell basis, i.e., to obtain the spatial distribution of h.

This was done by implementing Newton's second law of cooling on each cell of the wall.

This spatial wall h, q″ and temperature distribution determined by this process are illustrated in Figures 81, 82 and 83, for the three heating patterns considered, namely, uniform, half die and quadrant die heating, respectively. These cases represented the tests with total power of 25W and mass flow rate of 1.6 ml/s (equivalent to G= 1500 Kg/m^{2}s) on the 100-micron channel.

	Unifrom Heating		Half-Die Heating		Quadrant-Die Heating	
	adjusted CFD	2-phase testing	adjusted CFD	2-phase testing	adjusted CFD	2-phase testing
Sensor #						
101	84.4	88.1	97.2	96.3	72.4	72.3
102	86.2	76.4	77.1	75	104.8	101
103	84.6	87.6	76	75.3	80.5	79.4
104	86.2	89.9	97.3	97.2	75.6	75.1
105	80.6	70.1	71.5	69.6	98.7	101.4
106	78.8	84.9	70.7	69.9	74.7	75.8
107	85.9	82.1	75.6	74.4	94.2	91.7
108	81.2	83	90.8	93.1	72.9	72.5
109	79.5	86.2	88.1	93.2	69.7	70.9
Average	83	83.1	82.7	82.7	82.6	82.2
Min	78.8	70.1	70.7	69.6	69.7	70.9
Max	86.2	89.9	97.3	97.2	104.8	101.4

Table 19: Experimental (Two-Phase Test) and Iteratively Adjusted CFD Wall Temperatures for Three Heating Patterns. 100 micron Channel, 25W, G= 1500 kg/m^{2}s.

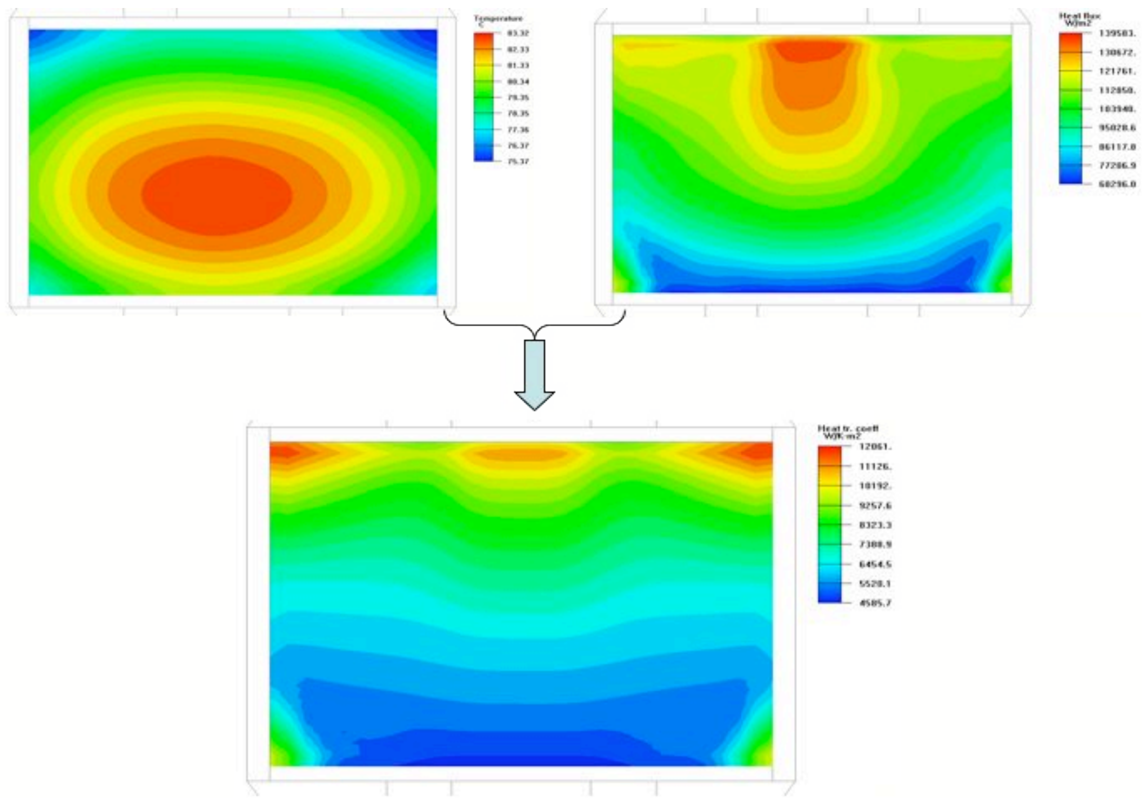

Figure 81: Inversely Calculated Spatial Heat Transfer Coefficient for 100-micron Channel and Uniform Heating. 25W, G= 1500 kg/m^{2}s.

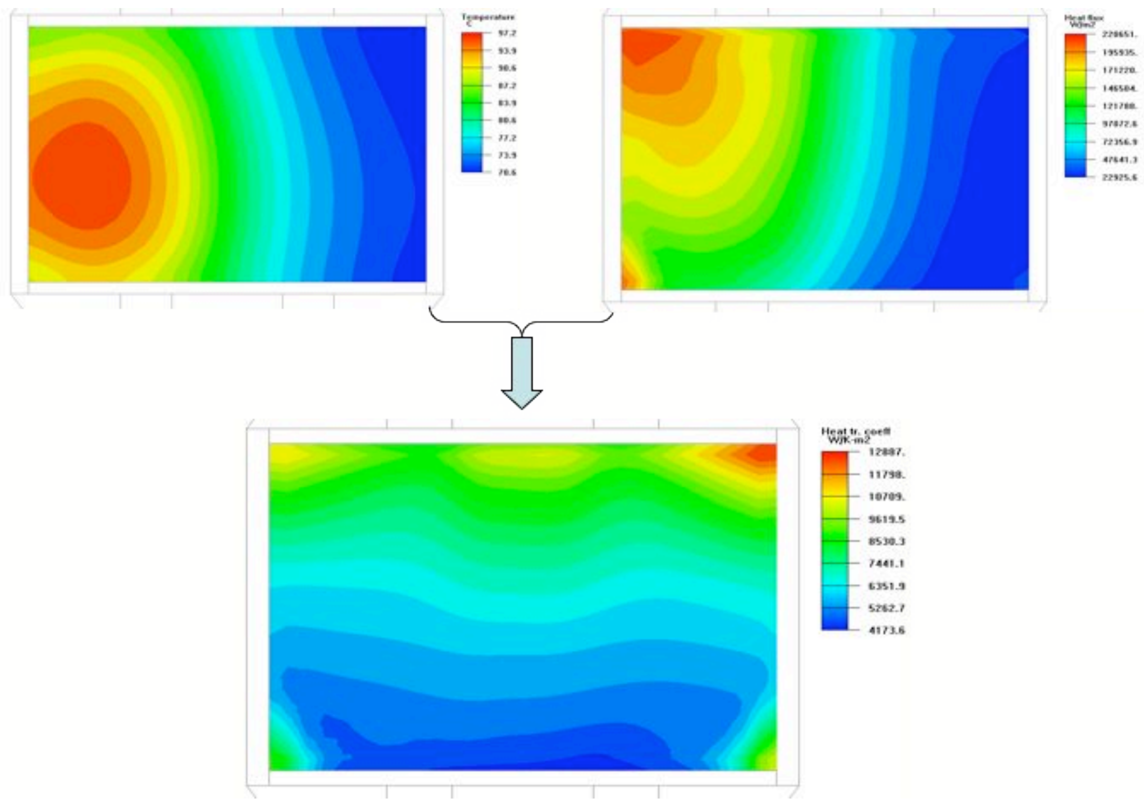

Figure 82: Inversely Calculated Spatial Heat Transfer Coefficient for 100-micron Channel and Half-Die Non-Uniform Heating. 25W, G= 1500 kg/m^{2}s.

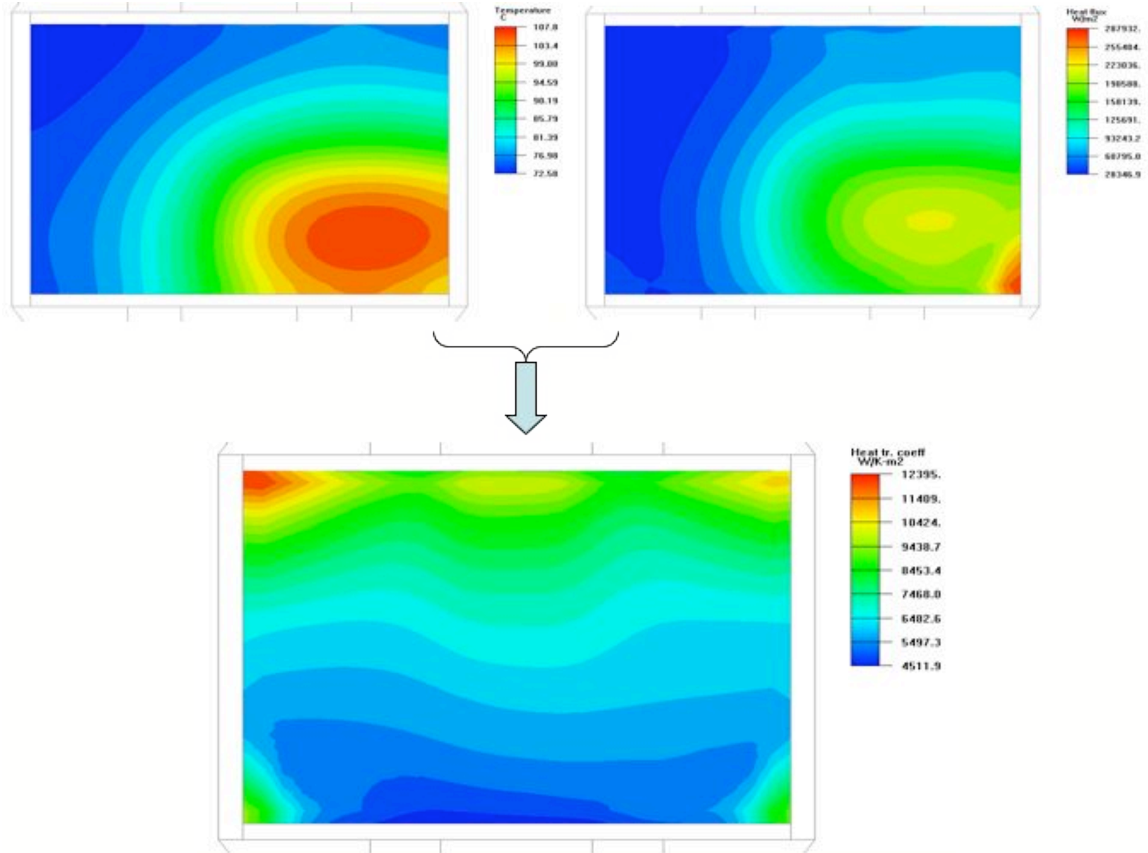

Figure 83: Inversely Calculated Spatial Heat Transfer Coefficient for 100-micron Channel and Quadrant-Die Non-Uniform Heating. 25W, G= 1500 kg/m^{2}s.

8.6 Inverse calculations of local Chen-based heat transfer coefficient

It is helpful and insightful from a research as well as a design standpoint to know how the Chen correlation would perform in predicting the local heat transfer coefficients and not only the average wall h. In this section, a numerical process is implemented to determine the efficacy of the Chen correlation in predicting the local wall h. The channel cross-section is divided into a number of small axial tubes (sub-walls) and each tube is further divided into a series of zones. It is assumed that the vapor quality

starts at zero at the beginning of all tubes (saturated conditions at channel inlet) and increases linearly across the tube length to end at the experimentally predetermined full exit quality at the channel outlet. Having determined the temperature, heat flux and average quality for each of the zones earlier from CFD, the calculation is performed to determine the Chen-based h for each of the zones.

These zonal Chen based h calculated values are compared to the zonal CFD based h. The results are illustrated in Figures 84 and 85, for both uniform heating and non-uniform heating cases. For the uniform heating case, it can be seen that the spatial Chen h does not correlate well with the spatial CFD h zonal-wise. While CFD h decreases axially along the channel axis, we see an opposite pattern, i.e., axial increase with the Chen h along the channel axis. Chen however correlates well with CFD only tube-wise if we consider h average values per each of the tubes. This is believed to be due to the characteristics of geometrical and boundary conditions (non-uniform wall heat flux) of the channel as being far from ideal channel conditions used in Chen correlations. For the non-uniform heating case, it quite clear that the spatial Chen h do not correlate with the spatial CFD h zonal-wise nor do they correlate tube-wise. This is believed to be due to the same reasons mentioned above especially the highly non-uniform wall heat flux in both axes of the wall, axially and cross-wise, respectively.
It is believed that the above technique of determination of local Chen based heat transfer coefficient, can be successful with the implementation of a robust optimization process for better correlation of local wall temperature distribution between the actual

two-phase test and the pseudo CFD model discussed in Section 8.4 above. A robust optimization algorithm can be based on locally changing the fluid properties in the pseudo CFD model in order to better correlate the local wall temperature distribution with the actual two-phase tests.

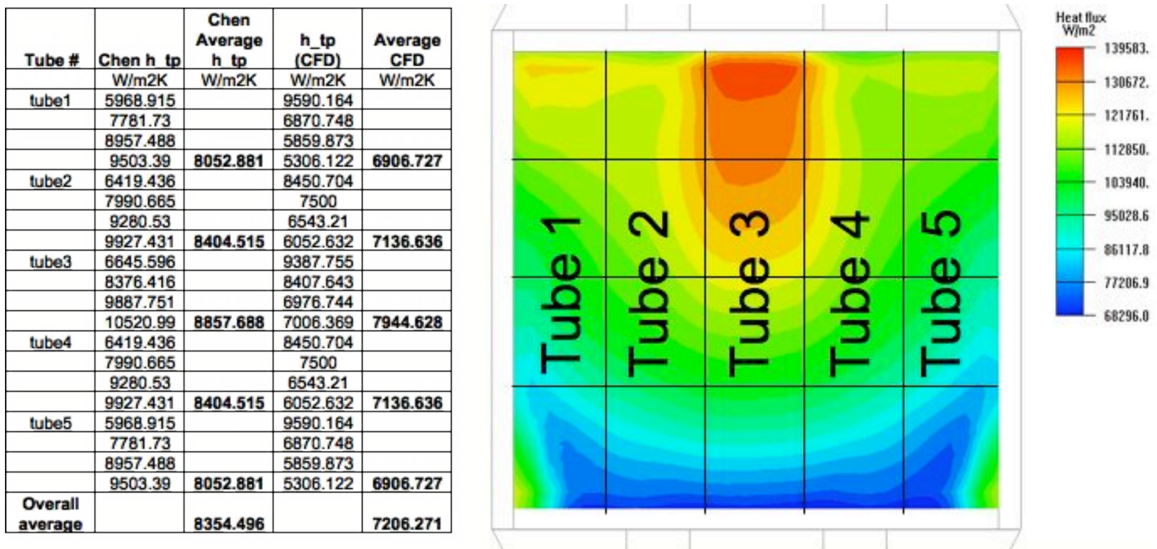

Tube #	Chen h_tp	Chen Average h_tp	h_tp (CFD)	Average CFD
	W/m2K	W/m2K	W/m2K	W/m2K
tube1	5968.915		9590.164	
	7781.73		6870.748	
	8957.488		5859.873	
	9503.39	**8052.881**	5306.122	**6906.727**
tube2	6419.436		8450.704	
	7990.665		7500	
	9280.53		6543.21	
	9927.431	**8404.515**	6052.632	**7136.636**
tube3	6645.596		9387.755	
	8376.416		8407.643	
	9887.751		6976.744	
	10520.99	**8857.688**	7006.369	**7944.628**
tube4	6419.436		8450.704	
	7990.665		7500	
	9280.53		6543.21	
	9927.431	**8404.515**	6052.632	**7136.636**
tube5	5968.915		9590.164	
	7781.73		6870.748	
	8957.488		5859.873	
	9503.39	**8052.881**	5306.122	**6906.727**
Overall average		**8354.496**		**7206.271**

Figure 84: Inversely Calculated Chen-based Spatial Heat Transfer Coefficient for 100-micron Channel and Uniform Heating. 25W, G= 1500 kg/m^{2}s.

Tube #	Chen h_tp	Chen Average h_tp	h_tp (CFD)	Average CFD
	W/m2K	W/m2K	W/m2K	W/m2K
tube1	9358.508		8750	
	11618.45		7600	
	13909.28		5263	
	14099.44	**12246.42**	6938	**7137.75**
tube2	8481.081		8809	
	10665.79		7333	
	12317.24		5500	
	12945.09	**11102.3**	5422	**6766**
tube3	6905.116		7500	
	8505.025		6941	
	9634.552		6823	
	10399.08	**8860.942**	7125	**7097.25**
tube4	4684.266		7540	
	4900.127		7258	
	5525.821		6666	
	5986.587	**5274.2**	6461	**6981.25**
tube5	4322.814		7674	
	4303.136		7333	
	4773.489		7021	
	5129.264	**4632.176**	7333	**7340.25**
Overall average		**8423.208**		**7064.5**

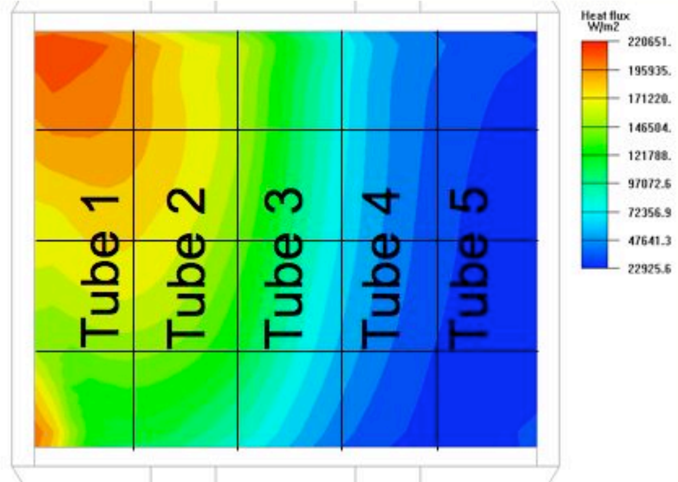

Figure 85: Inversely Calculated Chen-based Spatial Heat Transfer Coefficient for 100-micron Channel and Half-Die Non-Uniform Heating. 25W, G= 1500 kg/m^{2}s.

8.7 Prediction of wall temperature distribution and hot spots of non-uniform heating

It is of great interest for the thermal designer to resolve, even approximately, the wall temperature distribution and hot spot patterns associated with non-uniform heating or die power maps. In this section, a simple semi-numerical approach is proposed for the determination of wall temperature distribution, using correlation-derived heat transfer coefficients on the wetted surface. Given its relative accuracy in predicting the average heat transfer coefficients for the microgap channels, use can be made of the Chen correlation for this procedure. The approach involves modeling the die and the substrate in a detailed conduction model with the non-uniform heat source applied at the die junction plane and a single, average value of the flow boiling heat transfer coefficient applied to the wetted surface. In an alternative embodiment of this

approach, local values of the heat transfer coefficient could be imposed as the boundary conditions.

The approach was implemented on the 25W, 1.6 ml/s (1500 kg/m^2s) and 100-micron channel with three different heating patterns, namely, uniform, half die and quadrant die heating, respectively. Figure 86, shows the wetted wall (top die surface) temperature distribution, for each of the three cases, of the CFD inversed representing actual experiment (on the left) versus the CFD with prescribed average CFD inversed heat transfer coefficient (on the right.) It is clear that this technique predicts well the wall temperature pattern, including wall average temperature, locations of maximum temperatures and the temperature rise of the hot spots. The tabulated data of average and maximum wall temperature for these cases are listed in Table 20. The temperature differences between the two approaches are very small (1-3°C). The table shows the error associated with average wall temperatures to be 5.8%, 2.0% and 4.8% for uniform, half-die and quadrant-de heating patterns, respectively. While the error associated with maximum wall temperatures to be 5.9%, 5.4% and 2.3% for uniform, half-die and quadrant-de heating patterns, respectively.

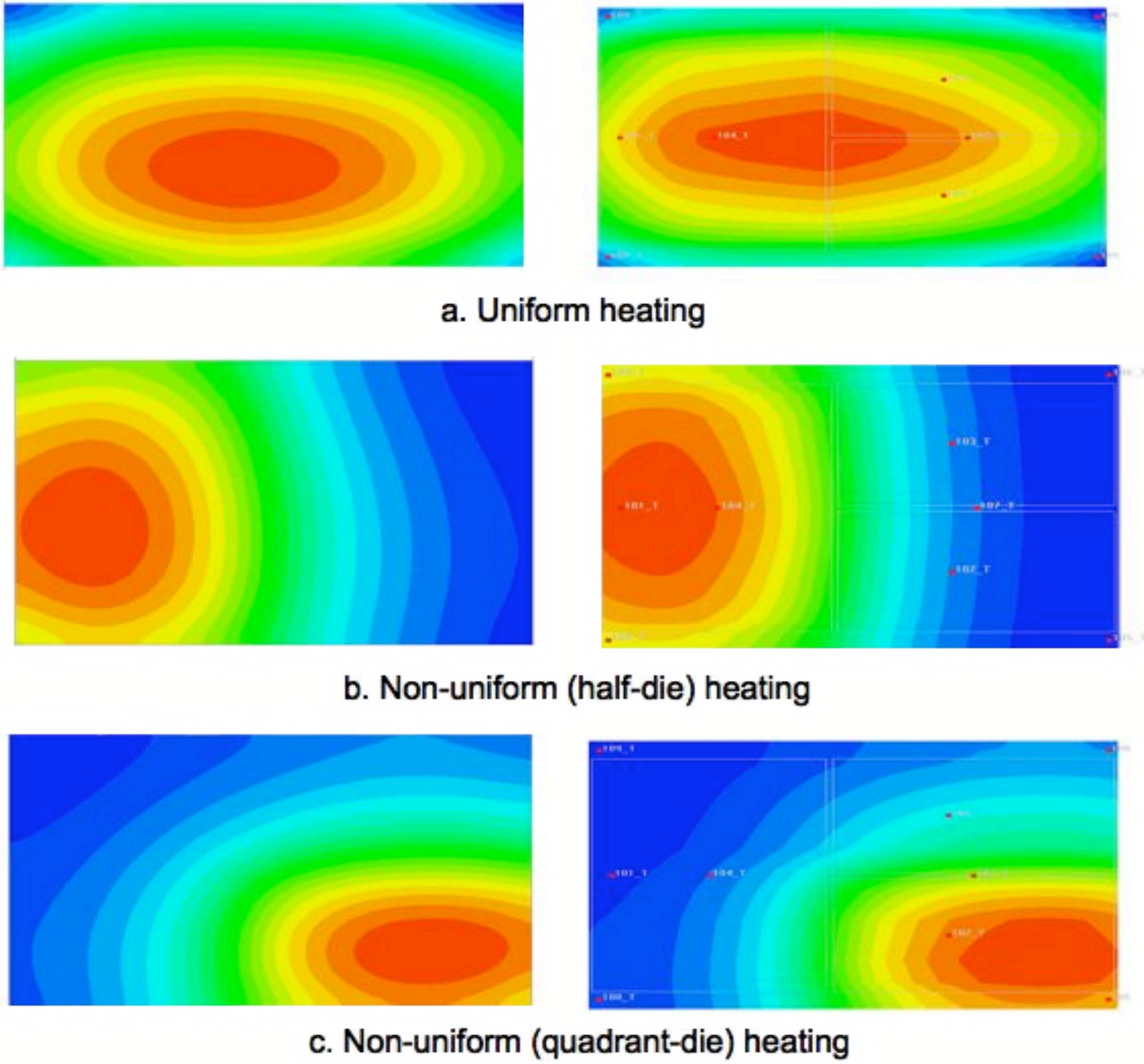

Figure 86: CFD Temperature Distribution vs. Conduction-Only Based Modeling with Wall-Prescribed Average Chen-Based h. 25W, G= 1500 kg/m^{2}s.

Heating Pattern	Uniform	Half-die	Quad-die
Average wall temperature (CFD inversed variable h)	83	82.7	82.6
Average wall temperature (fixed h)	82	82.4	82
error % (relative to Tin)	**5.8**	**2**	**4.8**
Max wall temperature (CFD inversed variable h)	86.2	97.4	104.8
Max wall temperature (fixed h)	85	99	104
error % (relative to Tin)	**5.9**	**5.4**	**2.3**
Tmax-Tave (CFD inversed variable h)	3.2	14.7	22.2
Tmax-Tave (fixed h)	3	16.6	22
error %	**6.3**	**12.9**	**0.9**

Table 20: Temperature Errors of Conduction-Only Model with Prescribed Chen-Based Average h on Wall, 100-micron Channel Flowing HFE-7100, P=25W, G= 1500 kg/m^{2}s.

8.8 Conclusions

Detailed analyses of two-phase heat transfer in non-ideal micro gap channels were performed in Chapters 7 and 8. The data show that heat transfer coefficient in such channels follows a similar M-shape characteristic curve, as a function of vapor quality, to literature data. It was quite evident that the heat transfer coefficient curve, across the various ranges of mass flux considered, can be mathematically fitted with a third-

degree polynomial that is characterized by a minimum point right after the transition from intermittent to annular flow and a maximum point (peak) at annular flow.

The general trend of heat transfer coefficient is that the higher the mass flux (G) the higher achievable two-phase heat transfer coefficient (h) with few exceptions.
Heat transfer coefficient, with the 100-micron channel h reaches an annular flow peak of ~7.8 kW/m^2K at G=1500 kg/m^2s and vapor quality of x=10%. The h value is extrapolated to increase to around 12 kW/m^2K with 200-micron channel at similar mass flux level of 1500 kg/m^2s and at around 15% vapor quality. At 500-micron channel, h could be expected to reach 9 kW/m^2K at 270 kg/m^2s mass flux and 14% vapor quality level.
The peak two-phase HFE-7100 heat transfer coefficient values were nearly 3-4 times as high as the single phase HFE-7100 values and sometimes exceed the cooling capability associated with water under forced convection.

It is important to note the fluctuating behavior, with the 100-micron channel with half die non-uniformity heating, of the heat transfer coefficient at the various power levels applied. This fluctuating behavior, i.e., h experiences more than two peaks, could reflect errors in the inverse determination of the heat transfer coefficients. Alternatively, these results could represent some inherent local instability in the channel, and/or wave phenomena in the two-phase flow prevailing in the channel, though – it should be noted that – no globally unstable flow conditions were

encountered in these experiments. The fluctuation in h appear to be suppressed at higher channel heights and higher mass fluxes and can be seen only at low mass flux levels with the 200 micron channel and completely vanishes with the 500-micron channel. Similar thermal performance levels were reported for the non-uniform heating cases as with the uniform heating ones however at slightly smaller vapor quality levels.

The Taitel-Dukler analytical flow regime map modeling suggests that majority of the present data falls within the intermittent flow regime. However, it is believed that the majority of data in this work fall into the annular flow regime. This belief is based on modifications, by researchers to the T&D flow regime map and its transition line to annular regime. The belief is also based on the very characteristic trend of heat transfer coefficient going through the annular regime in the majority of the cases considered.

While sorting the data based on the T&D flow regime maps, utilizing the original T&D criterion and the modified $\frac{We^{1/2}}{Bo^{1/4}} = 6.2$ based superficial gas velocity criterion, for transition between Intermittent and Annular flows, did not show very good overall accuracy, an attempt was made to sort the entire data graphically based on the characteristic features of the heat transfer coefficient curve. The sorted flow regimes, based on the characteristic h vs. x curve, were denoted "Pseudo Intermittent" and "Pseudo Annuar".

Heat transfer coefficients correlated well with Shah correlations in the pseudo intermittent flow regime and well with Chen correlations in the pseudo annular flow regime. Chen's overall average error for predicting the pseudo annular flow regime data is 22% while that of Shah for predicting the pseudo intermittent flow regime data is 38%. Chen's best accuracy is with the 200-micron channel (17%) followed by the 500-micron channel (23%) and the 100-micron channel (30%). The accuracy of Shah correlation prediction in the pseudo intermittent regime improves with the increase of channel height, where it is of an average error of 46% for the 100-micron channel, 35% for the 200-micron channel and 27% for the 500-micron channel.
Categorizing the data per heating patterns and showing the two different types of non-uniformity considered in the study, along with the flow regime sorting showed similar correlations with the Shah errors with the exception with the half-die heating pattern whereby the error of the 200-micron channel (40%) is higher than that of the 100-micron channel (30%) and the 500-micron channel experiences the best accuracy with 22% average error. On the other hand, Chen correlations show best accuracy with half-die heating (18%) as compared to that of quadrant-die heating (32%).

Examining the intermediate parameters used in the calculations of Chen correlations, the value of the nucleate boiling suppression factor (S) across all cases studied was very close to 1. In addition, the two-phase Reynolds number (Re_{tp}) experienced very low values across the data set (< 1700) suggesting that the convective boiling enhancement in this study could be modest and that setting F equal to unity may better

capture the heat transfer rate in the studied microgap channel. This was implemented and the biggest effect of setting Chen with F=1 was on the uniformly heated 100 micron channel, where the error decreased from 30% to 9%. This modification was not helpful with the higher channels heights.

Similar effect, by setting F=1, were obtained with the non-uniformly heated 100-micron channel as with the uniformly heated channel, where the error is reduced from 22% to 14% in the half-die heated channels and from 21% to 20% in the quadrant-die heated channels. For the 200- and 500-micron channels, this modification of F=1 had also a positive impact on the overall accuracy error as it dropped by a few percentage points.

Inverse calculations of the wall spatial heat transfer coefficient were successfully demonstrated utilizing CFD. The spatial heat transfer coefficient was correlated with their counterparts based on implementing Chen correlations. Although Chen provided accurate predictions spatially with measurements for the uniform heating cases, they however, did not correlate with the spatial measurements zonal-wise nor do they correlate tube-wise. This is believed to be due to the highly non-uniform wall heat flux in both axes of the wall, axially and cross-wise, respectively.

It is believed that the above technique of determination of local Chen based heat transfer coefficient, can be successful with the implementation of a robust optimization process for better correlation of local wall temperature distribution between the actual two-phase test and the pseudo CFD model discussed in Section 8.4 above. A robust

optimization algorithm can be based on locally changing the fluid properties in the pseudo CFD model in order to better correlate the local wall temperature distribution with the actual two-phase tests.

Finally, a semi-numerical technique was introduced for the prediction of temperature distribution and hot spots for non-uniform heating. The technique was based on solving a conduction-only model and prescribing a fixed and uniform Chen based heat transfer coefficient of the wall. The technique predicted well the wall temperature pattern including locations for maximum and minimum temperatures including locations and values of hot spots. The prediction error was largely due to the error associated with Chen correlations predicting the average wall heat transfer coefficient.

Chapter 9:

Conclusions and Future Work

9.1 Conclusions

Microgap channel coolers flowing two-phase dielectric fluid have a good potential for cooling advanced high power electronics for they provide good thermal performance and eliminate the inherited TIM thermal resistance prevailing with indirect liquid cooling techniques. They also can be considered as cost effective and reliable technique compared to expensive microchannel-based coolers. In order, however, to address the particular applications in the industry for such microgap channel coolers, a detailed study of the two-phase performance characteristics under non-ideal conditions including very short channel length, non-uniformly heated channels, conjugate heat transfer effect and packaging in a chip-scale form factor. The present work focuses on experimentally investigating and numerically modeling the two-phase as well as single-phase characteristics of microgap channels under these practical non-ideal boundary conditions for a "real world" thermal test chip.

Chapter 6 discussed in detail the various aspects of single-phase heat transfer for a chip-scale micro gap channel cooler. Single-phase heat transfer and hydraulic characterization is performed to establish the single-phase baseline performance of the microgap channel and to validate the mesh-intensive CFD numerical model developed for the test channel.

The pressure drop was found to be inversely proportional to the channel height for a fixed Re number (fixed velocity.) For HFE-7100, the pressure drop, for a fixed velocity of 6.5 m/s, increases from around 20,000 Pa for the 500-micron channel to 80,000 Pa for the 100-micron channel. The heat transfer coefficient is also inversely proportional to the channel height for a fixed Re number (fixed velocity.) The heat transfer coefficient function is pseudo linear as a function of Re number spanning the range from laminar to transitional at high flow rates (above 5 m/s.). Convective heat transfer coefficients for HFE-7100 flowing in a 100-micron microgap channel reached 9 kW/m^2K at 6.5 m/s fluid velocity.

The thermal performance for water is much better than with HFE-7100. It is around three times larger than that of HFE-7100. The heat transfer coefficient with water reaches a value of 27 kW/m^2K at 6.5 m/s velocity.

The literature correlations for pressure drop and heat transfer coefficient are well suited for ideal channels with ideal boundary conditions, i.e., channel geometries with the characteristics of uniform the flow, laminar-developing flow, uniform thermal boundary conditions (flux or temperature) and neglected conjugate heat transfer effects. The present work focused on a practical channel (non-ideal) with developing flow, non-uniform heating, non-ideal geometry, and full conjugate heat transfer effects. Although single-phase correlations captured the general dependence of the pressure drop and the heat transfer coefficient on the flow rate in this microgap channel, they have proven not to be accurate, especially at the low flow rate range. For HFE-7100

the average error of using the ideal channel pressure drop correlation is 24% and is highest at the low velocity range (0.7-1.5 m/s.) Similarly, the average heat transfer coefficient error is 7% and is highest at similar low velocity range (0.7-1.5 m/s.) Numerical modeling using computational fluid dynamics software (CFD) was extensively used in order to overcome the inappropriateness of the available correlations. A mesh intensive CFD model was developed. Despite the highly non-uniform boundary conditions imposed on the microgap channel, CFD model simulation gave excellent agreement with the experimental data (to within 5%), while the discrepancy with the predictions of the classical, "ideal" channel correlations in the literature reached 20%.

Another very important and rather critical aspect that was uncovered by the CFD mode was the spatial distribution of heat flux at the wall (die top surface) and resultant wall spatial the heat transfer coefficient. Conduction spreading of the die silicon block (800-micron thick) played an important role in changing the wall heat flux variations for all heating patterns considered (uniform and non-uniform.) It was found that silicon conduction did obscure the serpentine pattern on the wetted surface but always resulted in highly non-uniform heat flux at the wall even when the heat was applied across the entire junction plane of the chip. This provides a clear explanation for why available uniform heat flux correlations failed to predict accurately the heat transfer coefficient. Knowing the wall spatial variations of temperature and heat flux, CFD was used successfully to inversely calculate the spatial variations of wall the heat transfer

coefficient. The spatial the heat transfer coefficient was more non-uniform with non-uniform heating and was characterized by the skewed symmetry toward the higher heat flux zones of the chip compared to uniform heating**.** The flow field dominates the behavior of the heat transfer coefficient and due to conduction spreading in the chip the differences in the thermal boundary condition are minimized and have only a weak effect on the heat transfer coefficient distribution.

A detailed investigation of two-phase heat transfer in non-ideal micro gap channels, with developing flow and significant non-uniformities in heat generation, was performed in Chapters 7 and 8. Significant temperature non-uniformities were observed with non-uniform heating, where the wall temperature gradient exceeded 30°C with a heat flux gradient of 3-30 W/cm^2, for the quadrant-die heating pattern compared to a 20°C gradient and 7-14 W/cm^2 heat flux gradient for the uniform heating pattern, at 25W heat and 1500 kg/m^{2}s mass flux.

It is important to note the fluctuating behavior, with the 100-micron channel with half die non-uniformity heating, of the heat transfer coefficient at the various power levels applied. This fluctuating behavior, i.e., h experiences more than two peaks, could reflect errors in the inverse determination of the heat transfer coefficients. Alternatively, these results could represent some inherent local instability in the channel, and/or wave phenomena in the two-phase flow prevailing in the channel, though – it should be noted that – no globally unstable flow conditions were

encountered in these experiments. The fluctuation in h appear to be suppressed at higher channel heights and higher mass fluxes and can be seen only at low mass flux levels with the 200 micron channel and completely vanishes with the 500-micron channel. Similar thermal performance levels were reported for the non-uniform heating cases as with the uniform heating ones however at slightly smaller vapor quality levels.

Taitel-Dukler analytical flow regime map modeling was developed and suggested that majority of the present data falls within the intermittent flow regime. However, it is believed that the majority of data in this work fall into the annular flow regime. This belief is based on modifications, by researchers to the T&D flow regime map and its transition line to annular regime. The belief is also based on the very characteristic trend of heat transfer coefficient going through the annular regime in the majority of the cases considered.

While sorting the data based on the T&D flow regime maps, utilizing the original T&D criterion and the modified $\frac{We^{1/2}}{Bo^{1/4}} = 6.2$ based superficial gas velocity criterion, for transition between Intermittent and Annular flows, did not show very good overall accuracy, an attempt was made to sort the entire data graphically by flow regimes and type of dependence on quality (variable slope of heat transfer coefficient characteristic curve). The sorted flow regimes, based on the characteristic h vs. x curve, were denoted "Pseudo Intermittent" and "Pseudo Annular".

Heat transfer coefficients found to agree well with Shah correlations in the pseudo intermittent flow regime (38%) and well with Chen correlations in the pseudo annular flow regime (22%). Chen's best accuracy is with the 200-micron channel (17%) followed by the 500-micron channel (23%) and the 100-micron channel (30%). The accuracy of Shah correlation prediction in the pseudo intermittent regime improves with the increase of channel height, where it is of an average error of 46% for the 100-micron channel, 35% for the 200-micron channel and 27% for the 500-micron channel. Heat transfer coefficient, with the 100-micron channel was found to reach an annular flow peak of ~8 kW/m^2K at $G=1500\ kg/m^2s$ and vapor quality of x=10%. The heat transfer coefficient is extrapolated to increase to around 12 kW/m^2K with 200-micron channel at similar mass flux level of 1500 kg/m^2s and at around 15% vapor quality. At 500-micron channel, heat transfer coefficient reaches 9 kW/m^2K at 270 kg/m^2s mass flux and 14% vapor quality level.

The peak two-phase HFE-7100 heat transfer coefficient values were nearly 2.5-4 times as high as the single phase HFE-7100 values and sometimes exceed the cooling capability associated with water under forced convection.

Categorizing the data per heating patterns and showing the two different types of non-uniformity considered in the study, along with the flow regime sorting showed similar correlations with the Shah errors with the exception with the half-die heating pattern whereby the error of the 200-micron channel (40%) is higher than that of the 100-micron channel (30%) and the 500-micron channel experiences the best accuracy with

22% average error. On the other hand, Chen correlations show best accuracy with half-die heating (18%) as compared to that of quadrant-die heating (32%).

Examining the intermediate parameters used in the calculations of Chen correlations, the value of the nucleate boiling suppression factor (S) across all cases studied was very close to 1. In addition, the two-phase Reynolds number (Re_{tp}) experienced very low values across the data set (< 1700) suggesting that the convective boiling enhancement in this study could be modest and that setting F equal to unity may better capture the heat transfer rate in the studied microgap channel. This was implemented and the biggest effect of setting Chen with F=1 was on the uniformly heated 100 micron channel, where the error decreased from 30% to 9%. This modification was not helpful with the higher channels heights.
Similar effect, by setting F=1, were obtained with the non-uniformly heated 100-micron channel as with the uniformly heated channel, where the error is reduced from 22% to 14% in the half-die heated channels and from 21% to 20% in the quadrant-die heated channels. For the 200- and 500-micron channels, this modification of F=1 had also a positive impact on the overall accuracy error as it dropped by a few percentage points.

The use of inverse computation for determining two-phase heat transfer coefficients was successfully developed and demonstrated. Further efforts are needed to provide more precise local wall temperature agreement and enhance the technique accuracy. A

robust optimization algorithm can be based on locally changing the fluid properties in the pseudo CFD model in order to better correlate the local wall temperature distribution with the actual two-phase tests.

A semi-numerical first-order technique, using the Chen correlation, was found to yield acceptable prediction accuracy (17%) for the wall temperature distribution and hot spots in non-uniformly heated "real world" microgap channels cooled by two-phase flow. The technique was based on solving a conduction-only model and prescribing a fixed and uniform Chen based heat transfer coefficient of the wall. The technique predicted well the wall temperature pattern including locations for maximum and minimum temperatures including locations and values of hot spots. The prediction error was largely due to the error associated with Chen correlations predicting the average wall heat transfer coefficient.

9.2 Future work

In this dissertation a detailed modeling and characterization study of single-phase and two-phase heat transfer was conducted on a chip-scale non-uniformly heated microgap channel cooler. Thermal performance limits were established and comparisons with literature correlations of heat transfer coefficient and analysis of two-phase flow regimes were carried out. In order to complete the understanding of the thermofluid characteristics of such microgap channels, a number of future investigations are suggested as follows:

- The sorting the heat transfer coefficient data based on the T&D flow regime maps, utilizing the original T&D criterion and the modified $\frac{We^{1/2}}{Bo^{1/4}} = 6.2$ based superficial gas velocity criterion, for transition between Intermittent and Annular flows, did not show very good overall accuracy. On the other hand, the sorted flow regimes, based on the characteristic h vs. x curve, showed good accuracy using the Shah correlation in the "Pseudo Intermittent" flow regime and the Chen correlation in the "Pseudo Annular" flow regime. It is thus suggested a revisit of this subject and an extended work on possibly modifying the classical T&D transition lines for a predict better prediction of flow regimes in true microgap channels.
- The non-uniform heating and conjugate heat transfer effects are becoming critical characteristics of contemporary microprocessors and graphics chips packages. It is therefore, suggested that a future work on analyzing two-phase flow in microgap channels considers a wider range non-uniform heating patterns and different heat transfer conjugate effects.
- It is helpful and insightful from a research as well as a design standpoint to know how the Chen correlation would perform in predicting the local heat transfer coefficients and not only the average wall h. The dissertation presented a numerical process to determine the efficacy of the Chen correlation in predicting the local wall heat transfer coefficients. It is believed that this technique can be successful with the implementation of a robust optimization

process for better correlation of local wall temperature distribution between the actual two-phase test and the pseudo CFD model. A suggested future work is the investigation of a robust optimization algorithm that can be based on locally changing the fluid properties in the pseudo CFD model in order to better correlate the local wall temperature distribution with the actual two-phase tests.

- This dissertation established two-phase heat transfer performance ranges for a chip-scale microgap channel housing an actual bare die thermal test chip and flowing HFE-7100. An extension of this study, is suggested, to utilize other fluids including water/glycol mixtures and lower boiling point Novec fluids such as HFE-7000 and develop a two-phase thermal performance envelope as a function of thermo-physical properties of utilized fluids.

Bibliography

[1] Murray, C. T., International Electronics Manufacturing Initiative (iNEMI) Thermal Roadmap, MEPTEC-2005 Symposium, San Jose, 2005.

[2] Mallik, D., Thermal Issues from ITRS Perspective, MEPTEC-2006 Symposium, San Jose, 2006.

[3] Patel, C., Thermal Management from Chip Core to the Cooling Tower, MEPTEC-2005 Symposium, San Jose, 2005.

[4] Chrysler, G., Thermal management Challenges for Microprocessors, MEPTEC-2005 Symposium, San Jose, 2005.

[5] Tosaya, E., Processor Packaging thermal View, MEPTEC-2006 Symposium, San Jose, 2006.

[6] Goodson, K., Advanced Thermal Management Technologies for Electronic Systems, MEPTEC-2005 Symposium, San Jose, 2005.

[7] Howes, J., et al., Cooling of an IGBT Drive System with vaporizable Dielectric Fluid (VDF,) 24th IEEE Semi-Therm symposium, San Jose, 2008.

[8] Arik, M. and Bar-Cohen, A., "Immersion cooling for high heat flux microelectronics with dielectric liquids," 4th International symposium on advanced packaging materials, pp. 229-247, March 1998.

[9] You, S., Simon, T. and Bar Cohen, A., "A technique for enhancing boiling heat transfer with application to cooling of electronic equipment," I-THERM III, Inter society conference on thermal phenomena in electronic systems, pp. 65-73, Feb. 1992.

[10] Bergles, A. and Kim, C., “A method to reduce temperature overshoots in immersion cooling of microelectronic devices,” ITHERM-88, Inter society conference on thermal phenomena in electronic systems, pp. 100-105, May, 1988.

[11] Normington, P., Mahalingam, M., and Lee, T. Y., “Thermal Management Control Without Overshoot Using Combinations of Boiling Liquids,” IEEE Trans. Comp., Hybrids, Manufacturing Technology, vol. 15, pp. 806–814, 1992.

[12] Kraus, A., and Bar-Cohen, A., Thermal Analysis and Control of Electronic Equipment. New York: Hemisphere, 1983.

[13] Bar-Cohen, A., Arik, A., and Ohadi, M., 2006, Direct Liquid Cooling of High Flux Micro and Nano Electronic Components, Proceedings of the IEEE, Vol. 94, No.8, pp.1-22.

[14] Yokouchi, K., Kamehara, N., and Niwa, K., “Immersion cooling for high-density packaging,” IEEE transactions on components, hybrids and manufacturing, vol. CHMT-12, no. 4, pp. 643-646, December, 1987.

[15] Ciccio, J., and Thun, R., “Ultra-high density VLSI modules,” IEEE transactions on components, hybrids and manufacturing technology, vol. CHMT-1, no. 3, 1978.

[16] Lee, T. Y., Hause, V., and Mahalingam, M., “Liquid encapsulated MCM package – thermal demonstration,” IEEE Transactions on components, packaging and manufacturing technology, part A., vol. 20, no. 2, June 1997.

[17] Nelson, R., Sommerfeldt, S., and Bar-Cohen, A., “Thermal performance of an integral immersion cooled multichip module package,” in Proc. 9th IEEE SEMI-THERM Symp., 1993, pp. 8–18.

[18] Geisler, K., Straznicky, I., and Bar-Cohen, A., "Immersion cooling module for military cots applications," I-THERM V, Inter society conference on thermal phenomena in electronic systems, pp. 67-74, June 2004.

[19] Kim, D. W., Rahim, E., Bar-Cohen, A., Han, B., Thermofluid Characteristics of Two-phase Flow in Micro-Gap Channels, IEEE CPMT, pp. 979-992, 2008.

[20] Bar-Cohen, A. and Rahim, E., Modeling and Prediction of Two-Phase Microgap Channel Heat Transfer Characteristics, Heat Transfer Engineering, 2008.

[21] Thome, J., Wolverine Engineering Data Book, 2009

[22] Garimella S. V., and Singhal, V., Single-Phase Flow and Heat Transfer and pumping considerations in microchannel heat sinks, Heat Transfer Engineering, 2004

[23] Kays, W. M. and London, A. L., Compact Heat Exchangers, McGraw-Hill, New York, 1984.

[24] Shah, R. K. and London, A. L., Laminar Flow Forced Convection in Ducts, Supplement 1 to Advances in Heat Transfer, Academics, New York, 1978.

[25] Kays, W. M., and Crawford, C., "Convective Heat and Mass Transfer," McGraw-Hill, New York, 1966.

[26] Kakac, S., Shah, R., Aung, W., Handbook of Single-Phase Convective Heat Transfer, John Wiley & Sons, New York, 1978.

[27] Remley, T. J., Abdel-Khalik, S. I., Jeter, S. M., Ghiaasiaan, S. M., and Dowling, M. F., "Effect of non-uniform heat flux on wall friction and convection heat transfer coefficient in a trapezoidal channel," International journal of heat and mass Transfer, Vol. 44, Issue 13, July 2001.

[28] Mehendale, S. S., Jacobi, A. M. and Shah, R. K., Fluid Flow and Heat Transfer at Micro- and Meso-Scales with Applications to Heat Exchanger Design, Applied Mechanics Review, Vol. 53, pp. 175-193, 2000.

[29] Kandlikar, S. G. and Grande, W. J., Evolution of Microchannel Flow Passages – Thermohydraulic Performance and Fabrication Technology, Heat Transfer Engineering, Vol. 24, no. 1, pp. 3-17, 2003.

[30] Kew, P. A. and Cornwell, K., Correlations for the Prediction of Boiling Heat Transfer in Small-Diameter Channels, Applied Thermal Engineering, Vol. 17, no. 8-10, pp. 705-715, 1997.

[31] Liu, Z. and Winterton, R. H. S., A General Correlation for Saturated and Subcooled Flow Boiling in Tubes and Annuli Based on a Nucleate Boiling Equation, International Journal of Heat and Mass Transfer, Col. 34, no. 11, pp. 2759-2766, 1991.

[32] Cooper, M. G., Saturated Nucleate Pool Boiling – a Simple Correlation, Proc. of the 1st UK National Heat Transfer Conference, IChemE Symposium, Series Vol. 86 no. 2, pp. 785-793, 1984.

[33] Cooper, M. G., Flow Boiling – the Apparently Nucleate Regime, International Journal of Heat and Mass Transfer Vol. 32, no. 3, pp. 459-464, 1989.

[34] Lazarek, G. M., Black, S. H., Evaporative Heat Transfer, Pressure Drop, and Critical Heat Flux in a Small Vertical Tube with R113, International Journal of Heat and Mass Transfer, Vol. 25, no. 7, pp. 945-960, 1982.

[35] Tran, T. N., Wambsganss, M. W., and France, D. M., Boiling Heat Transfer with Three Fluids in Small Circular and Rectangular Channels, Argonne National Laboratory Dept. ANL-95-9. NTIS, Springfield, VA, 1995.

[36] Lee, H. J. and Lee, S. Y., Heat Transfer Correlation for Boiling Flows in Small Rectangular Horizontal Channels with Low Aspect Ratios, International Journal of Multiphase Flow, Vol. 27, no. 12, pp. 2043-2062, 2001.

[37] Yang, Y., Fujita, Y., Flow Boiling Heat Transfer and Flow Pattern in Rectangular Channel of Mini-gap, Second International Conference on Microchannels and Minichannels (ICMM2004-2383), New York, USA, 2004.

[38] Cortina-Diaz, M., and Schmidt, J., Flow Boiling Heat Transfer of n-Hexane and n-Octane in a Minichannel, Proc. the 13th International Heat Transfer Conference, Sydney, Australia, 2006.

[39] Madrid, F., Caney, N. and Marty, P., Flow Boiling Study in Mini-Channels," Proc. the 4th International Conference on Nanochannels, Microchannels, and Minichannels, Limerick, Ireland, Paper No. ICNMM2006-96048, 2006.

[40] Taitel, Y., and Dukler, A. E., A Model For Predicting Flow Regime Transitions in Horizontal and Near Horizontal Gas-Liquid Flow, AIChE Journal, Vol. 22, no. 1, pp. 47-55, 1976.

[41] Taitel, Y., and Dukler, A. E., Effect of Pipe Length on the Transition Boundaries for High Viscosity Liquids, International Journal of Multiphase Flow, Vol. 13, no. 4, pp 577-581, 1987.

[42] Bar-Cohen, A., Ruder, Z., and Griffith, P., Thermal and Hydrodynamic Phenomena in a Horizontal Uniformly Heated Steam Generating Pipe, Journal of Heat Transfer, Vol. 109, no. 3, pp. 739-745, 1987.

[43] Weisman, J., Duncan, D., Gibson, J., and Crawford, T., Effect of Fluid Properties and Pipe Diameter on Two-Phase Flow Pattern in Horizontal Lines, International Journal of Multiphase Flow, Vol. 5, no. 6, 437-462, 1979.

[44] Tabatabai, A., and Faghri, A., A New Two-Phase Flow Map and Transition Boundary Accounting for Surface Tension Effects in Horizontal Miniature and Micro Tubes, Journal of Heat Transfer, v 123, n 5, p 958-968, 2001.

[45] Collier, J. G., and Thome, J. R., "Convective Boiling and Condensation," Oxford Science Publications, 2001.

[46] Chen, J. C., Correlation for boiling heat transfer to saturated fluids in convective flow, Industrial and Engineering Chemistry - Process Design and Development, Vol. 5 no. 3, pp. 322-329, 1966.

[47] Kandlikar, S. G. and Balasubramanian, P., An extension of the flow boiling correlation to transition, laminar, and deep laminar flows in minichannels and microchannels, Heat Transfer Engineering, Vol. 25, no. 3, pp. 86-93, 2004.

[48] Gungor, K. E., and Winterton, R. H. S., A General Correlation for Flow Boiling in Tubes and Annuli, International Journal of Heat and Mass Transfer, Vol. 29, no. 3, pp. 351-358, 1986.

[49] Gungor, K. E., and Winterton, R.H.S., Simplified General Correlation for Saturated Flow Boiling and Comparisons of Correlations with Data, Chemical Engineering Research and Design, Vol. 65, no. 2, pp.148-156, 1987.

[50] Shah, M. M., A New Correlation for Heat Transfer During Boiling Flow Through Pipes, ASHRAE Transactions, Vol. 82, no. 2, pp. 66-86, 1976.

[51] Intel "Merom" Processor Test Vehicle, User Guide, November, 2005

[52] 3M Novec Engineering Fluid HFE-7100 for Heat Transfer, 3M, St Paul, MN, 2002.

[53] Icepak CFD Software reference Manual, Ansys, Inc., 2007.

[54] Patankar, S. V., Numerical Heat Transfer and Fluid Flow, Hemisphere, 1980.

[55] Figliola, R. and Beasley, D., Theory and Design for Mechanical Measurements, John Wiley & Sons, In., 1995.

[56] El-Genk, M. S., Combined Effects of Subcooling and Surface Orientation on Pool Boiling of HFE-7100 from a Simulated Electronic Chip. Experimental Heat Transfer, Vol. 16, Issue A, October 2003, pp. 281-301.

[57] Rahim, R., Revellin, R., Thome, J. and Bar-Cohen, A., Characterization and Prediction of Two-Phase Flow Regimes in Miniature Tubes, Submitted to IJMF, December 2009.